Measurements of the branching fraction and di-pion mass spectrum in B^0→J/ψ π^+ π^- decays

Measurements of branching fraction and di-pion mass spectrum in $B^0 \to J/\psi\ \pi^+\pi^-$ decays

Ayako Imoto

Nara Women's University

January 2007

A thesis presented to Nara Women's University
for the degree of doctor of science.

Abstract

We present a measurement of the branching fractions for neutral B meson into the final state $J/\psi\pi^+\pi^-$. The $B^0 \to J/\psi\rho^0$ is found to be the dominant component, and the additional possible contributions of $B^0 \to J/\psi f_2$ and non-resonant (nr) $B^0 \to J/\psi\pi^+\pi^-$ is also probed. The analysis is based on a data sample corresponding to 449 million $B\overline{B}$ has been collected at the $\Upsilon(4S)$ resonance by the Belle detector at the KEKB collider. Obtained branching fractions are as followings:

$$\mathcal{B}(B^0 \to J/\psi\pi^+\pi^-) = (2.2 \pm 0.3(stat.) \pm 0.2(sys.)) \times 10^{-5},$$
$$\mathcal{B}(B^0 \to J/\psi\rho^0) = (1.9 \pm 0.2(stat.) \pm 0.2(sys.)) \times 10^{-5},$$
$$\mathcal{B}(B^0 \to J/\psi f_2) < 4.9 \times 10^{-6}(@90\%\text{C.L.}),$$
$$\mathcal{B}(\text{nr}B^0 \to J/\psi\pi^+\pi^-) < 4.0 \times 10^{-6}(@90\%\text{C.L.}).$$

Contents

List of Figures

List of Tables

Chapter 1

Introduction

In the universe we are living now, only matter exists while antimatter does not remain. Since almost all the laws of nature are symmetric between matter and antimatter, solving this puzzle (matter-antimatter asymmetry) is a fundamental issue. In order to understand the matter-antimatter asymmetry, the CP violation is one of the key item to study. In the field of elementary particle physics, the Standard Model (SM) has been established during the last several decades. The SM is a re-normalizable field theory incorporating six quarks and six leptons as the basic constituent fermions, the gauge bosons mediating strong, electromagnetic and weak interactions as well as the Higgs bosons that give the masses of elementary particles.

In the SM, the CP violation as well as the flavor mixing in the quark sector is described by the Kobayashi-Maskawa (KM) theory[1]. In this theory, the quark-mixing matrix among three generation has an irreducible complex phase that gives rise to CP violation in weak interactions. In particular, the SM predicts large CP-violating asymmetries in the time-dependent rates of B^0 and $\overline{B}^0$ decays into a common CP eigenstate f_{CP}[2]. So far, the CP violation in B system has been confirmed by Belle[3] and BaBar[4] collaborations by $B^0 \to J/\psi K^0_S$ together with other $B^0 \to (c\overline{c})K^0$decays as f_{CP}. However, studies on various B decay modes play an important role in ascertaining whether or not the KM model provides a complete description of CP violation and flavor mixing in the quark sector, because various B decay final states involve different KM matrix elements and have different sensitivity to constrain the KM model as well as to probe new physics, especially concerning so-called the "penguin" that is non-leading contributions. Therefore, attempts to observe and to get comprehensive understanding of flavor non-specific neutral B meson decays are still very important.

In this thesis, the branching fraction measurement for $B^0 \to J/\psi\pi^+\pi^-$ decay is presented. In the quark level, this decay process is governed by $b \to c\overline{c}d$ transition and is a flavor-non-specific final state. It is "Cabibbo-suppressed" decay compared to the B

decays caused by $b \to c\bar{c}s$ transition, e.g. $B \to J/\psi K$ or $J/\psi K^*$ decays. Therefore, so far, other experiments have provided only limited knowledge about $B^0 \to J/\psi\pi^+\pi^-$ decay because of the limited statistics. The leading contribution, tree diagram, of this decay has same weak phase as $b \to c\bar{c}s$ decays. However, tree and penguin amplitudes all contribute to $b \to c\bar{c}d$ to the same order in the sine of the Cabibbo angle, in contrast with the $b \to c\bar{c}s$ case. Therefore, if penguin or other contributions are substantial, a precision measurement of the time-dependent CP asymmetry in $b \to c\bar{c}d$ may reveal the CP violation parameters that differ from the values for $b \to c\bar{c}s$. If it is the case, the branching fraction may also deviate from a naive expectation from already measured $B \to J/\psi K$ or $J/\psi K^*$ decays assuming simple tree-dominance with Cabibbo-suppression. In addition, by observing the di-pion invariant mass spectrum, the sources of the pion pair are resolved into the possible resonant and non-resonant contributions. The components contributing to the di-pion are also an important information to understand the strong interaction effect in the B meson decays.

In the following sections of this Chapter, the fundamental discrete transformations such as C, P and T operations and symmetries under them as well as the quark flavor mixing and the CP violation are briefly reviewed, then the relevant physics to $B^0 \to J/\psi\pi^+\pi^-$ decay is described. The experimental apparatus, the KEKB energy-asymmetric e^+e^- collider and the Belle detector are described in Chapter 2, then the event selection procedure and reconstruction are explained in Chapter 3. Measurement of the branching fraction for $B^0 \to J/\psi\pi^+\pi^-$ decay and the study on di-pion invariant mass spectrum are discussed in Chapter 4, and the work is concluded in Chapter 5.

1.1 Fundamental discrete transformations

In nature, there are three fundamental discrete transformations known as C, P and T operations. The charge conjugation operator, C changes the sign of internal charges such as electric charge, baryon number and so on. The parity operator, P produces the operation of spatial inversion of coordinates

$$(x, y, z) \implies (-x, -y, -z),$$

and T is a time reversal transformation that inverse the time coordinate. If the rule of a physics phenomena unchanged under such transformation, it is called "symmetry is conserved", while " symmetry is violated" if there is a difference in the rule between before and after a transformation. Since gravity is too small to affect elementary particle reactions, the SM is treating three interactions. Among those, strong and electromagnetic

interactions conserve each of C, P and T symmetries, while the weak interaction totally violates C and P symmetries. This weak interaction's nature results in the fact that it couples only left-handed fermions (or right-handed anti-fermions). Especially its coupling to quarks is closely related to the CP violation, therefore it is discussed more in the next section. In appendix, the complete description of C, P and T symmetries can be found.

1.2 Flavor mixing and CP violation in the quark sector

In the Standard Model, six quarks form the three doublets that are called as three quark generations:

$$\begin{pmatrix} u \\ d \end{pmatrix} \qquad \begin{pmatrix} c \\ s \end{pmatrix} \qquad \begin{pmatrix} t \\ b \end{pmatrix}$$

in terms of mass eigenstates. The flavor of quarks and leptons changes only via the charged-current weak interaction. Since the weak interaction violates the parity (P) conservation, the charged weak boson $W^{\pm}$ couples only left-handed quarks. Also, the quark weak eigenstates are different from mass eigenstates. Thus the Lagrangian of charged-current weak interaction is expressed as

$$\mathcal{L} = \frac{g}{\sqrt{2}} \left\{ (\overline{u}, \overline{c}, \overline{t})_L \gamma^\mu W_\mu^+ V_{KM} \begin{pmatrix} d \\ s \\ b \end{pmatrix}_L + (\overline{d}, \overline{s}, \overline{b})_L \gamma^\mu W_\mu^- V_{KM}^\dagger \begin{pmatrix} u \\ c \\ t \end{pmatrix}_L \right\},$$

where

$$\begin{aligned} g &: \text{coupling constant}, \\ \gamma^\mu &: \gamma \text{ matrix}, \\ W^{\pm} &: W \text{ bosons}, \\ \begin{pmatrix} d \\ s \\ b \end{pmatrix}_L \text{ or } \begin{pmatrix} u \\ c \\ t \end{pmatrix}_L &: \text{left} - \text{handed quark}, \end{aligned}$$

and V_{KM} is mixing matrix called Kobayashi-Maskawa matrix. This describes the quarks' eigenstates in the weak interaction by linear combinations of mass eigenstates.

$$V_{KM} = \begin{pmatrix} V_{ud} & V_{us} & V_{ub} \\ V_{cd} & V_{cs} & V_{cb} \\ V_{td} & V_{ts} & V_{tb} \end{pmatrix} \tag{1.1}$$

This model was proposed by M. Kobayashi and T. Maskawa in 1973[1] for explaining the CP violation in the weak interactions. This model requires the existence of at least three quark generations, i.e. six quarks, even though only three quarks had been observed, at that time. After that, c, b, and t quark were discovered in 1974, 1977 and 1995, respectively, and thus Kobayashi-Maskawa mechanism became a essential part of the Standard Model.

Since V_{KM} is unitary matrix, it satisfies:

$$V_{KM}^{\dagger} V_{KM} = \begin{pmatrix} V_{ud}^* & V_{cd}^* & V_{td}^* \\ V_{us}^* & V_{cs}^* & V_{ts}^* \\ V_{ub}^* & V_{cb}^* & V_{tb}^* \end{pmatrix} \begin{pmatrix} V_{ud} & V_{us} & V_{ub} \\ V_{cd} & V_{cs} & V_{cb} \\ V_{td} & V_{ts} & V_{tb} \end{pmatrix} = I. \tag{1.2}$$

Thus,

$$\sum_{i=u,c,t} V_{ij}^* V_{ik} \quad = \delta_{jk} \quad (j,k = d,s,b). \tag{1.3}$$

The matrix elements are parameterized by three real parameters and one complex phase. This irreducible complex phase introduces CP violation. It is convenient to write the matrix in Wolfenstein parameterization[13] which is an expansion in powers of $\lambda \equiv \sin\theta_c \simeq 0.22$, where θ_c is called Cabibbo angle.

$$V_{KM} = \begin{pmatrix} 1-\lambda^2/2 & \lambda & A\lambda^3(\rho - i\eta) \\ -\lambda & 1-\lambda^2/2 & A\lambda^2 \\ A\lambda^3(1-\rho-i\eta) & -A\lambda^2 & 1 \end{pmatrix} + \mathcal{O}(\lambda^4)$$

Among Equation 1.2, the relation involving V_{td} and V_{ub}, which is related to B meson decays, results in

$$V_{ud}V_{ub}^* + V_{cd}V_{cb}^* + V_{td}V_{tb}^* = 0.$$

Each term is expressed in Wolfenstein parametrization

$$\begin{aligned} V_{ud}V_{ub}^* &\simeq A\lambda^3(\rho + i\eta), \\ V_{cd}V_{cb}^* &\simeq -A\lambda^3, \\ V_{td}V_{tb}^* &\simeq A\lambda^3(1-\rho-i\eta). \end{aligned}$$

The three terms form a closed triangle in the complex plane, which is called "unitarity triangle", as shown in Figure 1.1. The three angle of the triangles are defined as

$$\phi_1 \equiv \arg\left(\frac{V_{cd}V_{cb}^*}{V_{td}V_{tb}^*}\right), \ \phi_2 \equiv \arg\left(\frac{V_{ud}V_{ub}^*}{V_{td}V_{tb}^*}\right), \ \phi_3 \equiv \arg\left(\frac{V_{cd}V_{cb}^*}{V_{ud}V_{ub}^*}\right).$$

Since the length of all three sides are the same order of $\mathcal{O}(\lambda^3)$, we can expect large CP violation such as $\mathcal{O}(0.1) \sim \mathcal{O}(1)$ in the B meson systems.

Summarizing the discussion in this section, the study of the B meson decays plays very important role to test the Kobayashi-Maskawa model. Next section will describe the physics related to $B^0 \to J/\psi\pi^+\pi^-$ decays.

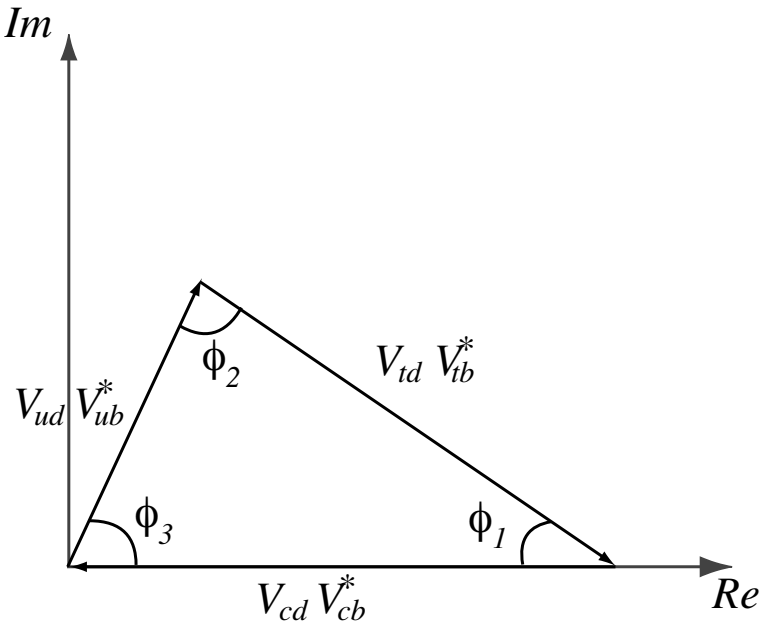

Figure 1.1: The unitarity triangle.

1.3 Physics in $B^0 \to J/\psi\pi^+\pi^-$

In $B^0 \to J/\psi\pi^+\pi^-$ decay, the ρ^0 meson is known to be a dominant source of the di-pion, so the tree and penguin diagrams for the $B^0 \to J/\psi\rho^0$ decay are shown in Figure 1.2. Here, not only ρ^0 but also other resonances can contribute if they contain the $d\overline{d}$ wave function and can decay into $\pi^+\pi^-$. The non-resonant process, the $d\overline{d}$ pair fragments hadronize into pion pair without forming any resonance as intermediate state, would contribute as well. Since both B^0 and $\overline{B}^0$ are able to cause this transition, it is a flavor non-specific neutral B meson decay.

Now, focusing on $B^0 \to J/\psi\rho^0$ decay, there are two important points. One is the fact that the tree diagram contains V_{cb} and V_{cd} which have no KM complex phase, same as the decays $B^0 \to J/\psi K^{(*)0}$ that are caused by the $b \to c\bar{c}s$ transition. Therefore the time-dependent decay rate asymmetry between B^0 and $\overline{B}^0$ is caused by the complex phase of V_{td} in $B^0 - \overline{B}^0$ mixing and the asymmetry is thought to be connected to $\sin 2\phi_1$. The other thing is this is the B decay to two vector mesons (J/ψ and ρ^0). The spins of the two vector mesons can add up to give a total spin of $0, 1$, or 2, while the B is a spin-less

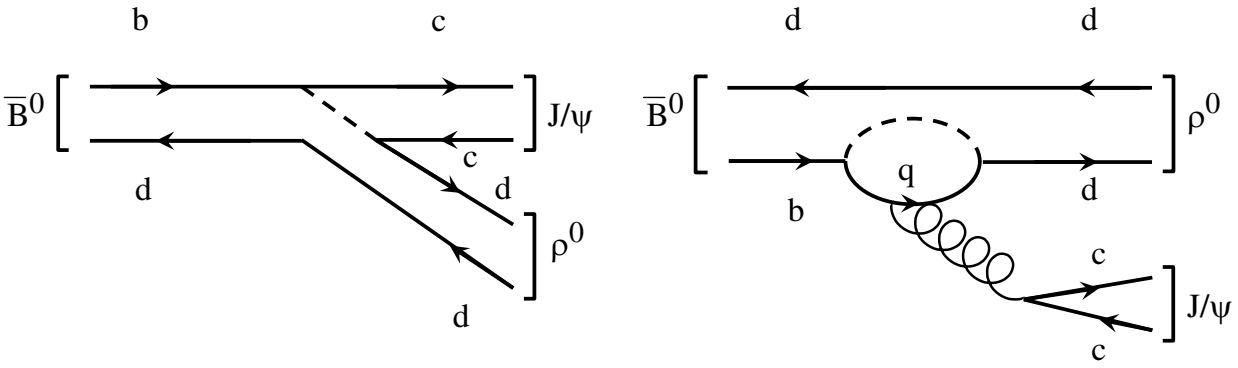

Figure 1.2: The tree and penguin Feynman diagrams for the decay $\overline{B}^0 \to J/\psi\rho^0$.

particle, therefore the final state can have an orbital angular momentum of $L = 0, 1$ or 2 between J/ψ and ρ^0, in order to conserve the total angular momentum. That means the final state is a linear combination of $L = 0, 1$ and 2 components in general. Taking account of the fact that both J/ψ and ρ^0 mesons have eigenvalues of $P = -1$ and $C = -1$, the CP eigenvalue of the final state is given by

$$CP(|J/\psi\rangle|\rho^0\rangle) = (-1)^L(|J/\psi\rangle|\rho^0\rangle). \tag{1.4}$$

Therefore this final state is not a pure CP eigenstate, but is an admixture of CP-odd and CP-even, due to the presence of the different angular momentum (L) partial waves. In spite of the dilution factor given by the amount of the $L = 0, 2$ (CP-even) and $L = 1$ (CP-odd) in the final state, this kind of decays can still be used to measure the unitarity angles, because amounts of CP-even and CP-odd partial waves can be determined by the decay products' angular distribution. The determination of the partial wave amounts is called polarization measurement. Because of the points mentioned above, if tree diagram is dominant, being same as $B^0 \to J/\psi K^{*0}(\to K^0_S\pi^0)$, we will obtain $\sin 2\phi_1$ by doing time-dependent CP violation together with polarization measurement. The detailed description of $B^0-\overline{B}^0$ mixing, mixing-induced CP violation and principle of time-dependent CP violation measurement can be found in the appendix.

However, CP violating asymmetries and polarization in $B^0 \to J/\psi\rho^0$ decay may differ from the expected ones by $B^0 \to J/\psi K^{*0}$ decay if penguin diagram or other non-standard contribution is substantial. This is because the penguin amplitude contains the V_{td} which is corresponding to an additional complex phase in the decay. In such case, branching fraction can be also affected. Because, the branching fractions can be estimated by simply scaling the measured branching fractions of the corresponding Cabibbo favored modes by assuming that the modes are dominated by the tree diagram (shown on the left of Figure 1.2), With the PDG [16] values for the branching fractions, the $B^0 \to J/\psi\rho^0$ branching

fraction is estimated as

$$Br(B^0 \to J/\psi K^{*0}) \times \left|\frac{V_{cd}}{V_{cs}}\right|^2 \times \frac{1}{2} = (3.7 \pm 0.5) \times 10^{-5}, \tag{1.5}$$

where the factor of a half comes from the coefficient of the $d\overline{d}$ content in the ρ^0 meson in $SU(3)$ flavor symmetry. The significant contribution of penguin diagram may cause the branching fraction deviating from this naive estimation.

In the experimental point of view, it is necessary to study the whole neutral B meson decay processes which result in the $J/\psi\pi^+\pi^-$ final state, because the ρ^0 meson has a large decay width. Here, a search for other resonant contributions than ρ^0 is quite interesting. For example, the f_2 meson is one of the possible candidates. Also, determination of the amount of non-resonant $B^0 \to J/\psi\pi^+\pi^-$ contribution is important to obtain the net $B^0 \to J/\psi\rho^0$ signal yield. Therefore we should attempt to resolve the entire $B^0 \to J/\psi\pi^+\pi^-$ decays into the possible resonant and non-resonant contributions. The di-pion invariant mass spectrum is the suitable observable for this purpose.

So far, CLEO[5] and BaBar[6] collaborations have been reported the branching fraction measurements of $B^0 \to J/\psi\pi^+\pi^-$ decays with their data sample corresponding to 5.1 million $B\overline{B}$ and 56 million $B\overline{B}$, respectively. In this thesis, the measurement of the branching fraction of $B^0 \to J/\psi\pi^+\pi^-$ process as well as the di-pion mass spectrum study are performed with the 449 million $B\overline{B}$ data sample which is much higher statistics data than the previous studies. It is an important step for polarization and time-dependent CP violation measurements in future.

Chapter 2

Experimental Apparatus

The Belle experiment is in operation employing the KEKB accelerator and the Belle detector at the High Energy Accelerator Research Organization (KEK), Tsukuba, Japan. The main physics goal is to test the Kobayashi-Maskawa mechanism of CP violation in B decays. The experiment has started data taking in June, 1999 and has achieved many physics results until now [23]. In this chapter, we briefly describe the KEKB e^+e^- collider and the Belle detector.

2.1 KEKB accelerator

The KEKB is an asymmetric energy e^+e^- collider with the energy of electrons and positrons are 8 GeV and 3.5 GeV, respectively. The center of mass energy is 10.58 GeV, which corresponds to the mass of the $\Upsilon(4S)$ that is the fourth resonance of b and $\overline{b}$ quarks. The $\Upsilon(4S)$ decays nearly 100% into a $B\overline{B}$ meson pair. Figure 2.1 illustrates the configuration of the KEKB. The electrons (positrons) are accelerated to their full energies by the linear accelerator (Linac) and are injected into the HER (LER) of about 3 km circumference. These rings are built side by side in a tunnel 11 m below the ground level. The KEKB has only one interaction point (IP) in the Tsukuba experimental hall, where the electron and positron beams collide at a finite angle of ± 11 mrad to avoid parasitic collisions. To measure the time-dependent CP asymmetry in B decays, KEKB is designed with the following special characteristics,

- Asymmetric energy collider
- High luminosity

In the following, we describe these items.

2.1.1 Asymmetric energy collider

KEKB consists of two storage rings for 8 GeV electron and 3.5 GeV positron. To measure CP asymmetry, we have to determine the decay time difference of B^0 and $\overline{B}^0$, Δt. However, B meson lifetime ($\sim$ 1.6 ps) is too short to determine Δt directly. If electron and positron collide with the same energy, B meson which is decayed from $\Upsilon(4S)$ is almost at rest and its flight length is only 20 μm. While, the produced B meson is boosted due to the asymmetric energy with a Lorentz factor $\beta\gamma \simeq 0.425$ and fly about 200 μm on average along the electron beam direction. Thus, Δt can be determined with enough resolution.

2.1.2 High luminosity

Luminosity $\mathcal{L}$ represents beam intensity parameter defined as $R = \mathcal{L}\sigma$, where σ and R is cross section and event rate. The branching fractions of B decays used for CP asymmetry measurements are order $10^{-4} \sim 10^{-6}$. Thus, KEKB is designed to achieve high luminosity, $10 \times 10^{33}\mathrm{cm}^{-2}\mathrm{s}^{-1}$ which corresponds to 10^8 $B\overline{B}$ pairs a year.

The $\mathcal{L}$ can be expressed as

$$\mathcal{L} = 2.2 \times 10^{34} \xi (1 + r) \left(\frac{E \cdot I}{\beta_y^*} \right)_{\pm} \tag{2.1}$$

E	:	beam energy [GeV]
I	:	circulating current [A]
ξ	:	beam-beam tune shift parameter (this parameter reflects the strength of the beam-beam collision)
r	:	aspect ratio of the beam shape (1 for a round and 0 for a flat beam)
β_y^*	:	vertical beta function at interaction point [cm]

where - and + sign represent electron and positron cases, respectively. Each ring can store at most 5000 bunches, which are clusters of a few hundred billion electrons (positrons). The main parameters of the KEKB are summarized in Table 2.1. Until July 2006, the KEKB has achieved the world record peak luminosity of $17.118 \times 10^{33}\mathrm{cm}^{-2}\mathrm{s}^{-1}$ and data recorded by the Belle detector correspond to the integrated luminosity of 710 fb^{-1}.

2.2 The Belle Detector

The Belle detector surrounds the IP to catch particles produced by the e^+e^- collisions. To measure time-dependent CP asymmetry, it is required that we fully reconstruct B meson decays efficiently, determine decay time difference and identify charged particle

Table 2.1: Main parameters of KEKB.

Ring		LER	HER	
Energy	E	3.5	8.0	GeV
Circumference	C	3016.26		m
Luminosity	$\mathcal{L}$	1×10^{34}		$\mathrm{cm}^{-2}\mathrm{s}^{-1}$
Crossing angle	θ_x	± 11		mrad
Tune shifts	ξ_x/ξ_y	0.039/0.052		
Beta function at IP	β_x^*/β_y^*	0.33/0.01		m
Beam current	I	2.6	1.1	A
Natural bunch length	σ_z	0.4		cm
Energy spread	σ_ε	7.1×10^{-4}	6.7×10^{-4}	
Bunch spacing	s_b	0.59		m
Particle/bunch	N	3.3×10^{10}	1.4×10^{10}	
Emittance	$\varepsilon_x/\varepsilon_y$	$1.8 \times 10^{-8}/3.6 \times 10^{-10}$		m
Synchrotron tune	ν_s	$0.01 \sim 0.02$		
Betatron tune	ν_x/ν_y	45.52/45.08	47.52/43.08	
Momentum compaction factor	α_p	$1 \times 10^{-4} \sim 2 \times 10^{-4}$		
Energy loss/turn	U_o	0.81†/1.5‡	3.5	MeV
RF voltage	V_c	$5 \sim 10$	$10 \sim 20$	MV
RF frequency	f_{RF}	508.887		MHz
Harmonic number	h	5120		
Longitudinal damping time	τ_ε	43†/23‡	23	ms
Total beam power	P_b	2.7†/4.5‡	4.0	MW
Radiation power	P_{SR}	2.1†/4.0‡	3.8	MW
HOM power	P_{HOM}	0.57	0.15	MW
Bending radius	ρ	16.3	104.5	m
Length of bending magnet	ℓ_B	0.915	5.86	m

†: without wigglers, ‡: with wigglers

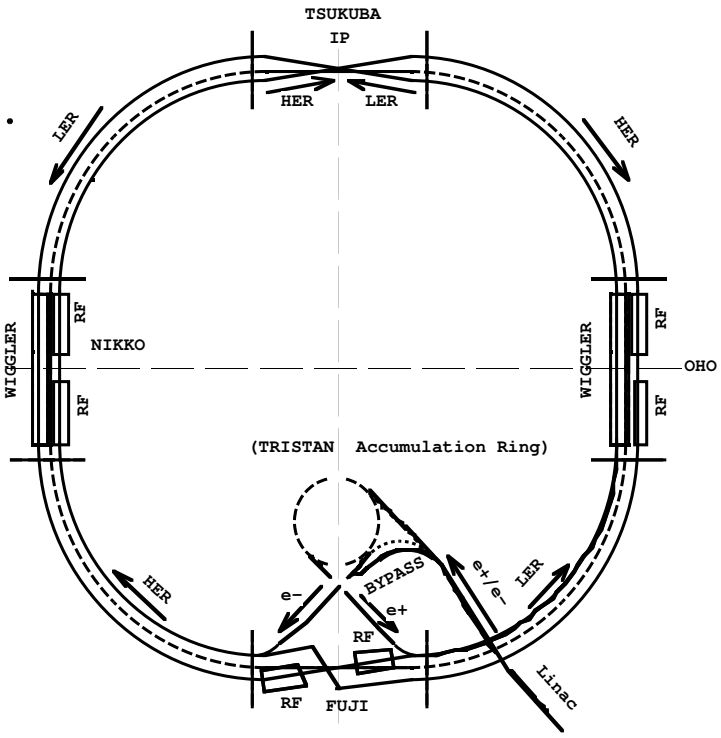

Figure 2.1: Configuration of the KEKB collider.

($e^{\pm}, \mu^{\pm}, \pi^{\pm}$ and $K^{\pm}$) for the B-flavor determination as well as the reconstruction of B decays with high purity. The Belle detector is designed to satisfy those requirements.

Figure 2.2 and 2.3 show the detector configuration. The B meson vertices are measured by the silicon vertex detector (SVD) situated just outside of a cylindrical beryllium beam pipe. Charged particle tracking is performed by the central drift chamber. Particle identification is provided by dE/dx measurements in CDC, aerogel Čherencov counter (ACC), and time-of-flight counter (TOF) placed radially outside of CDC. Electromagnetic showers, which are used to identify photons and electrons, are detected in an array of CsI(Tl) crystals (ECL) located inside the solenoid coil. The super-conducting solenoid provide a magnetic field of 1.5 T for momentum measurement of charged particles by CDC. Muons and K_L^0 mesons are identified by arrays of resistive plate counters interspersed in the iron yoke (KLM). In addition to these sub-detectors, the Belle detector has extreme forward calorimeter (EFC) to improve the experimental sensitivity to some physics processes such as $B \to \tau\nu$, as well as the luminosity measurement. The detector performance is summarized in Table 2.2.

Figure 2.4 illustrates the Belle coordinate system which is defined as:

- x: horizontal, outward to the KEKB ring,

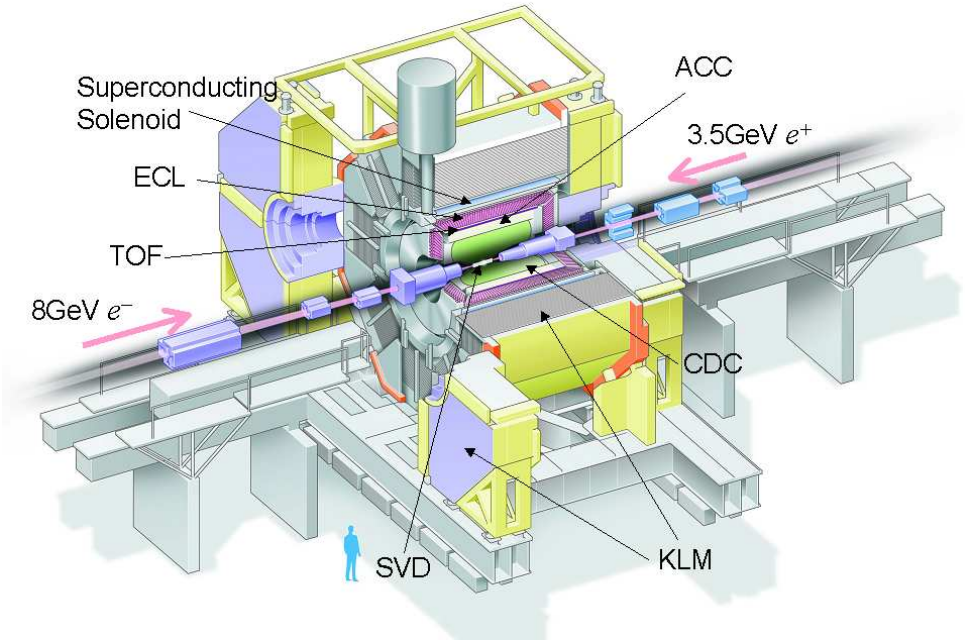

Figure 2.2: Configuration of the Belle detector system.

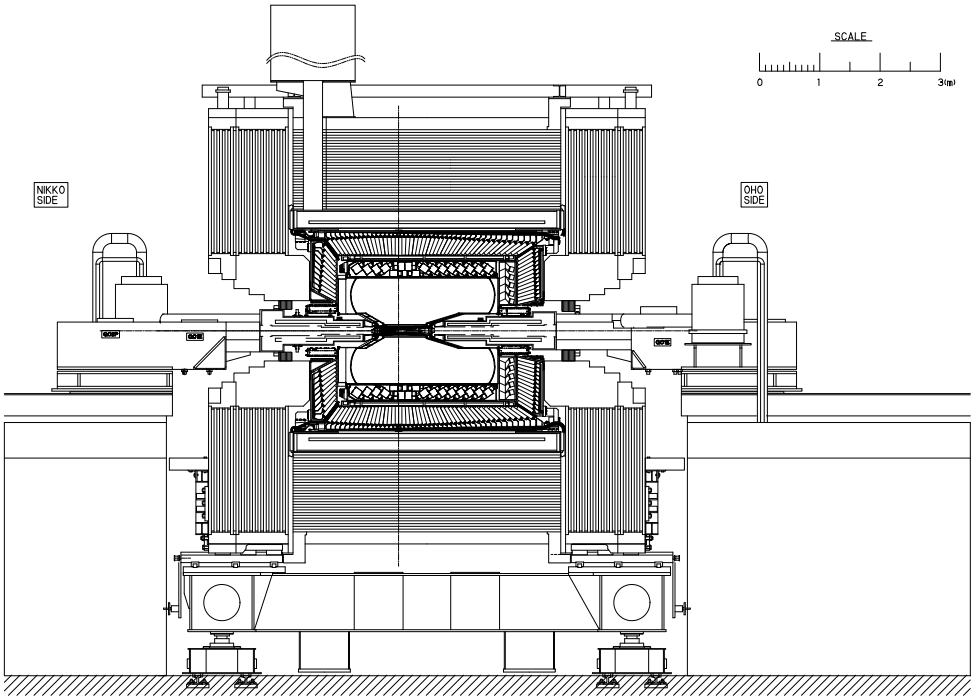

Figure 2.3: Side view of the Belle detector.

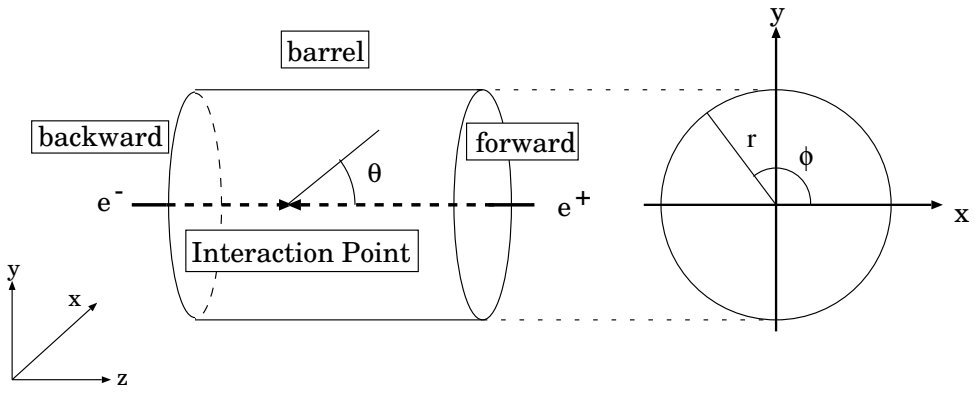

Figure 2.4: Definition of the coordinate system.

- y: vertical, upward,
- z: opposite of the positron beam direction,
- r: $\sqrt{x^2 + y^2}$,
- θ: the polar angle from z axis,
- and ϕ: the azimuth angle around z axis.

The detailed description of the Belle detector is found in the reference[25]. We give the brief description of the major detector subsystems

2.2.1 Beam Pipe

The beam pipe is designed to minimize its thickness to reduce multiple coulomb scattering which deteriorate the vertex resolution. Figure 2.5 shows the cross section of the beryllium beam pipe at the interaction region. The beam pipe which was used up to 2003 summer consists of two cylinders with different radii, the inner is 20.0 mm and the outer is 23.0 mm. Each cylinder have 0.5 mm thickness. A 2.5 mm gap between the cylinders provides a channel for cooling a beam-induced heating. Helium gas is used as a coolant in order to minimize the material in the beam pipe. Outside the outer beryllium cylinder, a 20 μm thick gold sheet is attached in order to reduce the low energy photon background from the HER. The total thickness of the beam pipe corresponds to 0.9% of a radiation length.

After 2003 summer, according to SVD upgrade, it was replaced by the one which as two cylinders with the radii of 15.0 mm and 18.0 mm. PF200 liquid is flowing in a 2.5 mm gap between two cylinders in order for cooling.

Detector	Type	Configuration	Readout	Performance
Beam pipe	Beryllium	Cylindrical, r=20 mm		He gas cooled
(∼2003)	double-wall	0.5/2.5/0.5(mm)=Be/He/Be		
Beam pipe	Beryllium	Cylindrical, r=15 mm		PF200 liquid cooled
(2003∼)	double-wall	0.5/2.5/0.5(mm)=Be/PF200/Be		
	Double	3-layers: 8/10/14 ladders	ϕ : 40.96k	$\sigma_{\Delta z}$ ∼137.9 μm
SVD1	sided	Strip pitch: 25(p)/50(n) μm	z : 40.96k	for $B^0 \to J/\psi K^0_S$
(∼2003)	Si strip			
	Double	4-layers: 6/12/18/18 ladders	ϕ : 55.296k	$\sigma_{\Delta z}$ ∼125.1 μm
SVD2	sided	Strip pitch:	z : 55.296k	for $B^0 \to J/\psi K^0_S$
(2003∼)	Si strip	75(p)/50(n) μm (layer1-3)		
		73(p)/65(n) μm (layer4)		
	Small cell	Anode: 50 layers	A: 8.4 K	$\sigma_{r\phi} = 130$ μm
CDC	drift	Cathode: 3 layers	C: 1.5 K	$\sigma_z \lesssim 200 \sim 1,400 \mu$m
	chamber	r = 8.3 - 86.3 cm		$\sigma_{p_t}/p_t = 0.3\% \sqrt{p_t^2+1}$
		-77$\leq z \leq$ 160 cm		$\sigma_{dE/dx} = 6\%$
	n : 1.01	∼12×12×12 cm^3 blocks		$N_{p.e.} \geq 6$
ACC	∼ 1.03	960 barrel		K/π separation :
	Silica	/ 228 endcap		1.2<p<3.5GeV/c
	aerogel	FM-PMT readout	1,788	
TOF	Scintillator	128 ϕ segmentation	128×2	$\sigma_t = 100$ ps
		r = 120 cm, 3 m-long		K/π separation :
TSC		64 ϕ segmentation	64	up to 1.2GeV/c
	CsI	Barrel : r = 125 - 162 cm	6,624	σ_E/E= 1.3 %/$\sqrt{E}$
ECL	(Towered-	End-cap : z =	1152 (F)	$\sigma_{pos} = 0.5$ cm/$\sqrt{E}$
	structure)	-102 cm and +196 cm	960 (B)	
Magnet	Super	inner radius = 170 cm		B = 1.5 T
	conducting			
	Resistive	14 layers	θ:16 K	$\Delta\phi$=$\Delta\theta$=30 mrad
KLM	plate	(5cm Fe+4cm gap)	ϕ:16 K	for K_L
	counters	2 RPCs in each gap		∼ 1 % hadron fake
EFC	BGO	2×1.5×12 cm^3	θ:5	σ_E/E=
			ϕ:32	$(0.3 \sim 1)\%/\sqrt{E}$

Table 2.2: Performance parameters expected (or achieved) for the Belle detector (p_t in GeV/c, E in GeV).

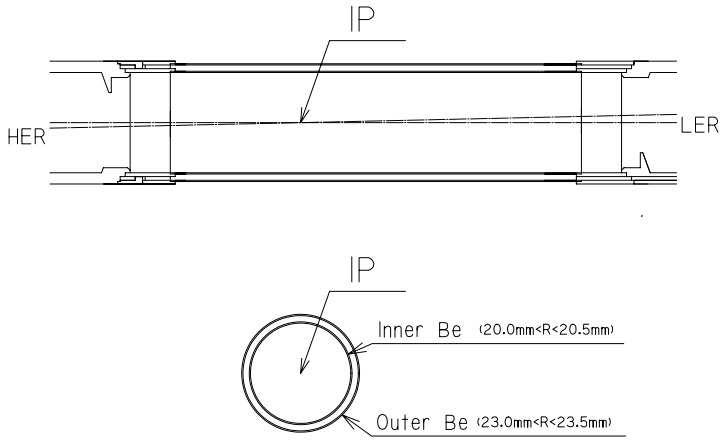

Figure 2.5: The cross section of the beryllium beam pipe at the interaction point.

2.2.2 Silicon Vertex Detector(SVD)

SVD detects the B meson vertex position which is essential for the measurement of time-dependent CP asymmetry parameters.

Figure 2.6 shows the geometrical configuration of the SVD which was used up to 2003 summer. It consists of three concentric cylindrical layers of silicon sensors and covers a polar angle $23^\circ < \theta < 139^\circ$. This corresponds to 86% of the full solid angle in the $\Upsilon(4S)$ rest frame. The radii of the three layers are 30, 45.5 and 60.5 mm. The three layers are constructed from 8, 10 and 14 ladders. Each ladder is made up of two long or short half ladders that are mechanically jointed by a support structure but electrically independent of each other. Each long half-ladder contains two double-sided silicon strip detectors (DSSDs) and a hybrid unit. Each short half-ladder contains a DSSD and a hybrid unit. The innermost layer ladder consists of two short half-ladders. The middle layer ladder consists of a short and a long half-ladder. The outermost layer ladder consists of two long half-ladders.

We use S6936 DSSDs fabricated by Hamamatsu Photonics, which were originally developed for the DELPHI[26]. The size of DSSD is 57.5×33.5 mm^2 with thickness of 300 μm. The schematic view of DSSD is shown in Figure 2.7. One side (n-side) of DSSD has n^+ strips oriented perpendicular to the beam direction to measure the z coordinate. The other side (p-side) with longitudinal p^+ strips allows the ϕ coordinate measurement. The n^+-strips are interleaved by p^+ implants, which are called p stops, to separate the consecutive strips electrically. The bias voltage of 75V is supplied to the

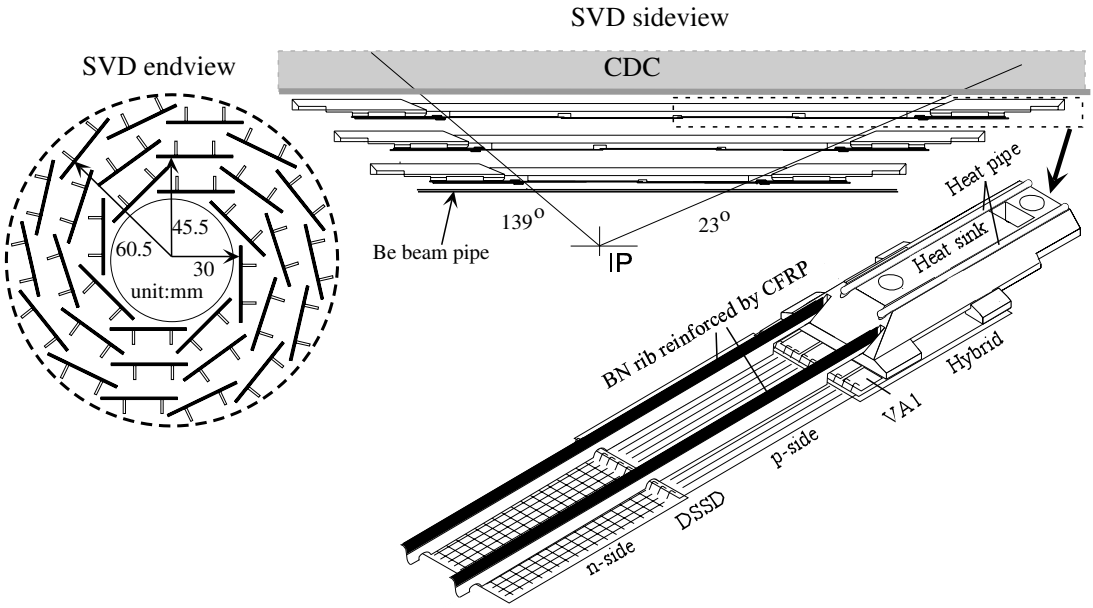

Figure 2.6: Detector configuration of SVD.

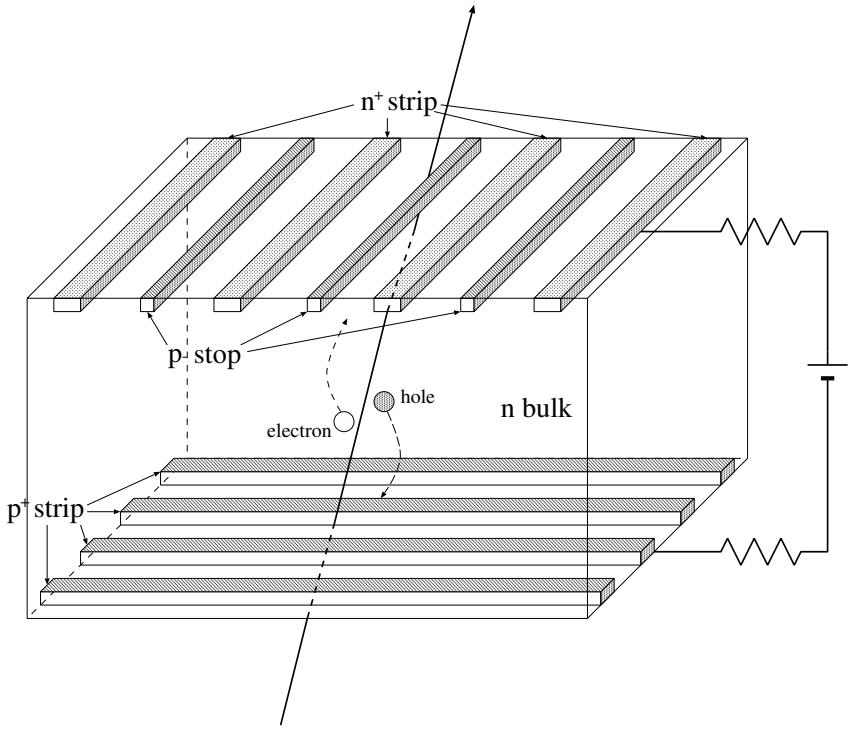

Figure 2.7: Schematic drawing of the DSSD.

n-side, while p-side is grounded. A charged particle passing through the depletion region of the n bulk silicon generates pairs of electron and hole. The electrons and holes drift to each strip and make two dimensional hit signals. The strip pitch is 25 μm for p-side and 42 μm for n-side. On the n-side, adjacent strips are read out by a single channel. This gives an effective strip pitch of 84 μm. On the p-side, every other strip is connected to a readout channel. Charge collected by the floating strips in between is read from adjacent strips by means of capacitive charge division. The signal of DSSDs are read out by VA1 chips[27] [28]. The VA1 chip is a 128 channel CMOS integrated circuit fabricated in the Austrian Micro Systems (AMS). Five VA1 chips are on both side of each hybrid unit. A total number of readout channels is 81,920.

The performance of SVD is parameterized by the SVD-CDC track matching efficiency and the impact parameter resolution of tracks with associated SVD hits. The SVD-CDC track matching efficiency is defined as the probability that a CDC track within the SVD acceptance has associated SVD hits in at least two layers, and in at least one layer with both the r-ϕ and r-z information. Figure 2.8 shows the SVD-CDC track matching efficiency for hadronic events as a function of time. The average matching efficiency is better than 98.7%, although we observe slight degradation after one year operation as a result of the gain loss of VA1 from radiation damage[29]. The momentum and angular dependence of the impact parameter resolution are shown in Figure 2.9. They are well represented by the following formula: $\sigma_{xy} = 19 \oplus 50/(p\beta \sin^{3/2}\theta)$ μm and $\sigma_z = 36 \oplus 42/(p\beta \sin^{5/2}\theta)$ μm, where "$\oplus$" indicates a quadratic sum.

In summer 2003, a new vertex detector, SVD2, was successfully installed. SVD2 has four detector layers, comprising 6, 12, 18, 18 ladders in the first, second, third layer, respectively. Detector acceptance is also improved to have larger coverage, $17° < 150°$, which is the same as CDC. The first layer is even closer to the interaction region than for the previous SVD (SVD1). The beam pipe is replaced by a new and smaller (1.5 cm in radius) one as describe in the previous subsection.. Two kinds of DSSDs are installed; 34.9×76.4 mm^2 DSSDs are used for the fourth layer, and 28.4×79.6 mm^2 DSSDs are used four other three layers. For the inner three layers, the z-strip pitch is 75μm and the ϕ-strip pitch is 50 μm. For the fourth layer, the z-strip (ϕ-strip) pitch is 73 (65) μm. Four VA1TA chips are installed on each hybrid. Each VA1TA chip consists of 128 channels and amplifies the signals from 128 strips. These VA1TA chips can be read in parallel, and the readout deadtime is reduced. They also have higher radiation tolerance than the VA1 chips. The sideview of SVD2 system is illustrated in Figure 2.10, while a typical hadronic event recorded by SVD2 is shown in Figure 2.11.

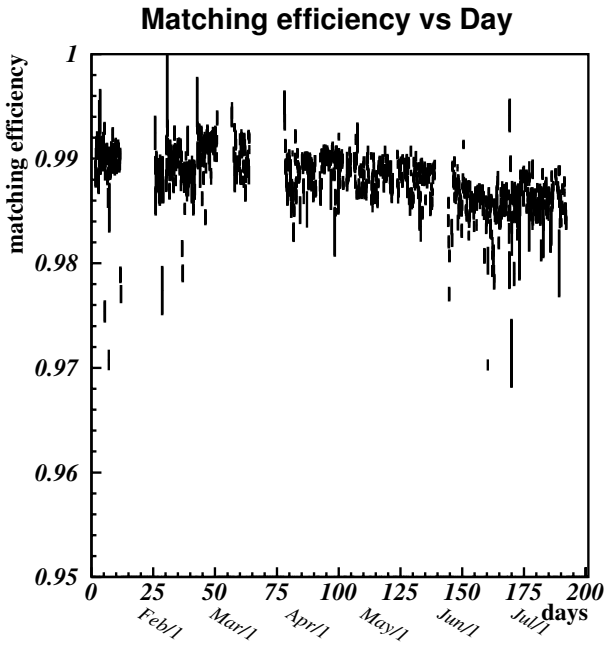

Figure 2.8: SVD-CDC track matching efficiency as a function of the date of data taking.

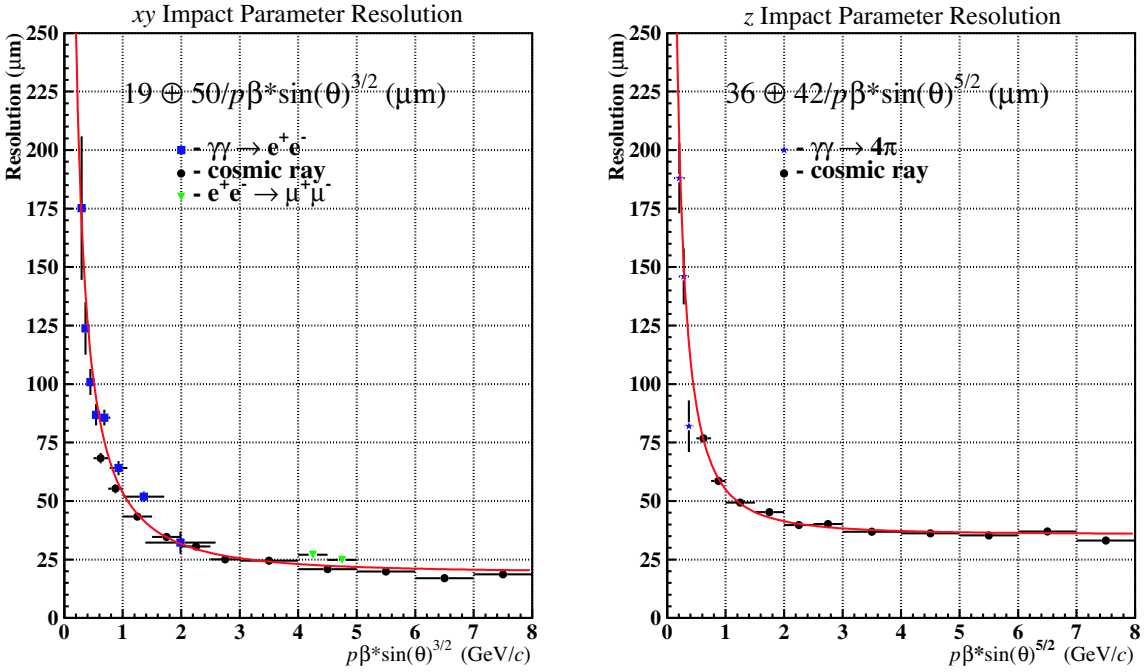

Figure 2.9: Impact parameter resolution of charged tracks with associated SVD hits.

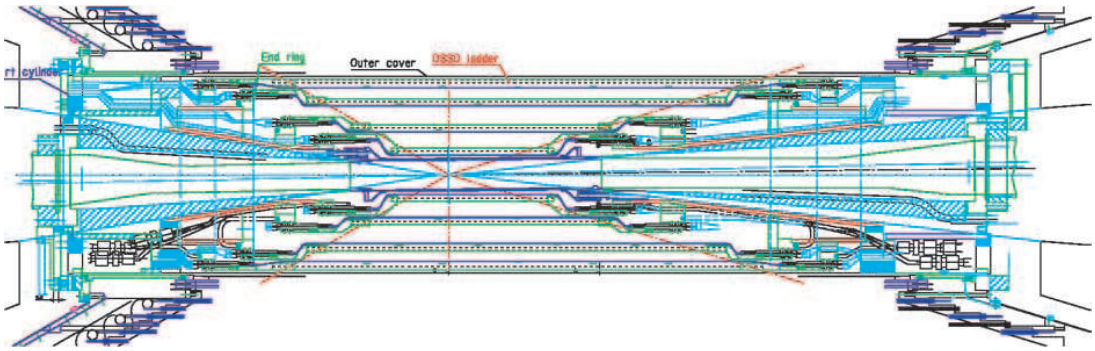

Figure 2.10: An illustration of the second version of silicon vertex detector, SVD2

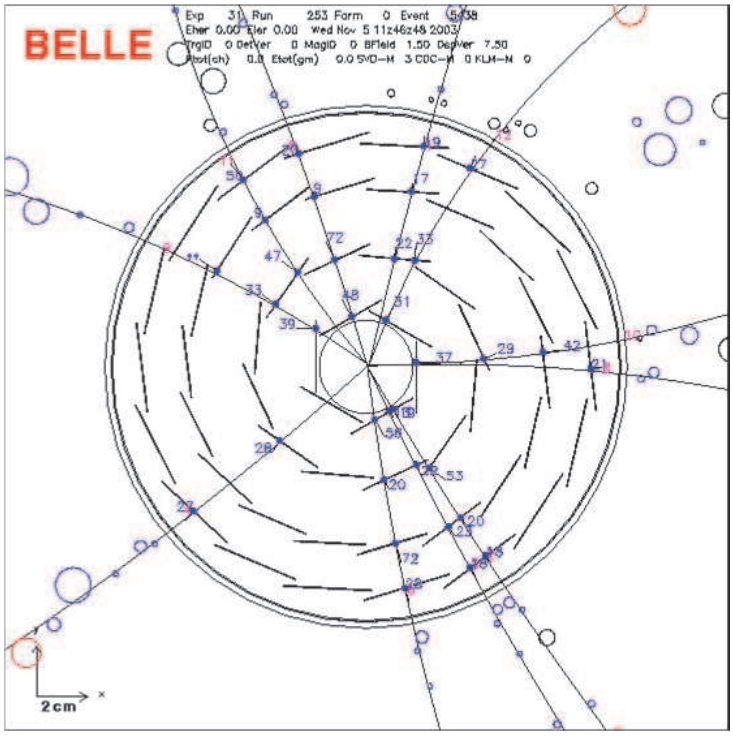

Figure 2.11: An typical hadronic event recorded by SVD2. Four DSSD detector layers can be clearly seen. The dots denote the SVD2 hits associated with reconstructed charged tracks. The open circle represents the CDC hits.

2.2.3 Central Drift Chamber(CDC)

The main role of Central Drift Chamber(CDC) is detection of charged particle tracks and reconstruction of their momenta from their curvature in the magnetic field of 1.5 T provided by the superconducting solenoid. CDC also provides particle identification information in the form of dE/dx measurements for charged particles.

The structure of CDC is shown in Figure 2.12. The length is 2,400 mm, and the inner and outer radii are 83 and 874 mm, respectively. The polar angle coverage is $17° \leq \theta \leq 150°$. CDC is a small cell drift chamber containing a total of 50 anode sense wire layers (32 axial wire layers and 18 stereo wire layers) and 3 cathode strip layers. The axial wires are configured to be parallel to z axis, while the stereo wires are slanted by approximately ± 50 mrad. The three dimensional information is provided by this wire configuration. Eight field wires surround a sense wire to provide drift electric field, and the field wires and a sense wire form a drift cell. The cell structure is shown in Figure 2.13. CDC has 8,400 drift cells. A mixture of helium (50%) and ethane (50%) gas is filled in the chamber with atmospheric pressure. A charged particle passing through CDC ionizes the gas. The electrons, liberated from the ionized gas, drift to a sense wire with a specific drift velocity and cause charge avalanches, then the measured signal height and the drift time provides information of the energy deposit and the distance from the sense wire. In the innermost radii, the three cathode strip layers are installed to provide the z position measurements of tracks for the trigger system. The number of readout channel is 8,400 for anode sense wires and 1,792 for cathode strips.

Figure 2.14 shows the transverse momentum (p_t) resolution as a function of p_t. The p_t resolution is $(0.20 p_t \oplus 0.29)\%$, where p_t is in unit of GeV/c. Figure 2.15 shows a scatter plot of measured dE/dx and particle momentum. Populations of pions, kaons, protons and electrons are clearly seen. Figure 2.16 shows the distribution of dE/dx for minimum ionizing particles measured with pions from K^0_S decays. The dE/dx resolution is measured to be 7.8%

2.2.4 Aerogel Čherenkov Counter(ACC)

The aerogel Čherenkov counter (ACC) provides separation between $K^\pm$ and $\pi^\pm$ with momentum ranged from 1.2 GeV/c to 3.5 GeV/c.

ACC detects if the particle emits Čherenkov light or not and distinguishes particle species. A charged particle passing through a matter emit Čherenkov light if its velocity is larger than the light velocity in the matter. The condition to emit Čhrenkov light is

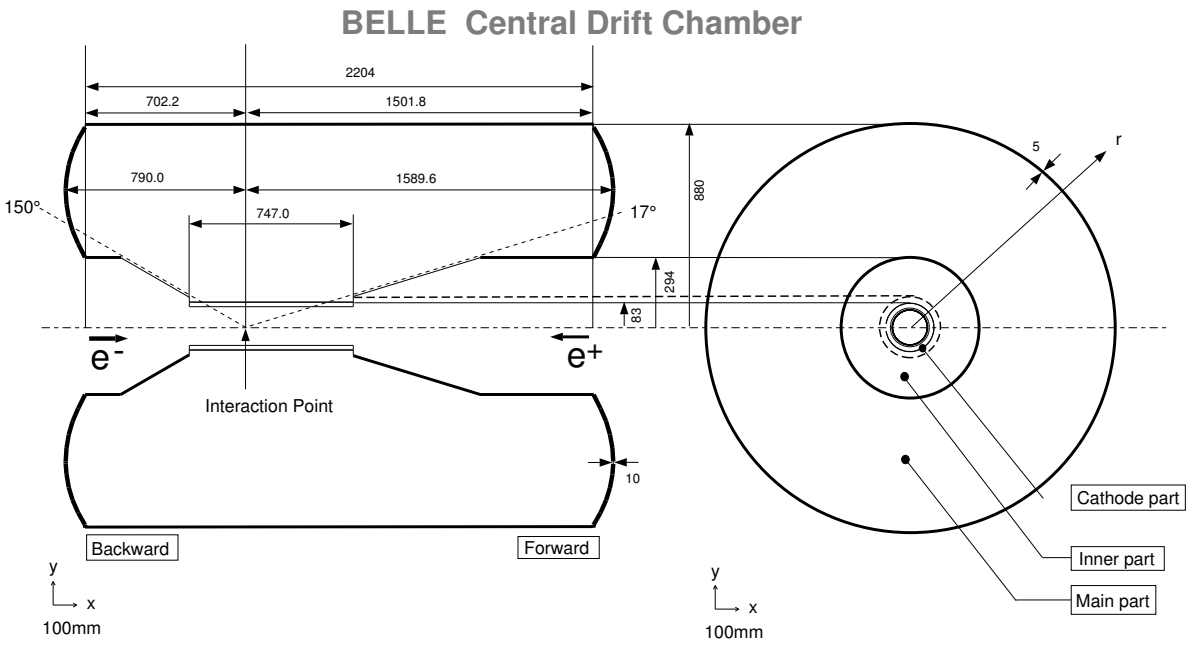

Figure 2.12: Overview of the CDC structure. The lengths in the figure are in units of mm.

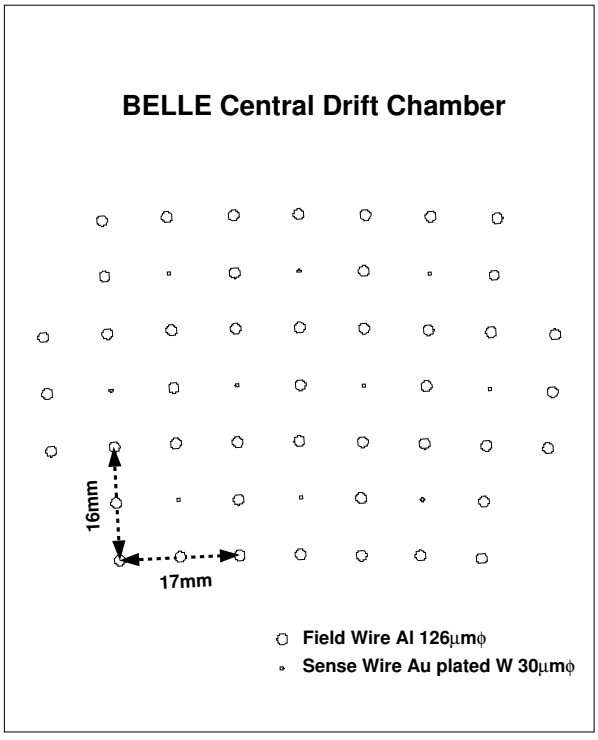

Figure 2.13: Cell structure of CDC.

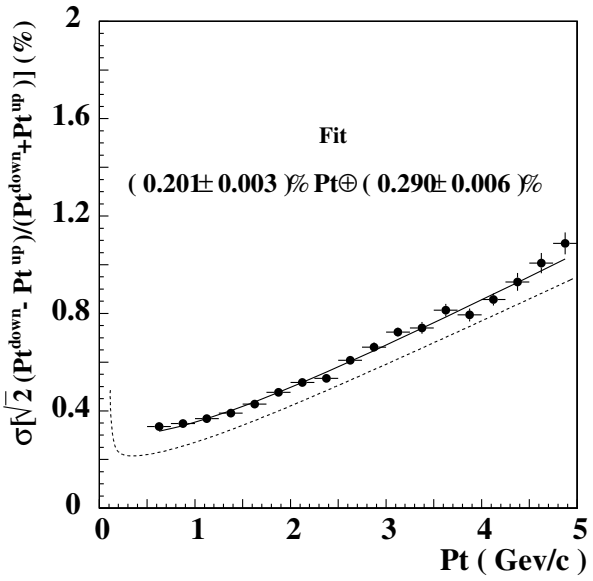

Figure 2.14: The p_t resolution is a function of p_t itself. The solid curve shows the fitted result ($0.201\% p_t \oplus 0.290\%/\beta$) and the dotted curve shows the ideal expectation for $\beta = 1$ particles.

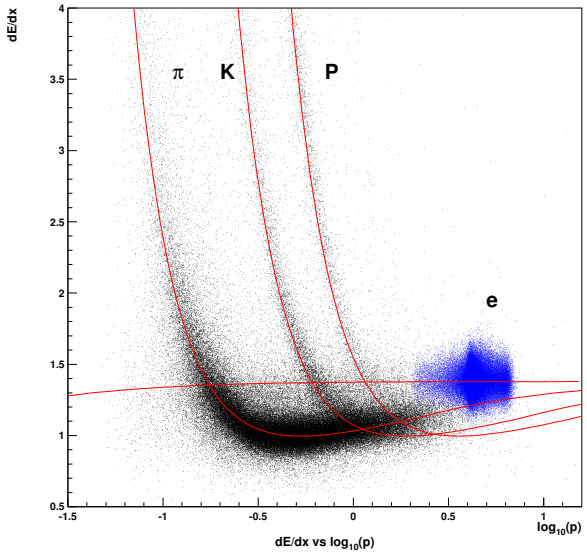

Figure 2.15: The measured dE/dx versus momentum observed in collision data.

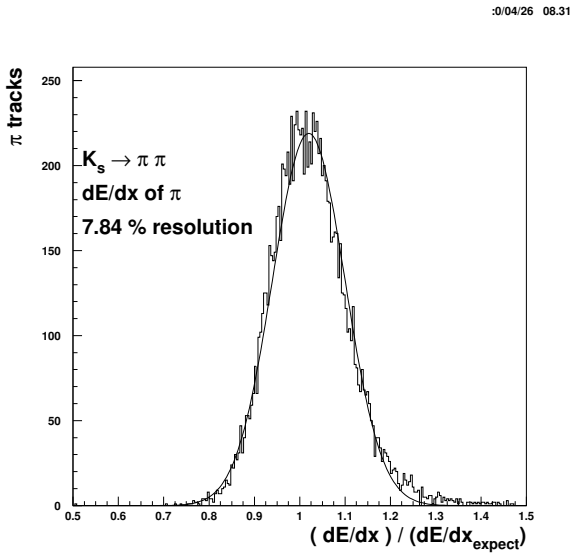

Figure 2.16: Distribution of $(dE/dx)/(dE/dx_{exp})$ for pions from K^0_S decays,where (dE/dx) is the measured specific ionization and (dE/dx_{exp}) is the expectation by Bethe-Bloch formula.

written as

$$m < p\sqrt{n^2 - 1}, \tag{2.2}$$

where m and p are the particle mass and the momentum and n is the refractive index of the matter.

Figure 2.17 shows the configuration of ACC. ACC consists of 960 counter modules segmented into 60 cells in the ϕ direction for the barrel part and 228 modules arranged in 5 concentric layers for the forward endcap part of the detector. Each counter module consists of a block of silica aerogel in an aluminum box of 0.2 mm thickness and one or two fine-mesh type photomultiplier tubes (FM-PMTs) which can work in the 1.5 T magnetic field. The silica aerogel with five different refractive indices, $n = 1.010, 1.013, 1.015, 1.020$ and 1.028 are used for the barrel modules depending on the polar angle. The refractive indices are selected to cover up to the maximum momentum of two body B decays. For the endcap module, the silica aerogel with $n = 1.030$ is used for low momentum particles, which is necessary for flavor tagging, to cover lack of TOF in the endcap. The number of readout channel is 1,560 for the barrel modules and 228 for the endcap modules.

Figure 2.18 shows measured pulse height distributions for barrel ACC for $e^{\pm}$ tracks in Bhabha events and $K^{\pm}$ candidates in hadronic events, where $K^{\pm}$ candidates are selected by TOF and dE/dx measurements, together with the expectations from Monte Carlo simulation. Clear separation between $K^{\pm}$ and $e^{\pm}$ is seen.

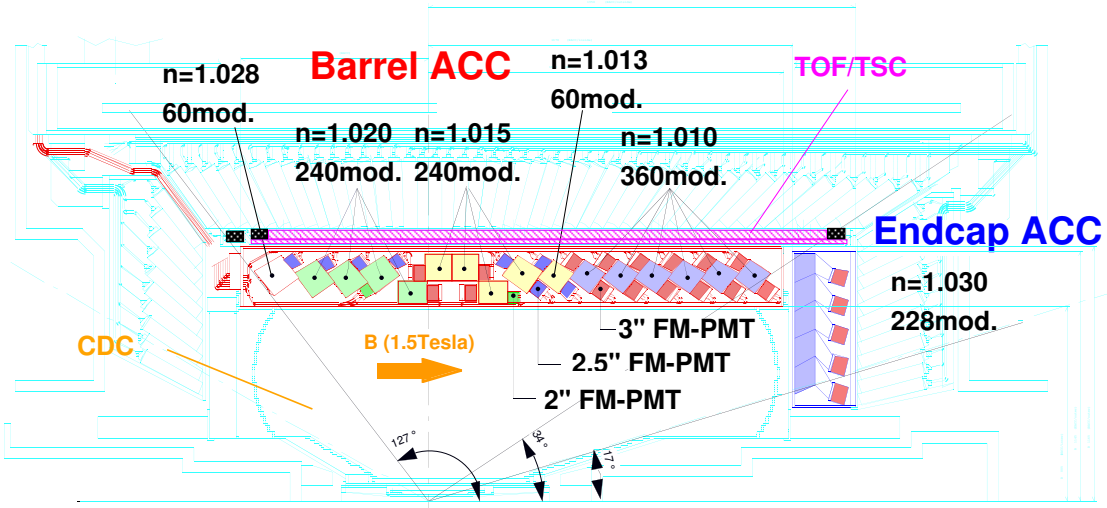

Figure 2.17: The arrangement of ACC.

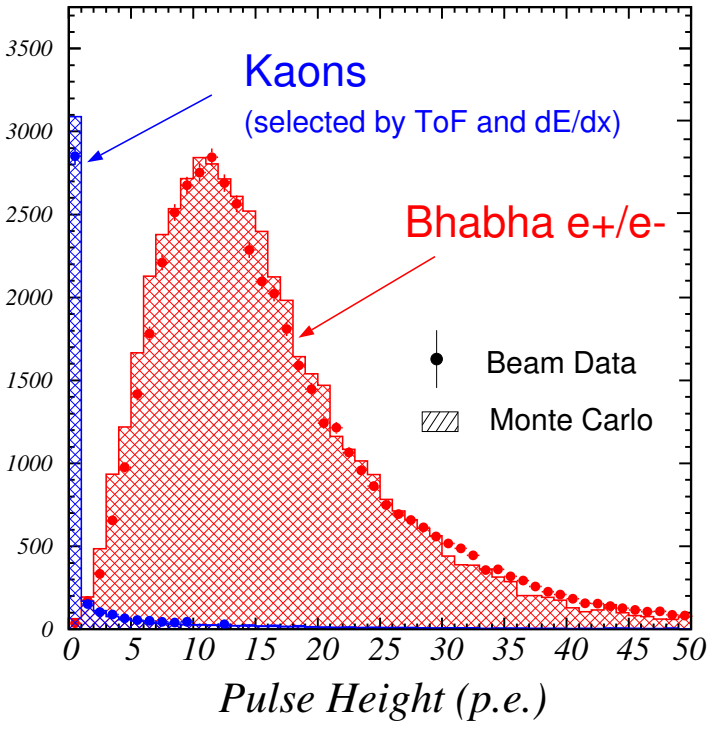

Figure 2.18: Pulse-height spectra in units of photoelectrons observed by barrel ACC for electrons and kaons.

2.2.5 Time of Flight Counter(TOF)

Time of flight counter (TOF) detector system using plastic scintillation counters is used to distinguish $K^{\pm}$ from $\pi^{\pm}$ up to 1.2 GeV/c. TOF measures the elapsed time between a collision at the interaction point and the time when the particle hits the TOF layer. A relation between measured time T and the particle mass m is expressed as

$$m = p\sqrt{\frac{c^2T^2}{L^2} - 1}, \tag{2.3}$$

where p is the particle momentum and L is the flight path length. For $K^{\pm}$ and $\pi^{\pm}$ with a momentum of 1.2 GeV/c and a flight path length of 1.2 m, which is the distance between the interaction point and TOF, give T of 4.3 ns and 4.0 ns, respectively. TOF is designed to have 100 ps time resolution which separate these $K^{\pm}$ and $\pi^{\pm}$ by 3 σ significance. In addition to particle identification, TOF provides fast timing signals for the trigger system. To sustain the fast trigger rate in any beam background condition, the thin trigger scintillation counters (TSC) is appended just inside the TOF counter.

TOF system consists of 128 TOF counters and 64 TSCs. Two trapezoidally shaped TOF counters and one TSC counter form one module. Figure 2.19 shows the configuration of a TOF/TSC module. In total 64 TOF/TSC modules located at a radius of 1.2 m from the interaction point cover a polar angle ranged from 34° to 120°. Each TOF counter is read out by a FM-PMT at each end. Each TSC counter is read out by only one FM-PMT from the backward end. The total number of readout channels is 256 for TOF and 64 for TSC.

Figure 2.20 shows TOF time resolution for forward and backward PMTs and for the weighted average as a function of z position in TOF module measured by μ-pair events. The resolution for the weighted average time is about 100 ps with a small z dependence. Figure 2.21 shows the mass distribution obtained from TOF measurement. Clear peaks corresponding to $\pi^{\pm}$, $K^{\pm}$ and protons are seen. The data points are in good agreement with the Monte Carlo expectation assuming time resolution of 100 ps (histogram).

2.2.6 Electromagnetic Calorimeter(ECL)

The main purpose of the electromagnetic calorimeter (ECL) is the detection of electrons and photons from B meson decays with high efficiency and good energy and position resolutions. For our analysis, ECL plays important role in $J/\psi \to e^+e^-$ reconstruction. Electron identification relies primarily on a comparison of the charged particle track momentum and the its energy deposit in ECL, as described in section 2.5.2. Electrons deposit most of its energy in the ECL by electromagnetic shower, while hadrons or $\mu^{\pm}$ deposit

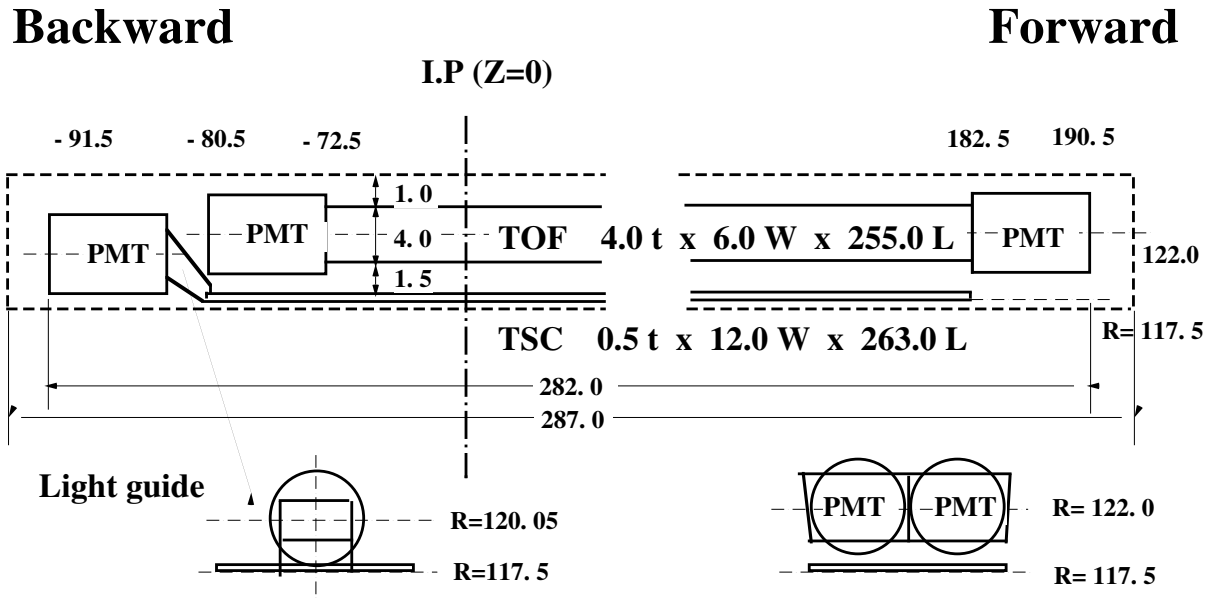

Figure 2.19: Dimensions of a TOF/TSC module.

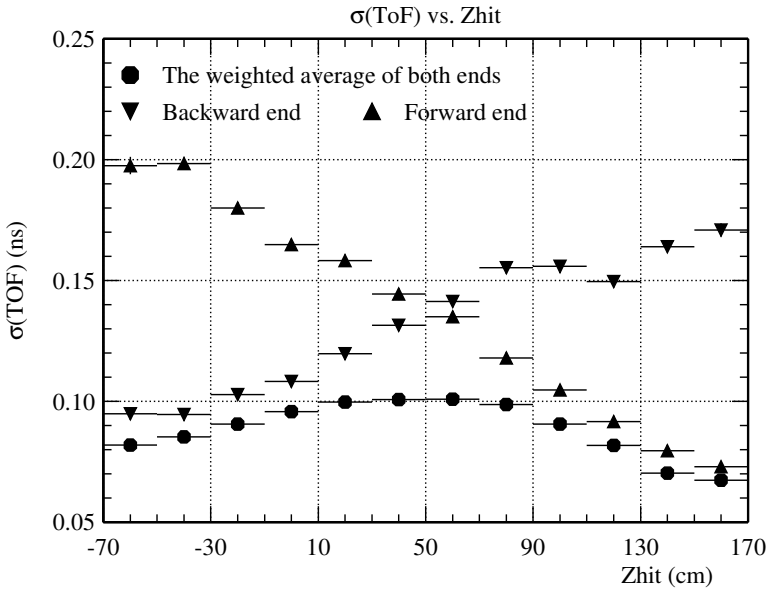

Figure 2.20: Time resolution for μ-pair events.

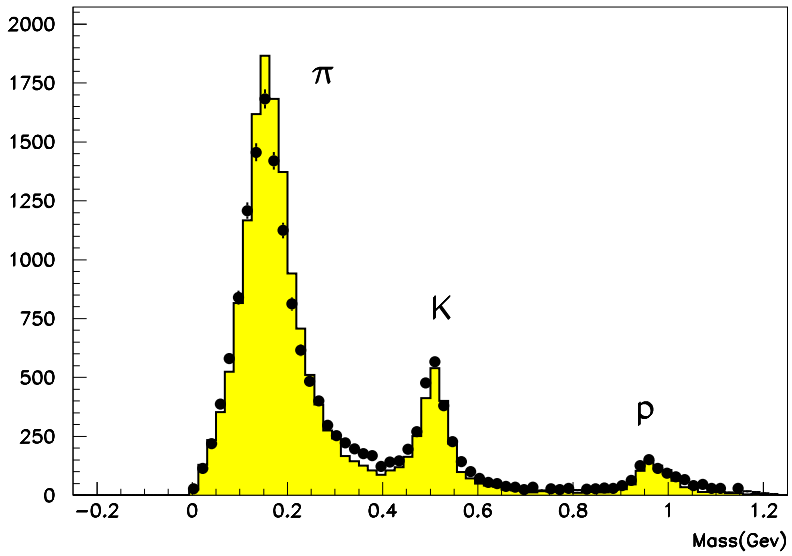

Figure 2.21: Mass distribution from TOF measurement for particle momenta below 1.2GeV/c. Histogram shows the Monte Carlo expectation assuming time resolution of 100 ps. The points with error bars are data.

small fraction of their energies. Thus, good energy resolution of ECL is indispensable for electron identification. In addition to this, we need to detect the photons radiated from the electron or positron in $J/\psi \to e^+e^-$ decays in order to reduce the radiative tail in the invariant mass distribution as described in section 3.4.1.

The overall configuration of the ECL is shown in Figure 2.22. ECL consists of 8,736 thallium doped CsI crystal counters, and the total weight is 43 tons. The calorimeter covers the polar angle region of 17° and 150°, corresponding to a total solid-angle coverage of 91 % of 4π. The barrel part has 6,624 crystals segmented 46 in θ and 144 in ϕ. The forward (backward) endcap has 1,152 (960) crystals segmented 13 (10) in θ and 48-144 (64-144) in ϕ depending on θ. Small gaps between the barrel and endcap crystals provide a path way for cables. The loss of solid angle associated with these gaps is approximately 3 % of the total acceptance.

Each CsI(Tl) crystal has a tower-like shape as shown in Figure 2.23. Typical size of a crystal is 30 cm long, 5.5 cm × 5.5 cm in the front face, and 6.5 cm × 6.5 cm in the rear face, respectively. The length corresponds to 16.2 radiation lengths. According to Monte Carlo simulation, approximately 80% of the total energy deposited by a photon injected at the center of the front face of the crystal is contained in that crystal. A single CsI(Tl) counter is assembled as indicated in Figure 2.24. All sides of the crystal except for the end face for light readout are covered by a single layer of 200 μm thick Teflon. It is then covered by a 25 μm thick layer of aluminaized mylar for light and electrical shielding.

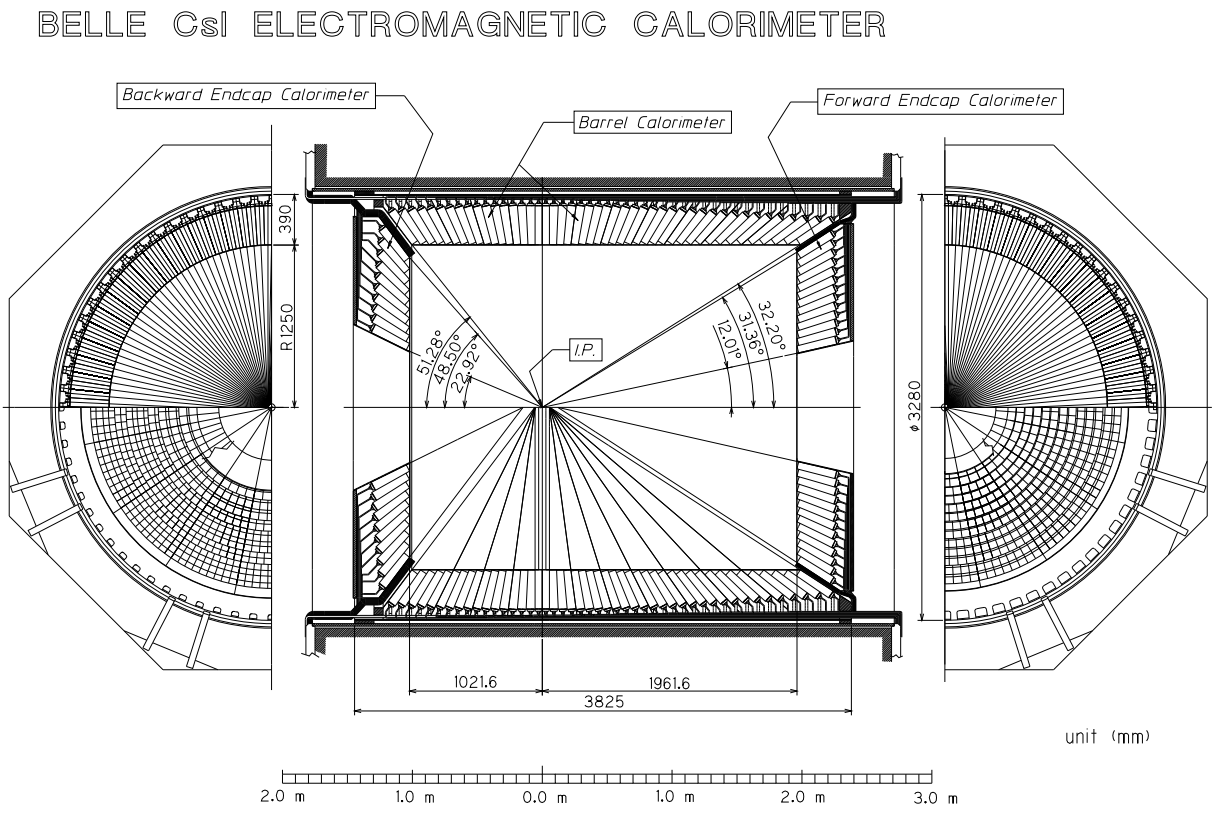

Figure 2.22: Configuration of ECL.

Two photodiodes, each having an active area of 10 mm × 20 mm, are glued at the center of crystal end surface via an acrylic plate of 1 mm thickness.

A block diagram of read out system is shown in Figure 2.25. Each counter has two photodiodes and preamplifiers attached at the end of the crystal in order to read out scintillation. The preamplifier output is transmitted to a shaping circuit where the two signals from the same crystal are summed. Then, the summed signal is split into two streams: one is for the signal to measure energy and the other is for the trigger signal with 200 ns shaping time.

The energy resolution is measured with the beam test before installation into the Belle structure to be $\sigma_E/E = 1.34 \oplus 0.066/E \oplus 0.81/E^{1/4}$ %, where E in GeV. The position resolution is $0.27 + 3.4/E^{1/2} + 1.8/E^{1/4}$ mm. Figure 2.26 shows the energy resolution and the position resolution.

2.2.7 Solenoid Magnet

The super-conducting solenoid provides a magnetic field of 1.5 T over the tracking volume for measurement of charged particle momentum. The super-conducting coil consists of a single layer of niobium-titanium-copper alloy embedded in a high purity aluminum stabilizer. It is wound around the inner surface of an aluminum support cylinder with 3.4 m in diameter and 4.4 m length. Indirect cooling is provided by liquid helium circulating through a tube on the inner surface of the aluminum cylinder. Figure 2.27 shows the structure of the solenoid.

2.2.8 K_L^0 and Muon Detector(KLM)

KLM detects K_L and muons. For our measurement, KLM provides muon detection for J/ψ reconstruction.

KLM consists of alternating layers of charged particle detectors and 4.7 cm thick iron plates. There are 15 resistive plate counter (RPC) superlayers and 14 iron layers in the octagonal barrel region and 14 RPC superlayers in each of the forward and backward endcaps. The iron layers also serve as a return yoke of the magnetic flux provided by the super-conducting solenoid. Figure 2.28 shows the barrel part of the iron yoke. A cross section of a RPC superlayers is shown in Figure 2.29. Each RPC superlayer consists of two RPC modules and provides θ-ϕ two dimensional information. A charged particle traversing the gas gap ionizes the gas and initiates a streamer in the gas. The streamer results in a local discharge of the glass plates. This discharge is limited by the high resistivity of the plates and induces a signal on external pickup strips. The iron plates provide a total of 3.9 hadronic interaction lengths for a particle traveling normal to the

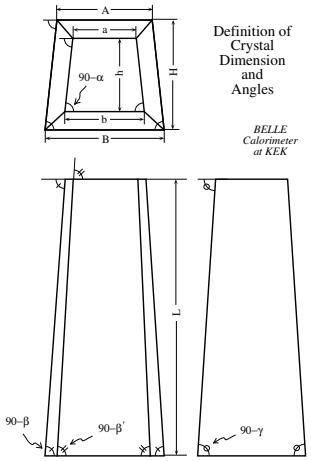

Figure 2.23: The CsI(Tl) crystal shape.

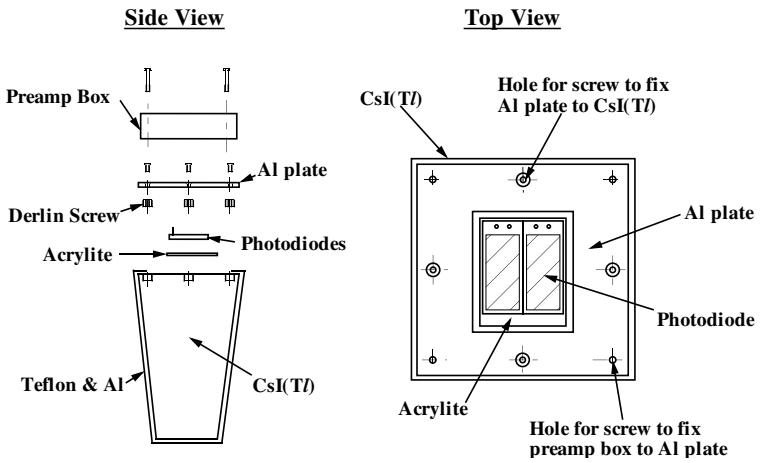

Figure 2.24: The mechanical assembly of the CsI(Tl) counter.

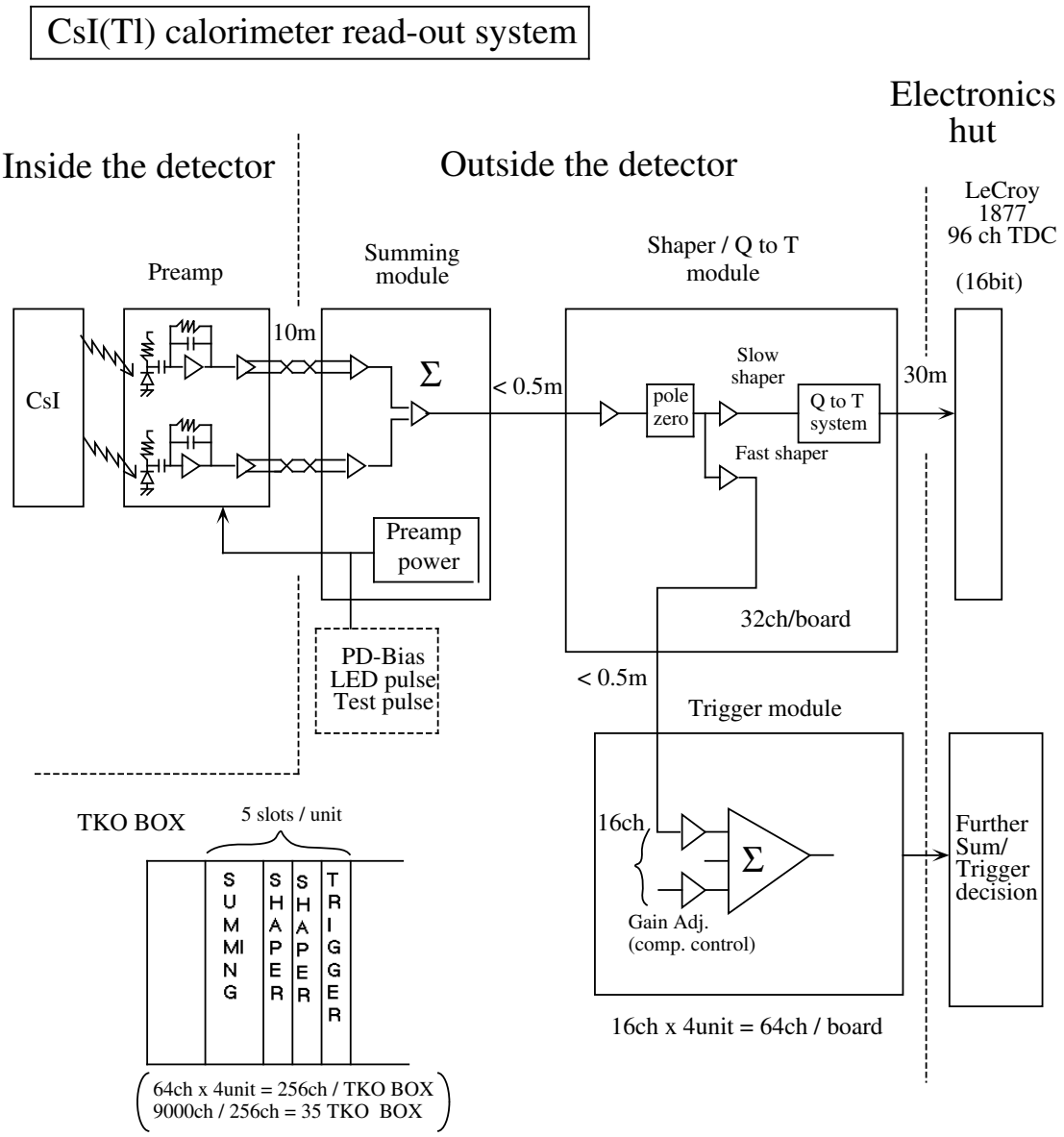

Figure 2.25: Block diagram of the CsI(Tl) readout electronics.

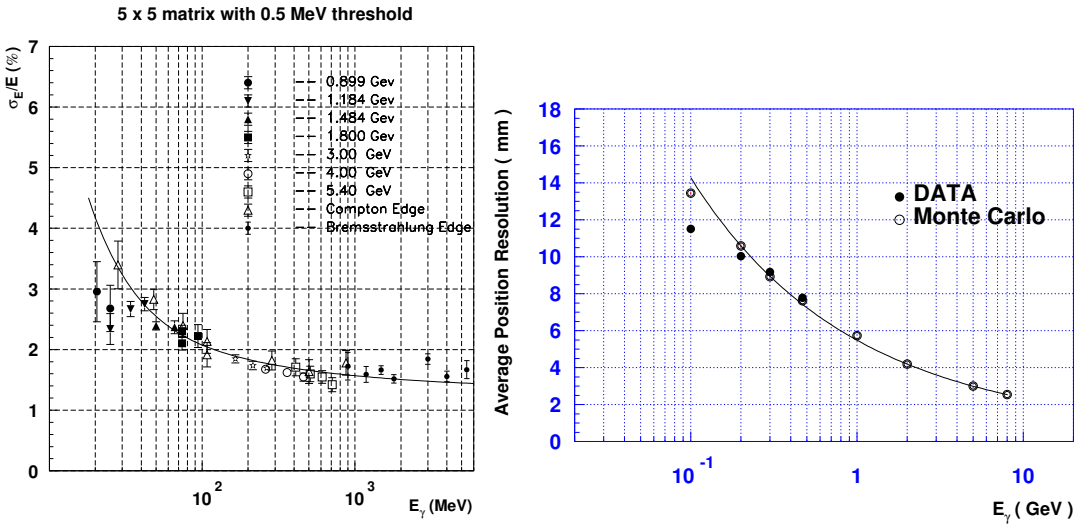

Figure 2.26: The energy resolution (left) and the position resolution (right) of ECL as a function of incident photon energy.

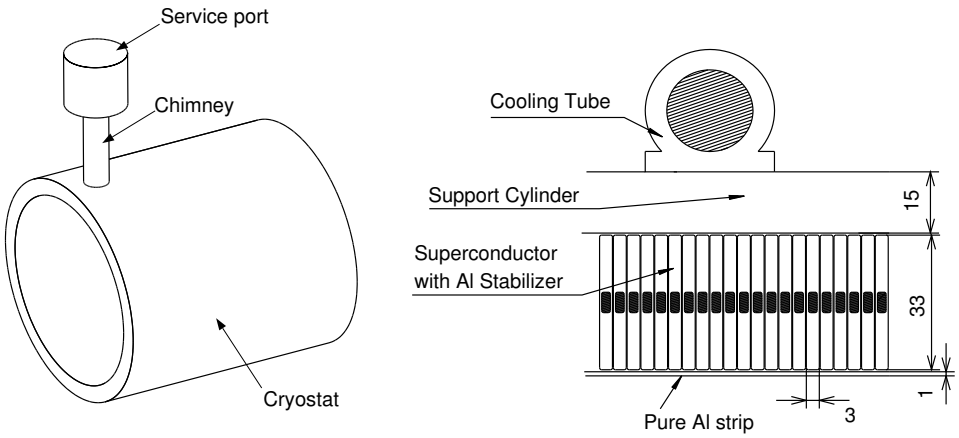

(a) Outlook of the magnet

(b) Cross sectional view of the coil

Figure 2.27: An outlook of the solenoid and the cross-sectional view of the coil. The unit is mm.

detector planes. K_L interacting with the iron produces a hadronic shower of ionizing particles and is detected by RPC layers.

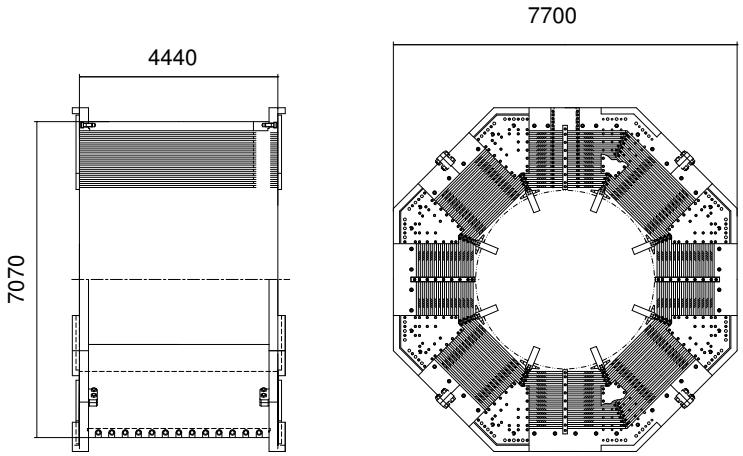

Figure 2.28: Barrel part of the iron yoke. The unit is mm.

2.2.9 Trigger and Data acquisition

The trigger system is required to catch $B\overline{B}$ event by ~ 100 % efficiency, while it is needed to suppress the trigger rate for uninteresting events. Because of the high beam current of KEKB, the trigger suffers from severe beam background. Since the beam background rates are very sensitive to actual accelerator conditions, it is difficult to make a reliable estimation. Therefore, the trigger system is required to be flexible so that background rates are kept within the tolerance of the data acquisition bandwidth and is also needed to have redundant triggers to keep the high trigger efficiency for physics events of interest.

Figure 2.30 shows a schematic view of the Belle Level 1 trigger system. It consists of the sub-detector trigger systems and the central trigger system called the global decision logic (GDL). The GDL combines the sub-detector trigger signals and make a final decision to initiate a Belle wide data acquisition within 2.2 μs from beam crossing. There are two major types of triggers prepared for the hadronic events. One is based on the charged track information from CDC. The other is provided by the energy information from ECL. These two redundant triggers provide more than 99.5 % trigger efficiency for $B\overline{B}$ events.

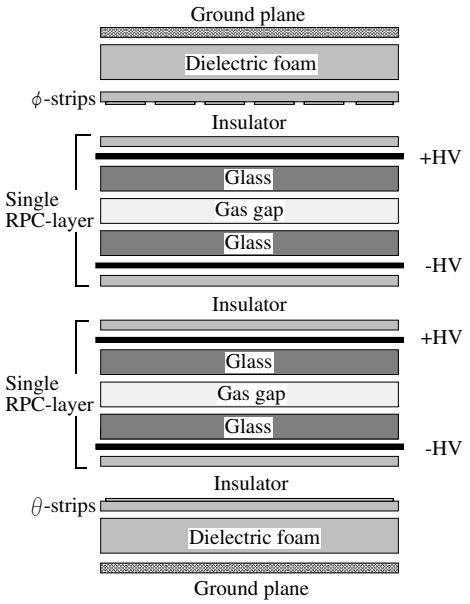

Figure 2.29: Cross section of a KLM super-layer.

The typical trigger rate is 300-350 Hz.

A schematic view of the Belle data acquisition system is shown in Figure 2.31. In order to keep DAQ dead time fraction less than 10 % up to a maximum trigger rate of 500Hz, the entire system is segmented into 7 subsystems running in parallel. The signals from sub-detectors are converted to timing signals by the Q-to-T converters (MQT300A) except for KLM and SVD and digitized by FASTBUS multi hit TDC (LRS1877S). KLM hits are processed by the multiplexer system and fed to LRS1877S. SVD signals digitized by the flush ADC system and processed by DSP (Digital Signal Processing) for noise reduction. The data of each subsystem are sent to the event builder. The event builder converts "detector-by-detector" parallel data streams to an "event-by-event" data river and sent the data to an online computer farm. The online computer formats an event data into an offline event format and performs a background reduction (the Level 3 trigger) after a fast event reconstruction. The data are then sent to a mass storage system located at the computer center 2 km away via optical fibers. A typical event data size is about 30 kB, which corresponds to the maximum data rate of 15 MB/s.

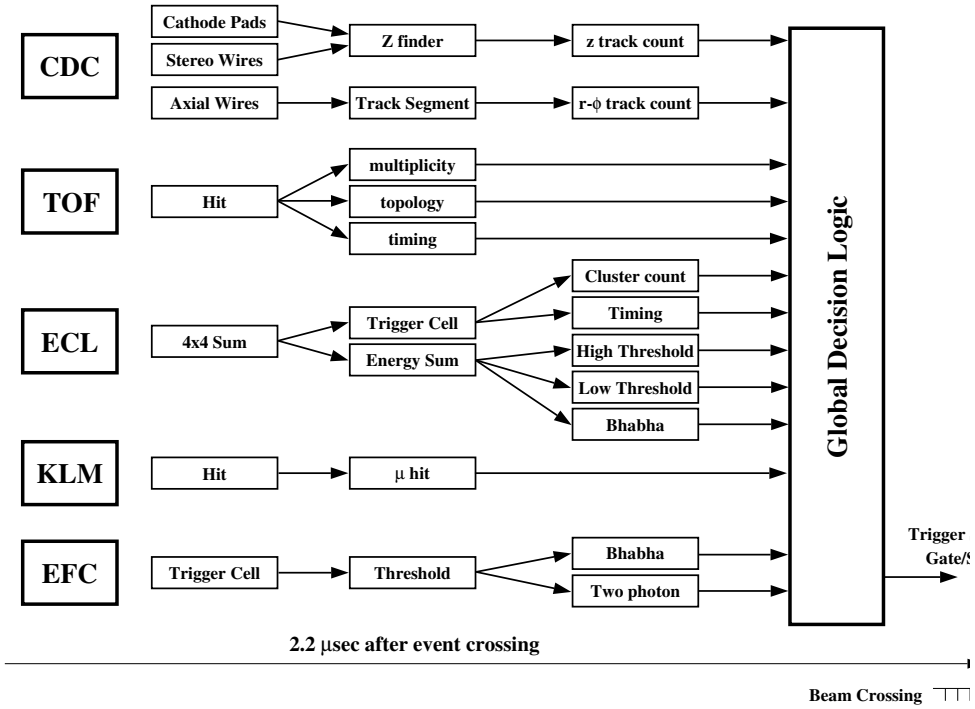

Figure 2.30: The Level-1 trigger system for the Belle detector.

2.2.10 Offline Software and Computing

Collected data by the Belle detector are analyzed at the offline computer farm. To cope with large data which accumulate at a rate of 400 GB a day, the parallel processing scheme by multi-CPU-servers is developed. Belle has a PC farm equivalent to 650 GHz Pentium III for data analysis. The PC farm is capable of processing ~ 2 fb^{-1} data a day.

All software for the data acquisition and the data analysis except for a few HEP specific and non HEP specific free software packages has been developed by the members of the Belle collaboration. In particular, the mechanisms to process events in parallel on large SMP (Symmetric Multiple Processor) computer servers have been developed locally using C and C++ programming languages. The users' reconstruction and analysis codes run on the event processing framework, called BASF (Belle AnalySis Framework), as modules and are linked dynamically at the run time. The BASF takes care of input/output of event data, parallel processing and HBOOK[30] output.

2.3 Monte Carlo Simulation

An important part of high physics data analysis is comparing real data to Monte Carlo expectations using simulated data. This enables the detector response to certain process

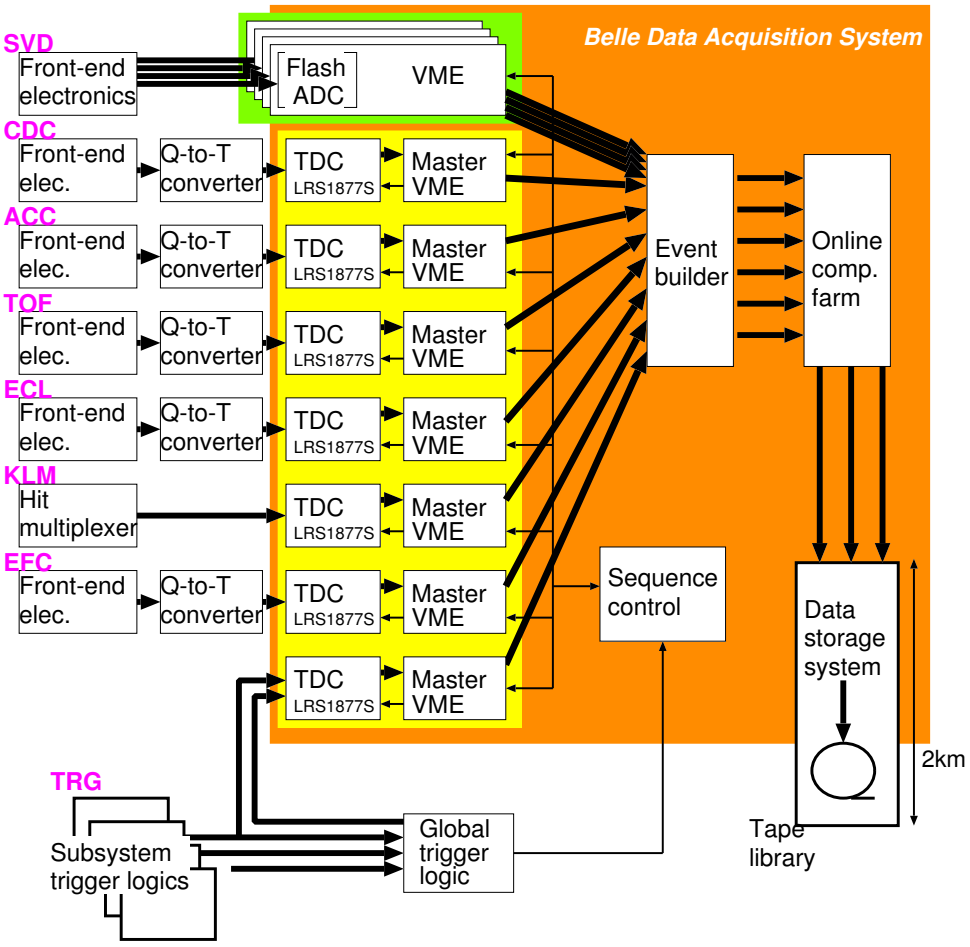

Figure 2.31: Belle DAQ system overview.

to be predicted and understood. It is vital for our understanding of how efficiently the Belle detector will record specific types of events. Monte Carlo is also used to study the detector response to very rare types of events, enabling us to deduce ways to increase the sensitivity to such events.

Generating Monte Carlo data takes place in two stage. First, the underlying particle physics process, such as collision and subsequent decays of daughter particles, are simulated. Then, the detector response to these particles is simulated. The first step uses the EvtGen package[32] [33]. It incorporates particle properties compiled from many experiments in the form of world averages and also position entries. The Monte Carlo simulation data used in this analysis is described in section 3.2.

The generated events are then passed to a BASF module called GSIM. This module simulates the detector response and is very computationally intensive. GSIM is based on the CERN package GEANT3[37] and simulates the interactions between the final state particles and the detector. The simulated data is then reconstructed in the same way as real data with the final MDSTs containing the additional event generator information.

Many efforts are made to keep the simulation as accurate as possible. Background events are added by taking random trigger events and inserting them into the Monte Carlo data set. The varying size and position of the IP is incorporated as well as any changes in the sub-detectors, such as dead channels.

2.4 Particle Reconstruction

The final state particles' energy, momentum and species have to be reconstructed from the recorded detector hits. In this chapter, the key reconstruction techniques for charged particles and showers are described.

2.4.1 Charged particle reconstruction

The first step of charged particle reconstruction is finding track-segment-hit-patterns in the CDC. The tracks projected onto the $r - \phi$ plane are searched for with axial wire hits, then hits of the stereo wires are used to determine z positions of the track. Track parameters (momentum and position) of the found track are obtained by the fitting based on the Kalman filter technique [38], which minimizes the effects of the multiple Coulomb scattering and non-uniformity of the magnetic field in the CDC in the determination of the track parameters. Then, all of the hit points are connected and fitted to a helix to obtain the particle momentum and position. Finally, the reconstructed charged particle trajectory is extrapolated toward the SVD to be connected to the SVD hits to improve

the resolution of track parameters. Here, the track parameters are computed again with combination of the hits on the CDC and the SVD.

The track momenta are calibrated by a scaling constant so that reconstructed invariant masses of $J/\psi \to \mu^+\mu^-$ and $D^0 \to K^-\pi^+$ decays become consistent with the world averages. The calibrations are made for every run range typically a few month data taking. The major source of a change in the calibration constant comes from the fluctuation of a current supplied to the solenoid magnet and the amount of the correction is $\mathcal{O}(10^{-3})$. The estimated errors of track parameters are also calibrated by a scaling constant using the cosmic ray events in which a cosmic ray particle penetrates detector and is recognized by the track finding algorithm as two individual tracks. Since the "two" tracks must possess same track parameters, the difference between these "two" tracks is suitable to calibrate the estimated errors of the track parameters. Typical amounts of the corrections by the scaling constants are 10 - 15 %.

2.4.2 Shower reconstruction

Photon or electron cause electromagnetic shower at the CsI(Tl) crystal in the ECL, then its energy is measured. An electromagnetic shower spreads over several crystals that are neighboring each other. Therefore, such a group of crystal hits, which is called cluster, has to be found to reconstruct a shower. First, a local maximum energy crystal, whose energy deposit exceeds 10 MeV, is picked up as a "seed crystal". The surrounding crystals of 5×5 matrix is the basis of the shower reconstruction. Figure 2.32 shows the cluster of 5×5 crystals.

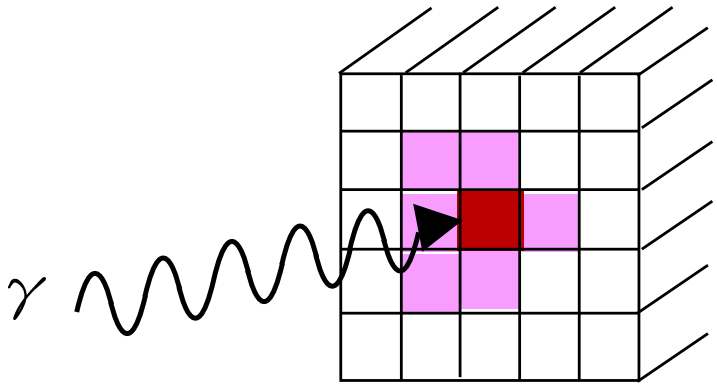

Figure 2.32: Schematic view of the shower reconstruction based on the cluster of 5×5 crystals. Hatched crystal with most dark color is a seed crystal, and the hatched one with lighter color denote the recorded hits.

The crystal hits less than 0.5 MeV are suppressed by the readout TDC(LRS 1877S).

All the recorded hits(i.e. at least 0.5 MeV) in the 5×5 matrix are summed up to get the incident particle's energy. The incident position is calculated by the energy-weighted average position of the recorded crystal hits inside 5×5 matrix. Here, since naive calculations of the energy and position have some systematic behavior due to electromagnetic shower development characteristics and finite crystal size(∼5.5×5.5 cm at the front face), so we apply the appropriate corrections which are determined by Monte Carlo simulation.

To check the matching among the reconstructed showers and tracks, a track is extrapolated up to the calorimeter crystal front face. When the extrapolated track go across a CsI crystal front face, the shower including the hit crystal, where the extrapolated track arrived, is regarded as an associated shower with the charged track.

Among the showers that are not associated with any charged tracks, we accept all the reconstructed ones as photons if they exceed 0.5 GeV. Below 0.5 GeV, we require the following criteria to be recognized as a photon; having at least 20 MeV, shower width is less than 6 cm and E9/E25 is greater than 0.75, where, shower width is the lateral spread of the shower calculated as the energy-weighted distance between crystal hits and the shower center, E9/E25 means the ratio of between the energies contained by 3×3 and 5×5 crystal matrices surrounding the seed crystal.

2.5 Particle Identification

The particle identification play an important role in efficient reconstruction of particle. In this section, the method of particle identification is described.

2.5.1 $K^{\pm}/\pi^{\pm}$ Identification

In this analysis, the separation of kaons from pions is crucial for eliminating bacgrounds coming from $B^0 \to J/\psi K^{(*)}$ decays. The $K^{\pm}/\pi^{\pm}$ identification is carried out by combining information: dE/dx measurement by CDC, information from TOF, and measurement of the number of photoelectrons in the ACC. For each charged track, we calculate probability with kaon and pion hypothesis for each sub-detector. The probabilities of each sub-detector is combined to form a likelihood ratio defined as $PID(K) \equiv P_K/(P_K+P_\pi)$, where P_K and P_π are product of sub-detectors' probabilities for $K^{\pm}$ and $\pi^{\pm}$, respectively. The $K^{\pm}/\pi^{\pm}$ identification is performed with the $PID(K)$. The $K^{\pm}$ identification efficiency and wrong identification probability of $\pi^{\pm}$ as $K^{\pm}$ measured with $D^{*\pm} \to D^0(\to K^{\mp}\pi^{\pm})\pi^{\pm}$ decays are shown in Figure 2.33. For most of the momentum region, the measured $K^{\pm}$ identification efficiency exceeds 80 %, while the π fake rate is kept below 10 %. This performance allows us to reduce backgrounds by rejecting the tracks identified as charged

K.

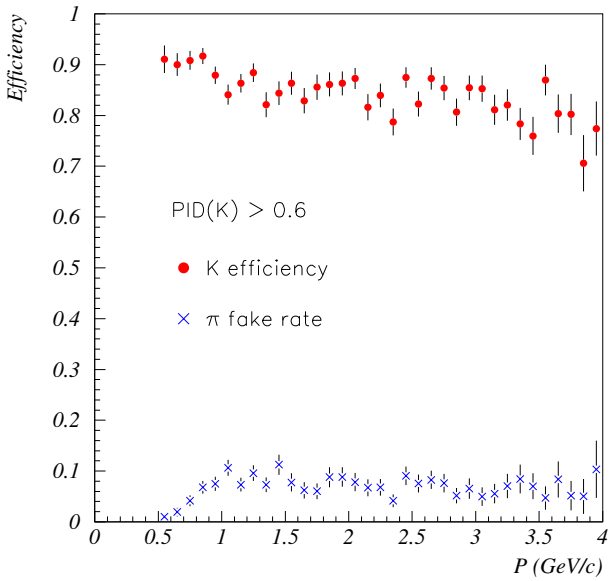

Figure 2.33: K efficiency and π fake rate as a function of momentum.

2.5.2 Electron Identification

For electron identification, we use the following discriminants that are based on the information from CDC and ECL.

- Matching of an extrapolated track position and a cluster position in the ECL
  It is important for electron identification to find out a right combination of a cluster and track position. The ECL cluster position is determined by the center-of -gravity of the ECL hits in the cluster as described in section 2.4.2. Figure 2.34 shows the difference in ϕ ($\Delta\phi$) and θ ($\Delta\theta$) between a cluster position and a position of an extrapolated electron track. Since the lateral spread of electron is narrower than that of hadronic showers, the electron's cluster position matches with the extrapolated track position better than that of hadron's.

  Using the $\Delta\phi$ and $\Delta\theta$, we form the matching χ^2 to identify electrons as follows:

$$\chi^2 \equiv \left(\frac{\Delta\phi}{\sigma_{\Delta\phi}}\right)^2 + \left(\frac{\Delta\theta}{\sigma_{\Delta\theta}}\right)^2$$

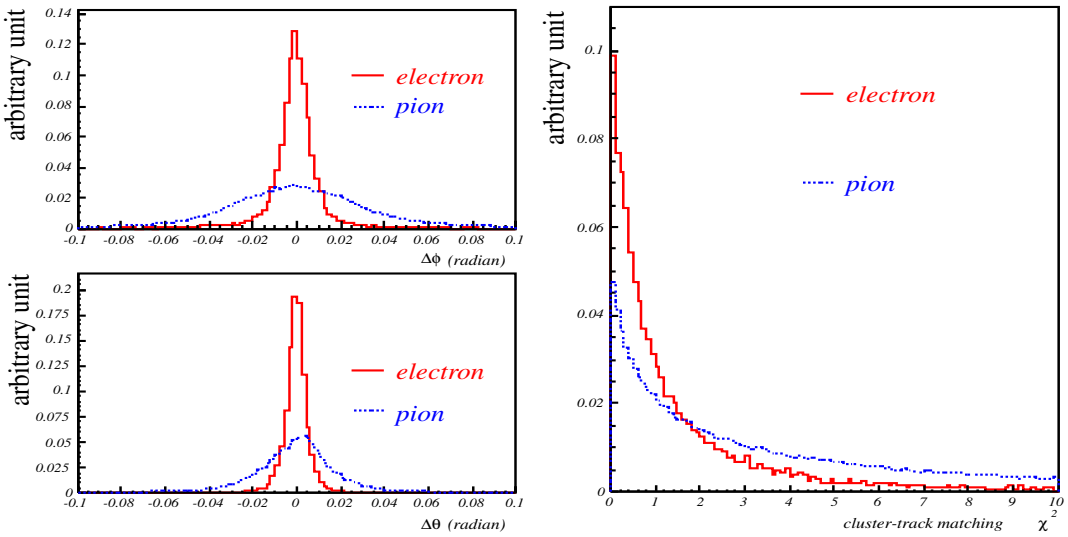

Figure 2.34: $\Delta\phi$ (left, top), $\Delta\theta$ (left, bottom), and cluster-track matching χ^2 (right) distributions for electrons and charged pions.

where $\sigma_{\Delta\phi}$ and $\sigma_{\Delta\theta}$ are the widths obtained by fitting the $\Delta\phi$ and $\Delta\theta$ distribution of electrons with Gaussian. The χ^2 distributions for electrons and charged pions are shown in Figure 2.34 For each charged track, a cluster that gives the minimum χ^2 and that have the χ^2 less than 50, is take for the matched cluster.

- Ratio of cluster energy measured by ECL (E) and charged track momentum (p) measured by CDC : E/p

  The E/p is use as a powerful discriminant to distinguish electrons from hadrons. Since electron deposites almost all energy in ECL, the electron's E/p becomes close to unity. While, the deposit energy of hadrons in ECL is smaller than their momentum ($E < p$). Figure 2.35 shows E/p distribution for electrons and pions. The momentum range is 0.5 GeV/$c < p_{lab} <$ 3.0 GeV/c in the laboratory frame. The tail in the lower E/p side of electrons comes from interaction of electrons with materials in front and the shower leakage in ECL. As shown in Figure 2.35 which shows the momentum dependence of E/p, E/p is more efficient in high momentum region.

- Shower shape

  Since electromagnetic shower and hadronic shower have different shape in both transverse and longitudinal directions, this difference can be used as a significant discriminant. The shower shape in the transverse direction can be evaluated with $E9/E25$, which is defined as a ratio of energy summed in 3 $\times$ 3 crystals to that in 5 $\times$ 5 crystals. Figure 2.36 shows $E9/E25$ for electrons and charged pions. Electrons

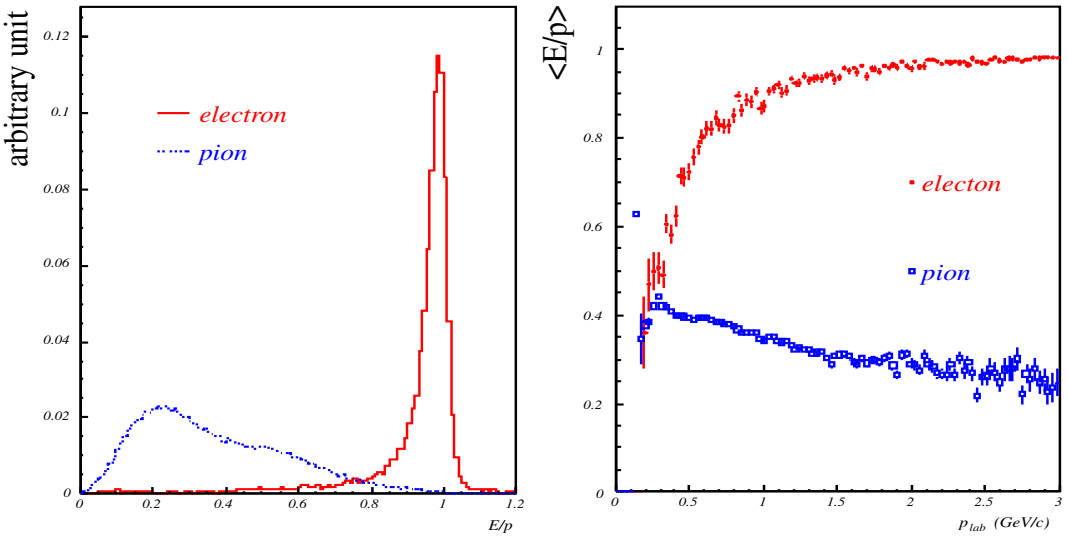

Figure 2.35: E/p distribution (left) and momentum dependence distribution of E/p (right) for electrons and charged pions.

have a peak at around 0.95 with relatively small low-side tail, while pions have more events in the lower $E9/E25$ region.

- dE/dx measurement by CDC
  Energy deposit in CDC is measured as dE/dx. As shown in Figure 2.37 which shows dE/dx of electrons and pions, the $dEdx$ enables us to distinguish electrons and hadrons effectively. The averaged dE/dx as a function of momentum is shown in Figure 2.37. From the distribution, the separating power is higher in the lower momentum region and this feature is supplementary to the ability of E/p.

In addition to above discriminants, light yield in ACC is also incorporated for the electron identification to eliminate kaons. The likelihood ratio $\mathcal{L}_e$ computed with combination of above quantities is defined as

$$\mathcal{L}_e = \frac{\prod_i P_e(i)}{\prod_i P_e(i) + \prod_i P_h(i)}$$

where $P_e(i)$ and $P_h(i)$ are the probabilities to identify electrons and hadrons respectively, which are calculated from i-th discriminator. Figure 2.38 shows the electron identification efficiency measured with $e^+e^- \to e^+e^-e^+e^-$ data and the fake rate for charged pions from $K^0_S \to \pi^+\pi^-$ decays as a function of momentum. The efficiency of electron identification is greater than 90 % and the hadron fake rate is less than 1% for $p_{lab} > 1$ GeV/c. The detailed description of electron identification are given in [39].

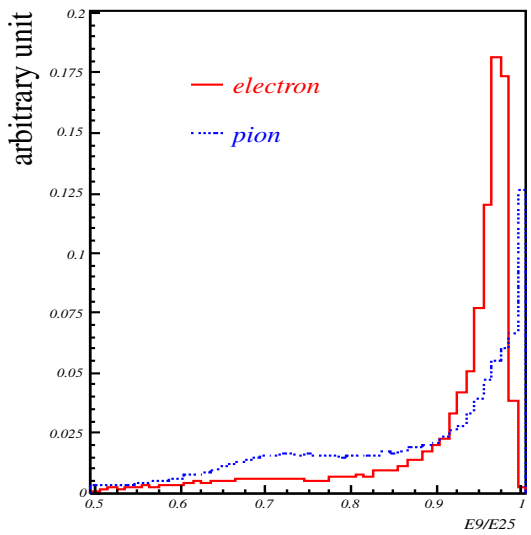

Figure 2.36: $E9/E25$ distribution for electrons and pions

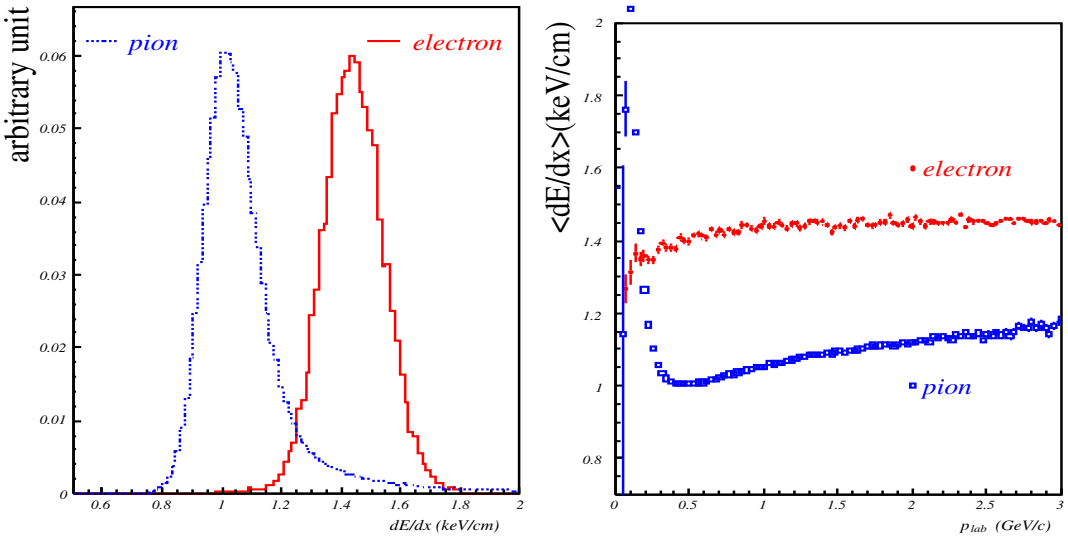

Figure 2.37: dE/dx distribution (left) and momentum dependence distribution of dE/dx (right) for electrons and charged pions.

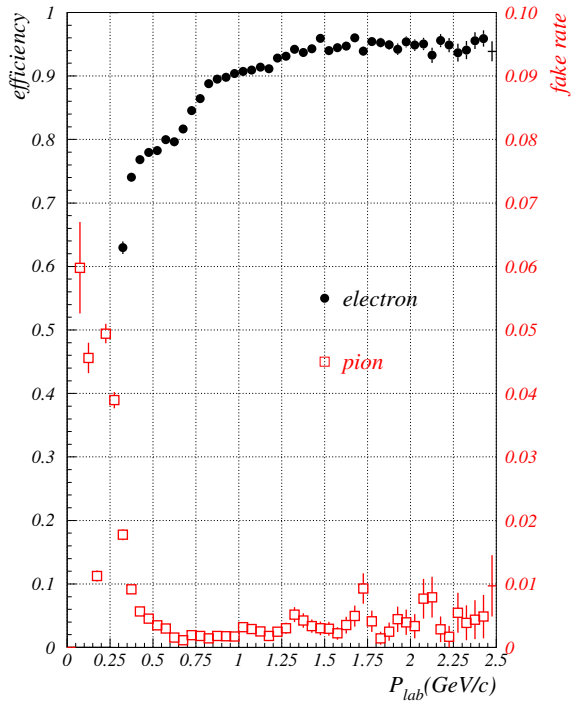

Figure 2.38: Electron identification efficiency (circles) and fake rate for charged pions (squares). Note the different scales for the efficiency and fake rate.

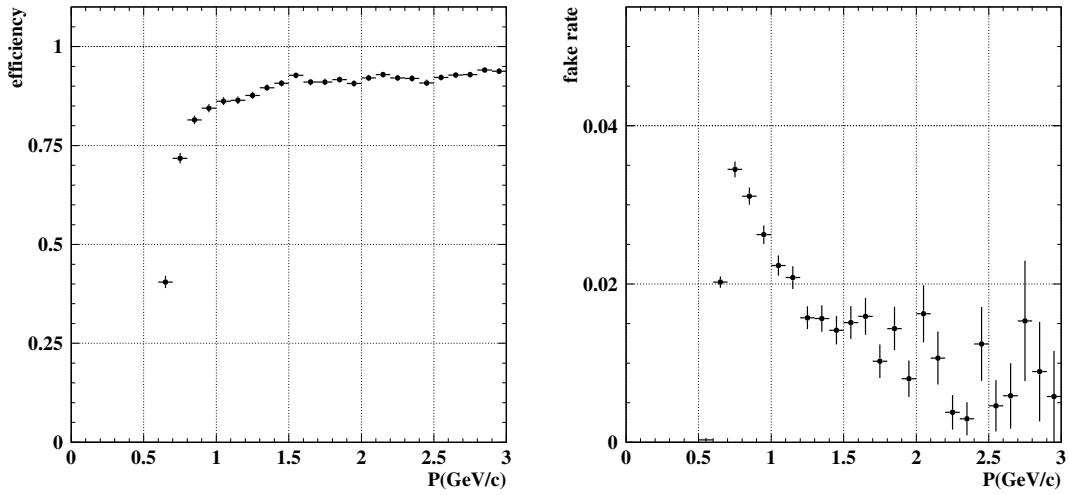

Figure 2.39: Muon identification efficiency versus momentum in KLM (left). Fake rate for charged pions versus momentum in KLM (right).

2.5.3 Muon Identification

KLM provides muon identification for charged particles with momenta greater than 0.6 GeV/c. Charged particles with momenta less than 0.6 GeV/c cannot reach KLM. The muon identification is performed based on the range and the transverse scattering in KLM. Muons pass through KLM with small deflections, while hadrons, which are dominated by pions, are deflected by the strong interaction with iron and then stop within less iron layers than muons. These information is parametrized by the number of penetrated iron plates and the reduced χ^2 calculated with the extrapolated charged track and the position of KLM hits. A likelihood ratio of the muon hypothesis and the pion hypothesis is made combining these two information and is used to separate muons from hadrons. Figure 2.39 shows the muon identification efficiency measured with cosmic muons as a function of momentum and the fake rate for $\pi^{\pm}$ measured with $K^0_S \to \pi^+\pi^-$ decays. Typical efficiency for momentum grater than 1 GeV/c is better than 90 %, while fake rate for $\pi^{\pm}$ is smaller than 2 %. The details of muon identification are given in Ref.[40].

Chapter 3

Event Selection and Reconstruction

In this chapter, we describe the procedure of event selection and reconstruction for $B^0 \to J/\psi\pi^+\pi^-$ candidates. First, we select hadronic events from the data sample collected by the Belle detector. Next, we reconstruct J/ψ then combine $\pi^+\pi^-$ to reconstruct B meson candidates.

3.1 Data Sample

The data sample used for this analysis is collected by the Belle detector from January 2000 to July 2005. The integrated luminosity at the $\Upsilon(4S)$ resonance is 414 fb^{-1}, corresponding to 449 million $B\overline{B}$ pairs. The obtained data is filtered by requiring the hadronic event selection described in section 3.3, then processed by further reconstruction procedure to obtain $B^0 \to J/\psi\pi^+\pi^-$ candidates.

3.2 Monte Carlo sample

As describe in the earlier chapter, in order to know the detection efficiency for $B^0 \to J/\psi\pi^+\pi^-$ signal decays and to estimate a background, a Monte Carlo (MC) simulation data has to be prepared. In this subsection, the Monte Carlo datasets used in this analysis is briefly described. The events are generated by the EvtGen software that is described in the section 2.3 by specifying the proper B decay model and giving an appropriate input parameters.

3.2.1 Signal Monte Carlo

As described in section 1.3 , there can be several sources of the di-pion system in $B^0 \to J/\psi\pi^+\pi^-$ decays. The $B^0 \to J/\psi\rho^0$ is known to contribute predominantly. About other possible resonant contributions, a hint of $B^0 \to J/\psi f_2$ are gotten as described in the next

chapter. Therefore the Monte Carlo sample for these two decay modes are prepared. In order to generate the $B^0 \to J/\psi\rho^0$ Monte Carlo events, the `SVV_HELAMP` decay model is used. This decay model is the proper one to treat the B meson decay into two vector mesons. The polarization parameters are set to be same as $B \to J/\psi K^*$ mode[43], as it can be regarded as a reasonable assumption to estimate the detection efficiency. The $\rho^0 \to \pi^+\pi^-$ decay is treated by the `VSS` decay model that carries out a vector particle decay into two spin-less particles. The $B^0 \to J/\psi f_2$ Monte Carlo events are generated by the model in which B^0 decays into J/ψ and f_2 according to the available phase space distribution, that is called `PHSP` model. The f_2 decay into $\pi^+\pi^-$ is taken care by the `TSS` decay model that handle the kinematics tensor decay to two spin-less particles. The B^0 decay into J/ψ, π^+ and π^- with `PHSP` model is also simulated, in order to model non-resonant $B^0 \to J/\psi\pi^+\pi^-$ and to estimate the detection efficiency as a function of the di-pion invariant mass ($M_{\pi^+\pi^-}$). The decay model used here are described in Ref.[42]. Table 3.1 summarizes the Monte Carlo samples for different di-pion components among $B^0 \to J/\psi\pi^+\pi^-$ final states considered in this analysis. Each B^0

B^0 Decay Channel	Number of Events	Decay model
$B^0 \to J/\psi\rho^0$	100,000	`SVV_HELAMP`
$B^0 \to J/\psi f_2$	100,000	`PHSP` and `TSS`
$B \to J/\psi\pi^+\pi^-$ non-resonant	100,000	`PHSP`

Table 3.1: The Monte Carlo sample to treat various B^0 decays into $J/\psi\pi^+\pi^-$.

decay channel is generated 100,000 events and processed by GSIM detector simulation and reconstruction programs for two different detector configuration, SVD1 (till 2003 summer) and SVD2 (after 2003 summer).

3.2.2 Inclusive J/ψ Monte Carlo

In the analysis presented in section 3.5 and later, the background estimation is carried out by the inclusive J/ψ Monte Carlo[41] that is the simulated $B\overline{B}$ events in which one of the B decays into the final state having a J/ψ. Not only the J/ψ directly coming from B but also the higher charmonium states decaying into J/ψ, e.g. $\psi(2S)$, χ_{c0}, χ_{c1} and χ_{c2} are also taken into account. In the inclusive J/ψ Monte Carlo sample the J/ψ coming from one of the B is forced to decay to either electron or muon pair because these are the only decay modes in which J/ψ is reconstructed in this analysis. The amount of the simulated events is equivalent to 3.88×10^{10} $B\overline{B}$.

3.3 Hadronic Event Selection

The data sample contains not only $\Upsilon(4S)$ production but also several other processes such as continuum $e^+e^- \to q\overline{q}$ ($q = u, d, s, c$) processes, muon pair productions, tau pair productions, Bhabha (including radiative Bhabha) and two-photon ($\gamma\gamma \to q\overline{q}$) processes. The cross section of these processes are listed in Table 3.2. The data sample also contains cosmic ray events, and beam background, which occur from spent electrons that are off the beam orbit due to the bremsstrahlung, and the interactions between the electron (or positron) and beam gas. To suppress these unnecessary events and to select hadronic

Process	Cross section (nb)
$e^+e^- \to \Upsilon(4S)$	1.2
$e^+e^- \to q\overline{q}$ ($q = u, d, s, c$)	2.8
$e^+e^- \to l^+l^-$ ($l = \mu, \tau$)	1.6
Bhabha ($\theta_{lab} > 17°$)	44.
two-photon ($\theta_{lab} > 17°$, $p_t > 0.1$ GeV)	~ 15

Table 3.2: Cross section for each process in e^+e^- collisions at the center of mass energy of $\sqrt{s} = 10.58$ GeV [44]. θ_{lab} and p_t are the polar angle in the laboratory frame and p_t is transverse momentum of the final state particle, respectively.

events that comes from continuum and $\Upsilon(4S)$ production, we apply the following requirements:

- The number of good charged tracks ≥ 3.
  Where the good charged track is defined to satisfy (1) transverse momentum, $P_t > 0.1$ GeV/c, (2) the impact parameter to the nominal interaction point in the x-y plane, $|dr| < 2.0$ cm, (3) the impact parameter to the nominal interaction point along z-axis, $|dz| < 4.0$ cm.

  This requirement is effective to suppress Bhabha and μ pair productions. It also reduces the cosmic rays and the beam background because the tracks from these events come from arbitrary points while the tracks from hadronic events come from the nominal interaction point.

- At least one "good" ECL cluster should be within the fiducial volume of $-0.7 < \cos\theta < 0.9$. The good ECL cluster is defined as the cluster having the energy more than 100 MeV. This requirement reduces Bhabha events because most clusters for Bhabha events have a very shallow angle.

- The total visible energy $E_{vis} > 0.2\sqrt{s}$ where $\sqrt{s}$ represents the cms (center of mass system) energy of $\Upsilon(4S)$. The E_{vis} is calculated from the good tracks assuming the pion mass and good photons in an event, where the good photon is defined as the good ECL cluster within the CDC acceptance ($17° < \theta < 150°$ in the laboratory frame) with no associated tracks from the CDC.

- The energy sum of the good ECL clusters within the CDC acceptance, E_{sum} is required to satisfy

$$0.1 < E_{sum}/\sqrt{s} < 0.8.$$

- The average cluster energy defined as E_{sum}/(Number of good ECL cluster), including the ones outside the CDC acceptance, is required to be

$$E_{sum}/(\text{Number of good ECL cluster}) < 1 \text{ GeV}.$$

  This requirement is used to suppress the Bhabha process.

- The momentum sum of good tracks and good photons is required to be balanced in the z direction in the cms to eliminate the beam background.

$$|P_z| < 0.5\sqrt{s}$$

- The position of the primary vertex is required to satisfy $|r_{vertex}| < 1.5$ cm and $|z_{vertex}| < 3.5$ cm, where primary vertex is obtained from all good charged tracks, r and z represent the position of the primary vertex in the r-ϕ plane and the z-axis, respectively.

- To suppress tau pair, beam gas, and two-photon events and to regain continuum events which are inconsistent with tau pair events, we adopt the following requirements. At first, we separate the event into two hemispheres by a plane perpendicular to the event thrust axis, then the invariant mass of tracks in each hemisphere is calculated assuming a pion mass for each track. In tau pair events, this invariant mass does not exceed tau mass. In the event, we regard the lager invariant mass as heavy jet mass, M_{jet}. It is required to satisfy

$$M_{jet} > 1.8 GeV/c^2 \text{ or } E_{sum}\sqrt{s} > 0.18 \text{ or } M_{jet}/E_{vis} > 0.25$$

  where E_{sum} includes the cluster outside the CDC acceptance.

The efficiencies of the hadronic event selection is 99.1 % for $B\overline{B}$ events and 79.5 % for continuum process, while the contamination of the non-hadronic components is less than 5 % [45].

3.4 $B^0 \to J/\psi\pi^+\pi^-$ Reconstruction

To suppress continuum process, we require the event shape variable R_2 to be less than 0.5, where R_2 is the ratio of the second to the zeroth Fox-Wolfram moment [46]. R_2 is defined as

$$R_2 \equiv \frac{\sum_i^N \sum_j^N [|\vec{p_i}||\vec{p_j}| \cdot (3\cos^2\phi_{ij} - 1)]}{2\sum_i^N \sum_j^N [|\vec{p_i}||\vec{p_j}|]} \tag{3.1}$$

where $\vec{p_i}$ is a momentum vector of i-th particle, ϕ_{ij} is an angle between $\vec{p_i}$ and $\vec{p_j}$ in the cms, and N is a total number of particles in the event. For jet-like events, such as continuum, most $\cos\phi_{ij}$ are likely to be $\sim \pm 1$ and the denominator in Equation 3.1 becomes similar number. Therefore R_2 becomes 1 in the limits of narrowest two-jet event. While, in the case of spherical events like B decays, $R_2 \simeq 0$. The efficiency loss due to R_2 selection is estimated to be smaller than 0.5 % [45].

In order for J/ψ mesons reconstruction and charged pion pairs forming, the charged tracks are required to have $|dz| < 5$cm and 0.4 rad $< \theta <$ 2.43 rad, where dz is the z component of the track's closest approach with respect to the origin and θ is polar angle of the track. The former requirement is introduced to eliminate the wrongly reconstructed tracks and the latter is to require the tracks to be detected within good fiducial volume throughout SVD1 and SVD2 data as shown in Figure 3.1. With this θ requirement, the detection efficiencies are almost identical between SVD1 and SVD2 environment (see section 4.4, Table 4.6).

3.4.1 Reconstruction of J/ψ

J/ψ mesons are reconstructed via their decays into opposite charged lepton pairs (e^+e^- or $\mu^+\mu^-$). Both lepton tracks must be identified to have opposite charges.

In the e^+e^- mode, ECL clusters that are within 50 mrad of the track's initial momentum vector are included in the calculation of the invariant mass, in order to include photons radiated from electrons/positrons. The invariant mass $M_{l^+l^-}$ ($l = e$ or μ) is calculated

$$M^2_{l^+l^-} = \left(\sqrt{M_l^2 + |\vec{p_{l^+}}|^2} + \sqrt{M_l^2 + |\vec{p_{l^-}}|^2}\right)^2 - |\vec{p_{l^+}} + \vec{p_{l^-}}|^2, \tag{3.2}$$

where e^+e^- case, $\vec{p_{l^+}}$ and $\vec{p_{l^-}}$ are the corrected with the four-momentum of the included photons. Figure 3.2 (a) and (b) show the invariant mass distributions of e^+e^- pairs for

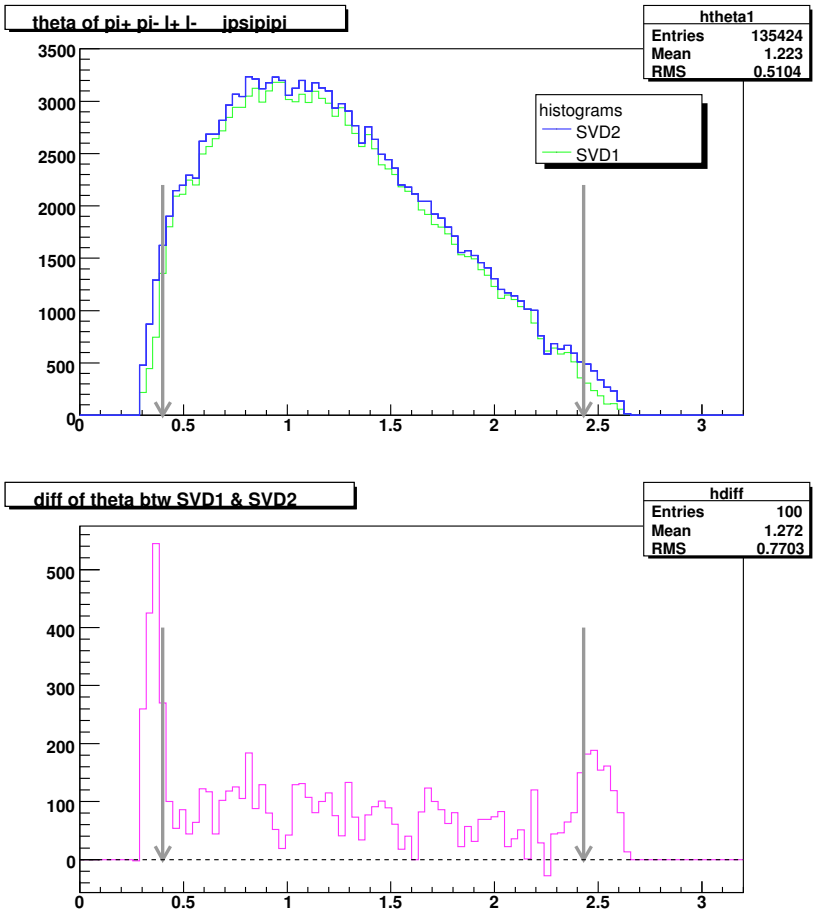

Figure 3.1: Charged tracks' θ distribution for $B^0 \to J/\psi\pi^+\pi^-$ phase space (PHSP) signal Monte Carlo. Here, 100,000 events are generated for both of each SVD1 and SVD2 Monte Carlo. Upper: Comparison between two Monte Carlo datasets processed under SVD1 and SVD2 environment. Lower: Difference between the number of tracks as a function of θ. The arrows show the window to accept tracks to reconstruct B candidates.

Monte Carlo and experimental data, where the arrows indicate the edges of the mass window. Although the radiative photon's effect is included, a broad tail in the lower mass region is seen in the distribution. It is due to absorption of photon by the material in front of the ECL. Thus, the invariant masses of e^+e^-, $M_{e^+e^-}$, is required to satisfy the range $-150\ \mathrm{MeV}/c^2 < (M_{e^+e^-} - M_{J/\psi}) < 36\ \mathrm{MeV}/c^2$. Here $M_{J/\psi}$ denotes the world average of the J/ψ mass [16]. Figure 3.2 (c) and (d) show the invariant mass distributions of $\mu^+\mu^-$ pairs. For the invariant mass of $\mu^+\mu^-$, $M_{\mu^+\mu^-}$, it is required to satisfy $-60\ \mathrm{MeV}/c^2 < (M_{\mu^+\mu^-} - M_{J/\psi}) < 36\ \mathrm{MeV}/c^2$. The invariant mass window is asymmetric due to missing energy carried away by radiative photon, though the effect is much smaller than e^+e^- case.

For the J/ψ candidate events after the invariant mass selection, we apply the fit with vertex and mass constraint, where we vary the momentum of lepton tracks within their error under the constraint that these tracks come from same decay vertex point, and the invariant masses of lepton pair become the world average J/ψ mass. It improves the reconstructed B^0 momentum resolution.

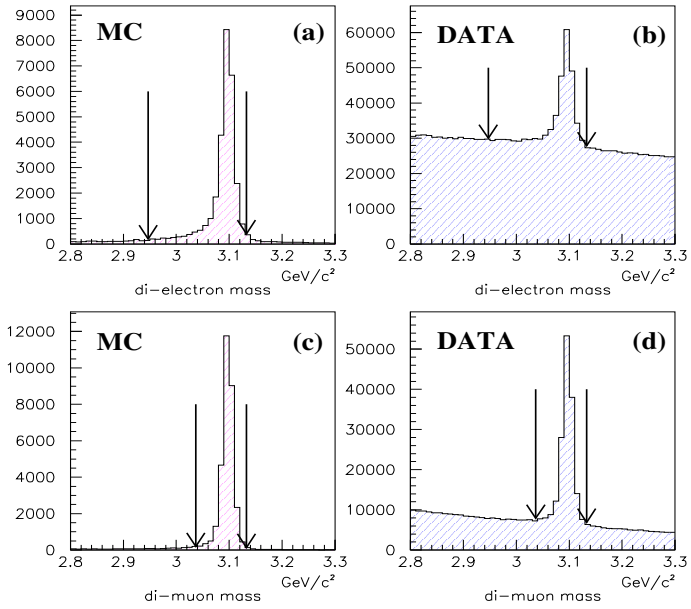

Figure 3.2: The invariant mass distribution of electron pairs for (a) $B^0 \to J/\psi\pi^+\pi-$ PHSP signal Monte Carlo 100,000 events and (b) data, muon pairs for (c) $B^0 \to J/\psi\pi^+\pi^-$ PHSP signal Monte Carlo and (d) data. Arrows indicate the invariant mass ranges.

3.4.2 Reconstruction of B^0

J/ψ and two charged pions are combined to form B candidates. The B candidate selection is carried out using two observables in the $\Upsilon(4S)$ cms, i.e., the beam-energy constrained mass ($M_{\rm bc}$) and the energy difference (ΔE), which are defined as follows:

$$M_{\rm bc} = \sqrt{(E^*_{beam})^2 - \sum_i |\vec{p^*_i}|^2}, \tag{3.3}$$

$$\Delta E = \sum_i E^*_i - E^*_{beam}, \tag{3.4}$$

where $E_{\rm beam} = \sqrt{s}/2$ is the cms beam energy, and $\vec{p_i}^*$ and E^*_i are the cms three-momenta and energies of the B meson decay products, respectively. In order to improve ΔE and

$M_{\rm bc}$ resolutions, we applied the fit with vertex to $\pi^+\pi^-$ pairs. To reduce the $B^0 \to J/\psi K^0_S$ events and the backgrounds due to accidentally formed pion pairs, we require the distance between the reconstructed vertices of the J/ψ and the $\pi^+\pi^-$ pair to be less than 3 mm.

The fraction that we find more than one $J/\psi\pi^+\pi^-$ combination in $-0.2 < \Delta E < 0.2$ and $5.2{\rm GeV}/c^2 < M_{\rm bc}$ in a event is 14 %. The candidate events are selected by requiring the smallest χ^2 of the vertex fit of charged pion tracks in the final state, because such multiple candidate events are totally due to the number of $\pi^+\pi^-$ combination in the event.

The B meson signal region is defined as $5.27\ {\rm GeV}/c^2 < M_{\rm bc} < 5.29\ {\rm GeV}/c^2$ and $-0.04\ {\rm GeV} < \Delta E < 0.04\ {\rm GeV}$. Figure 3.3 and 3.4 show scatter plot of $M_{\rm bc}$ and ΔE for signal Monte Carlo and data sample. The number of reconstructed $B^0 \to J/\psi\pi^+\pi^-$ candidates passing the all selection criteria is 1098 events.

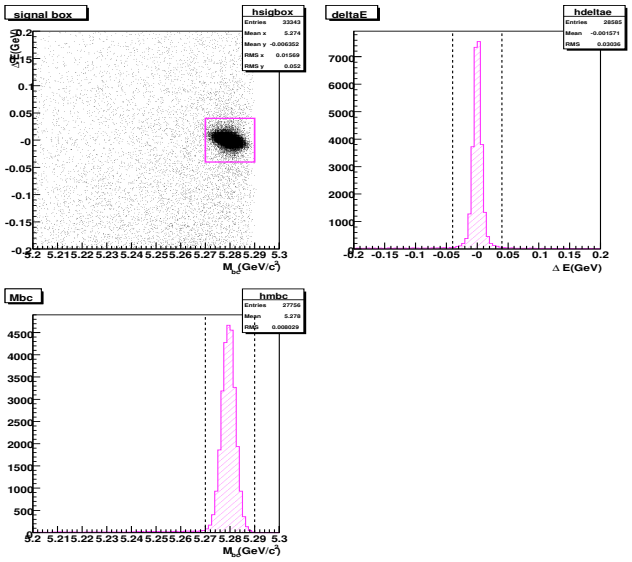

Figure 3.3: Upper left: $M_{\rm bc}$-ΔE 2D distribution, upper right: ΔE projection in $5.27 < M_{\rm bc} < 5.29\ {\rm GeV}/c^2$, lower: $M_{\rm bc}$ projection in $-0.04 < \Delta E < 0.04$ GeV for $B^0 \to J/\psi\pi^+\pi^-$ PHSP signal Monte Carlo 100,000 events. Dashed lines indicate the signal region.

3.5 Inclusive J/ψ Background

Since the main background source is B meson decays having a J/ψ, we checked the background components using the inclusive J/ψ Monte Carlo sample (see section 3.2.2). Table 3.3 shows the remained background events of the decays in the signal box.

Some decay modes make a peak structure at signal value of $M_{\rm bc}$. The order of the branching fraction for these decays is 1.0×10^{-3} which is far greater than the signal

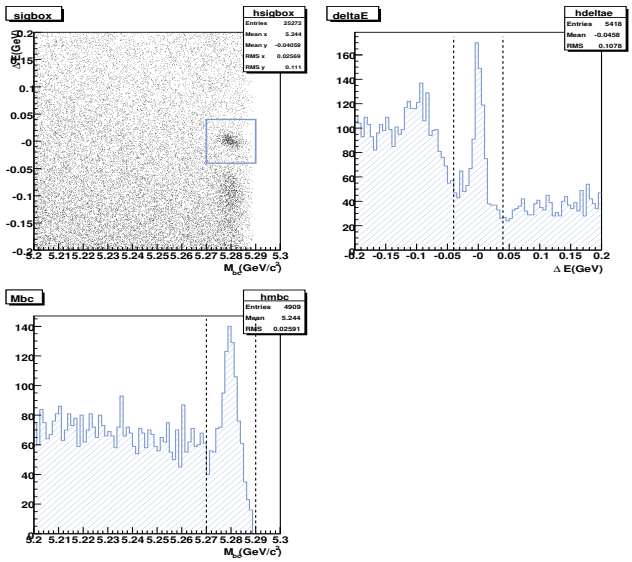

Figure 3.4: Upper left: $M_{\rm bc}$-ΔE 2D distribution, upper right: ΔE projection in $5.27 < M_{\rm bc} < 5.29$ GeV/c^2, lower: $M_{\rm bc}$ projection in $-0.04 < \Delta E < 0.04$ GeV for candidate events found in the experimental data corresponding to 449 million $B\overline{B}$. Dashed lines indicate the signal region.

Neutral B Monte Carlo	
$B^0 \to J/\psi K^0_S$	261
$B^0 \to J/\psi K^*(892)^0$	150
$B^0 \to J/\psi K_1(1270)^0$	30
$B^0 \to J/\psi K^0 \pi^+ \pi^-$	24
$B^0 \to J/\psi K^\pm \pi^\mp \pi^0$	23
$B^0 \to J/\psi K^*_2(1430)^0$	18
$B^0 \to J/\psi$ others	518
total	1025 (events)

Charged B Monte Carlo	
$B^\pm \to J/\psi K^*(892)^\pm$	118
$B^\pm \to J/\psi K_1(1270)^\pm$	47
$B^\pm \to J/\psi K^\pm \pi^+ \pi^-$	24
$B^\pm \to J/\psi K^0 \pi^\pm \pi^0$	20
$B^\pm \to J/\psi K^*_2(1430)^\pm$	16
$B^\pm \to J/\psi \rho^\pm$	18
$B^\pm \to J/\psi$ others	95
total	338 (events)

Table 3.3: Background B decay modes expected with the inclusive J/ψ Monte Carlo sample that corresponds to $3.88 \times 10^{10} B\overline{B}$

branching fraction (due to the extra level of Cabibbo suppression in $B^0 \to J/\psi\rho^0$ decay). This background is therefore a potential problem, but it can be separated using ΔE distribution.

3.5.1 ΔE distribution

The experimental data ΔE distribution superimposed with the background expectation obtained by inclusive J/ψ Monte Carlo is shown in Figure 3.5. The ΔE distribution for $J/\psi K^*(K^+\pi^-)$ peaks at a lower value ($\Delta E \sim -0.12$ GeV) than that for signal, this is due to assigning the mass of the pion to kaon in the construction of the B candidate. And there is no peak structure around zero in ΔE projection except for $B^0 \to J/\psi K^0_S(\to \pi^+\pi^-)$. In the inclusive J/ψ Monte Carlo, $B^0 \to J/\psi K^*_0(1430)^0$ and $B^0 \to K^*_2(1430)^0$ are also taken into account[47]. The branching fraction of each background mode is summarized in Table 3.4.

Since the peaking structure in the signal region is $B^0 \to J/\psi K^0_S$ only, it's contribution can be easily subtracted by using $M_{\pi^+\pi^-}$ distribution as described in section 4.4.2. Because there is no peaking structure in the signal region except for it, the $B^0 \to J/\psi\pi^+\pi^-$ signal yield can be obtained by the fit to this ΔE distribution. A detailed explanation is mentioned in the next chapter.

Background mode	Branching Fraction
$B^0 \to J/\psi K^0_S$	(8.72 $\pm$ 033) $\times 10^{-4}$
$B^0 \to J/\psi K^*(892)^0$	(1.33 $\pm$ 0.06) $\times 10^{-3}$
$B^0 \to J/\psi K^*_0(1430)^0$	5.0 $\times 10^{-5}$ $*$
$B^0 \to J/\psi K^*_2(1430)^0$	2.6 $\times 10^{-4}$ $*$
$B^0 \to J/\psi K^\pm$	(1.008 $\pm$ 0.035) $\times 10^{-3}$
$B^0 \to J/\psi \pi^\pm$	(4.9 $\pm$ 0.6) $\times 10^{-5}$

Table 3.4: Branching fraction for each decay mode in ΔE background. The values marked by $*$ are the ones in the EvtGen program, otherwise the value and uncertainty are taken from the PDG[16].

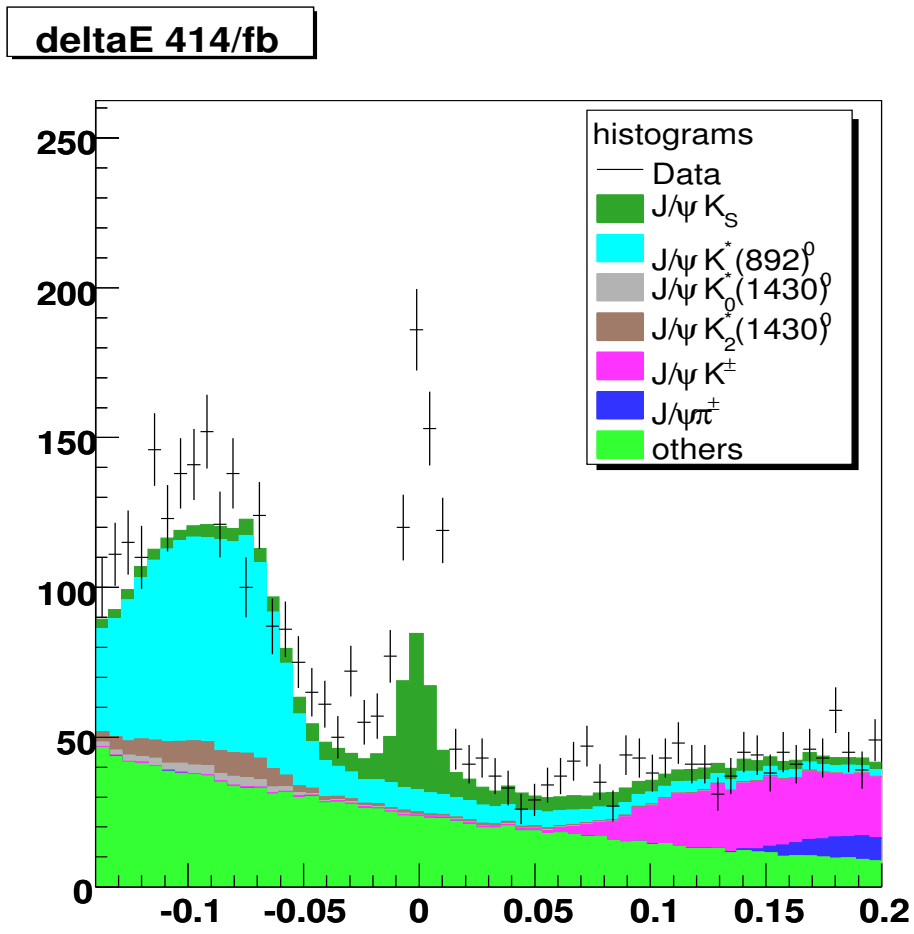

Figure 3.5: ΔE distribution of experimental data(dots with error bar) superimposed with the background expectation obtained by inclusive J/ψ Monte Carlo(histograms) in 5.27 GeV/c^2< $M_{\rm bc}$ < 5.29 GeV/c^2. Note that the contribution named "Others" contains only $B \to J/\psi X$ other than $B \to J/\psi K^{(*)}$ and $B^{\pm} \to J/\psi\pi^{\pm}$ modes; i.e. the continuum background ($e^+e^- \to u\overline{u}, d\overline{d}, s\overline{s}$ and $c\overline{c}$) is not considered in the background expectation shown here.

Chapter 4

Measurement of the Branching Fractions

4.1 Signal yield extraction

4.1.1 Fitting to the ΔE distribution

As mentioned in the previous section 3.5.1, The $B^0 \to J/\psi\pi^+\pi^-$ signal yield is obtained by the fit to the ΔE distribution. The signal distribution is expressed by Gaussian. Among $B \to J/\psi X$ backgrounds, ΔE distributions for the decays,

$$B^0 \to J/\psi K^{*0}, \quad B^0 \to J/\psi K_0^*(1430)^0, \quad B^0 \to J/\psi K_2^*(1430)^0,$$
$$B^\pm \to J/\psi K^\pm \quad \text{and} \quad B^\pm \to J/\psi \pi^\pm,$$

are expressed by smoothed histograms according to the Monte Carlo simulation, because the branching fractions for these B decay modes are relatively well-measured[16]. Other backgrounds do not form significant peaking structure so that their sum up is expressed as a 1st order polynomial. The fit result is shown in Figure 4.1. The peak around $\Delta E = 0$ comes from $B^0 \to J/\psi\pi^+\pi^-$ signal and $B^0 \to J/\psi K_S^0(\to \pi^+\pi^-)$, and correspond to 435 ± 29 events. The $B^0 \to J/\psi K_S^0$ subtraction is done by $M_{\pi^+\pi^-}$ distribution to obtain the net $B^0 \to J/\psi\pi^+\pi^-$ signal yield. To obtain the number of $J/\psi K_S^0$, a fitting to the $M_{\pi^+\pi^-}$ is performed. The function used in the fit is a double Gaussian, because the natural width of the K_S^0 is so small that the observed distribution is completely dominated by the Gaussian detector resolution. First, their mass, width values and the ratio of fitted yields between two Gaussian components are determined by fitting the $M_{\pi^+\pi^-}$ distribution with Monte Carlo expectation (see Figure 4.2). The resultant numbers are summarized in Table 4.1. Then the fit to the data is performed with fixing those values

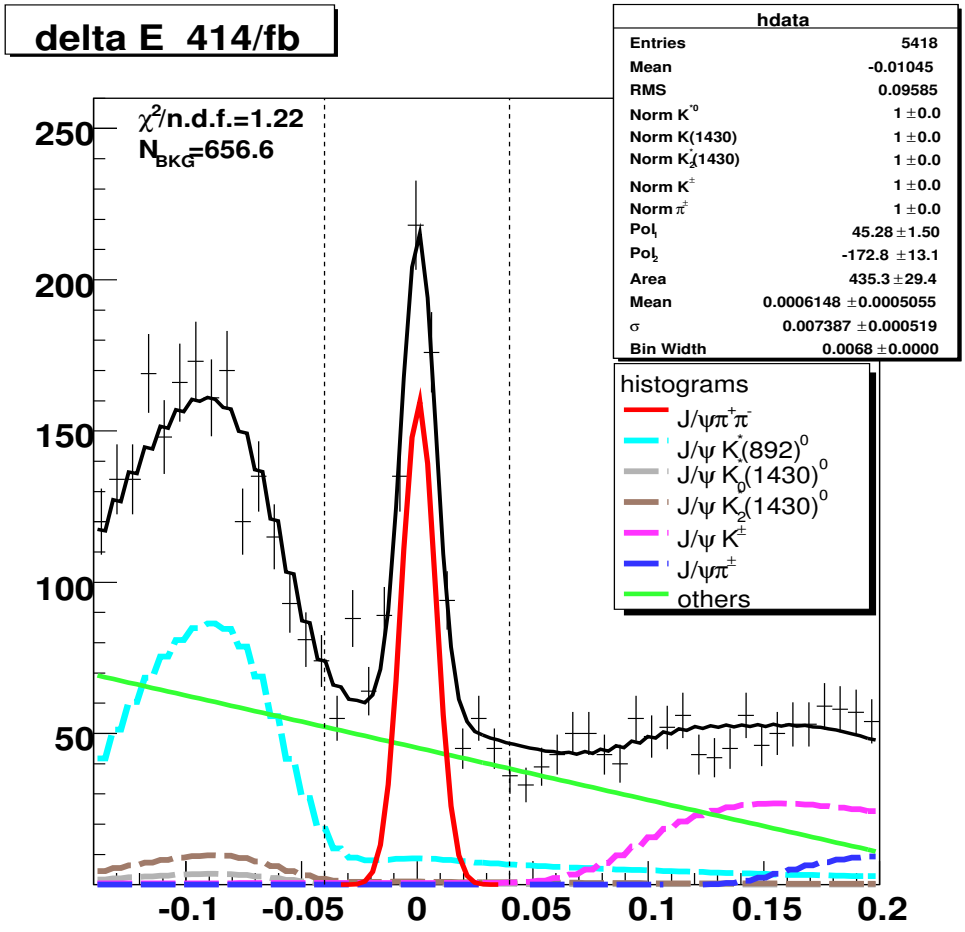

Figure 4.1: ΔE distribution with the fit result. Gaussian to describe $B^0 \to J/\psi\pi^+\pi^-$ signal + $B^0 \to J/\psi K^0_S(\to \pi^+\pi^-)$ and first order polynomial to describe the"Others" background, while background contributions due to exclusive B decay modes into J/ψ are fixed(see text). Here, first order polynomial takes not only $B\overline{B}$ background but also the potential continuum background into account.

	Mass (GeV/c^2)	Width (GeV/c^2)	Yield ratio
Gaussian 1	0.4977	0.002171	0.7618
Gaussian 2	0.4956	0.005002	0.2382

Table 4.1: Mass, width and the ratio of fitted yield to fit the $M_{\pi^+\pi^-}$ distribution of $B^0 \to J/\psi K^0_S$.

(see Figure 4.3), and obtained 101±10 events of $B^0 \to J/\psi K^0_S(\to \pi^+\pi^-)$ decays.

After subtracting this contribution, the net $B^0 \to J/\psi\pi^+\pi^-$ signal yield is obtained to be 334±40 events.

	Number of events
Number of gross $B^0 \to J/\psi\pi^+\pi^-$	435 ± 29
Number of $B^0 \to J/\psi K^0_S$	101 ± 10
Number of net signal $B^0 \to J/\psi\pi^+\pi^-$	334 ± 40

Table 4.2: The numbers to calculate the signal $B^0 \to J/\psi\pi^+\pi^-$ events.

The same procedure is applied to the subsamples which are divided according to $M_{\pi^+\pi^-}$ subregions to obtain the background contribution as a function of $M_{\pi^+\pi^-}$ (section 4.3.4).

In the next section, we describe the fit to the pion pair invariant mass spectrum in order to resolve the contributions of decays in $B^0 \to J/\psi\pi^+\pi^-$ final state.

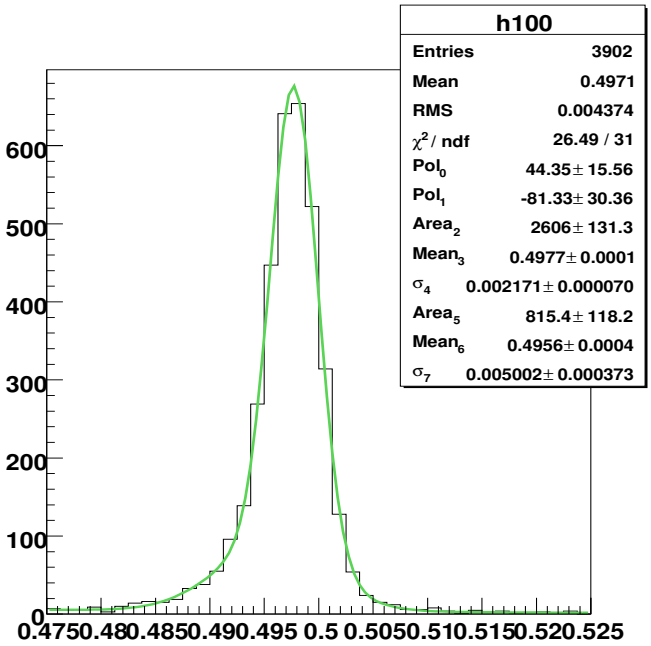

Figure 4.2: $M_{\pi^+\pi^-}$ distribution around K^0_S peak using signal Monte Carlo. Double Gaussian is capable to describe the peak shape.

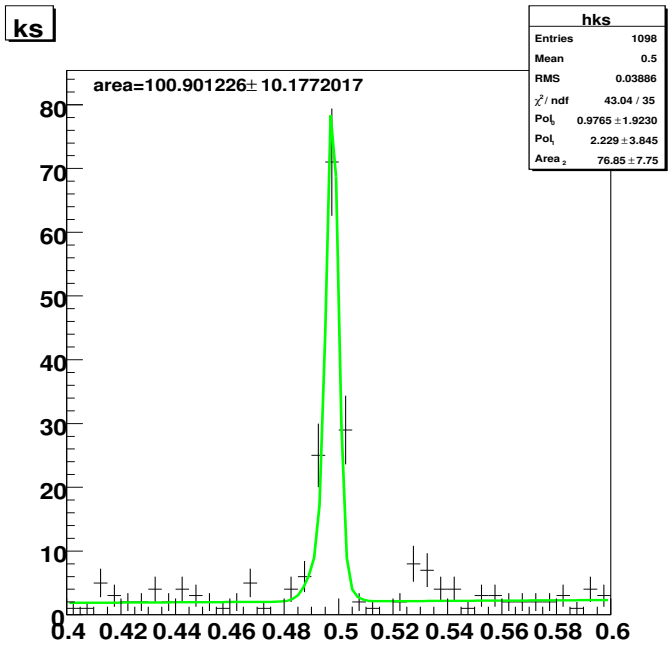

Figure 4.3: Fit to $M_{\pi^+\pi^-}$ distribution around $K^0_S \to \pi^+\pi^-$ peak of the events passing the selection criteria in 449 million $B\overline{B}$ experimental data. 101±10 $B^0 \to J/\psi K^0_S(\to \pi^+\pi^-)$ events are found.

4.2 Pion pair invariant mass ($M_{\pi^+\pi^-}$) spectrum

Figure 4.4 shows the distribution of the charged pion pairs' invariant mass($M_{\pi^+\pi^-}$) for the $B^0 \to J/\psi\pi^+\pi^-$ candidate events found in the signal region(5.27 GeV/c^2< $M_{\rm bc}$ < 5.29 GeV/c^2 and -0.04 GeV < ΔE < 0.04 GeV). The sharp peak at 0.5 GeV/c^2 due to $K^0_S \to \pi^+\pi^-$ and ρ^0 contribution around 0.77GeV/c^2 are apparent. There is an bump-like structure around $M_{\pi^+\pi^-} = 1.25$GeV/c^2, that might be the $B^0 \to J/\psi f_2$ contribution.

We take the following five contributions into account to describe the observed $M_{\pi^+\pi^-}$ distribution and perform a binned maximum likelihood fit to determine each contribution.

1. $B^0 \to J/\psi\rho^0$
2. $B^0 \to J/\psi f_2$
3. non-resonant $B^0 \to J/\psi\pi^+\pi^-$
4. $B^0 \to J/\psi K^0_S$
5. Background (not $B^0 \to J/\psi\pi^+\pi^-$)

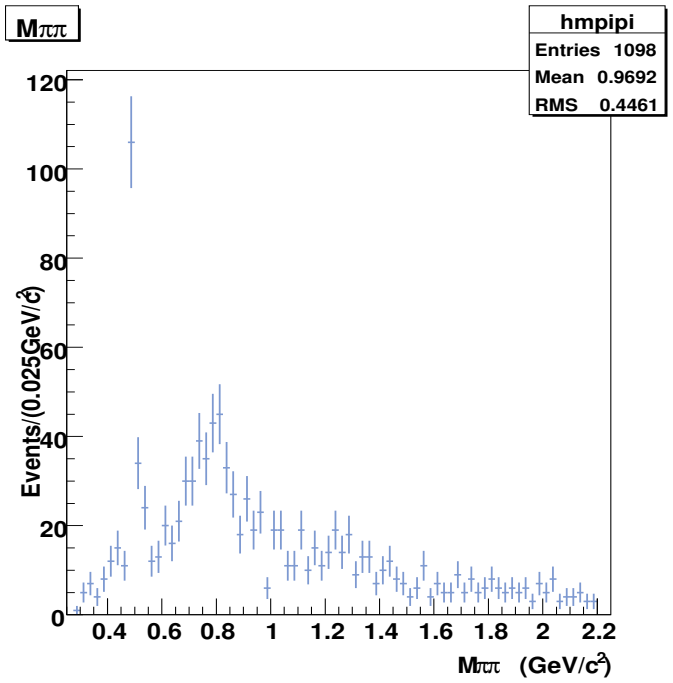

Figure 4.4: The pion pairs' invariant mass($M_{\pi^+\pi^-}$) distribution for the $B^0 \to J/\psi\pi^+\pi^-$ candidate events found from experimental data corresponding to 449 million $B\overline{B}$.

A probability density function (PDF) is constructed for each of these five contributions. Note that the $B^0 \to J/\psi K^0_S$ mode is not considered as signal. The detailed procedure is described in the following subsections.

4.3 Probability Density Functions to fit the $M_{\pi^+\pi^-}$ distribution

4.3.1 $B^0 \to J/\psi\rho^0$ and $B^0 \to J/\psi f_2$

In order to handle a resonance which comes from B decays, a relativistic Breit-Wigner function[48] is used. The Probability Density Function(PDF) is written as;

$$F(M_{\pi^+\pi^-}) = \frac{M_{\pi^+\pi^-}\Gamma(M_{\pi^+\pi^-})P^{2L_{eff}+1}}{(M_0^2 - M^2_{\pi^+\pi^-})^2 + M_0^2\Gamma(M_{\pi^+\pi^-})^2}, \tag{4.1}$$

where M_0, Γ_0 and J is mass, natural width and spin of the resonance, respectively. Here $M_{\pi^+\pi^-}$ dependent width $\Gamma(M_{\pi^+\pi^-})$ is introduced in order to take the final state's phase space into account,

$$\Gamma(M_{\pi^+\pi^-}) = \Gamma_0 \left(\frac{q}{q_0}\right)^{2J+1} \left(\frac{M_0}{M_{\pi^+\pi^-}}\right) G(R, q, q_0), \tag{4.2}$$

here $G(R, q, q_0)$ is the Blatt-Weiskopf barrier factor given in Table 4.3;

Spin J	Blatt-Weiskopf barrier factor $G(R, q, q_0)$
0	1
1	$\frac{1+(R/\hbar c)^2 {q_0}^2}{1+(R+\hbar c)^2 q^2}$
2	$\frac{9+3(R/\hbar c)^2 {q_0}^2+(R/\hbar c)^4 {q_0}^4}{9+3(R+\hbar c)^2 q^2+(R+\hbar c)^4 q^4}$

Table 4.3: Blatt-Weisskopf barrier factor for each spin state.

The meanings of the other parameters in PDF are as follows:

- q is the pion momentum in the di-pion rest frame;

$$q = \sqrt{\left(\frac{M_{\pi^+\pi^-}}{2}\right)^2 - m_\pi^2}, \tag{4.3}$$

  where m_π is the mass of charged pion.

- q_0 is the pion momentum for $M_{\pi^+\pi^-} = M_0$ case.

$$q_0 = \sqrt{\left(\frac{M_0}{2}\right)^2 - m_\pi^2} \tag{4.4}$$

$$\tag{4.5}$$

- P is the J/ψ momentum in the B^0 rest frame expressed as follows;

$$P = \sqrt{\frac{M_{B^0}^2 + M_{J/\psi}^2 - M_{\pi^+\pi^-}^2}{2M_{B^0}} - M_{J/\psi}^2}, \tag{4.6}$$

  where M_{B^0} and $M_{J/\psi}$ are masses of B and J/ψ, respectively.

- L_{eff} is the effective orbital angular momentum between the J/ψ and the ρ^0 or f_2, which can take any value in the range from 0 up to 2 (from 1 up to 3 in f_2 case). Here we use 1 in this analysis to extract the central value of signal yield. The difference in other fitting results are taken into account as a systematic uncertainty.

- R is the Blatt-Weiscopf barrier-factor radius[49]. The fit is performed in case of R equal to two values (0.5 and 1.0 fm[50]), and we used 1.0 fm in the nominal fit. The difference in other fitting result is taken into account as a systematic uncertainty.

The function $F(M_{\pi^+\pi^-})$ is a result from squared absolute value of the Breit-Wigner amplitude, $\mathcal{M}(M_{\pi^+\pi^-})$. Since the normalization of $F(M_{\pi^+\pi^-})$ is not easy to be analytically obtained, a normalization factor N is needed to be introduced. This N is to be adjusted in accordance with the numerical integration of $F(M_{\pi^+\pi^-})$. Hence, the amplitude $\mathcal{M}(M_{\pi^+\pi^-})$ can be written as:

$$\mathcal{M}(M_{\pi^+\pi^-}) = \frac{\sqrt{NM_{\pi^+\pi^-}\Gamma(M_{\pi^+\pi^-})P^{2L_{eff}+1}}}{(M^2_{\pi^+\pi^-} - M_0^2) + iM_0\Gamma(M_{\pi^+\pi^-})}. \tag{4.7}$$

Therefore, its real and imaginary parts are:

$$Re(\mathcal{M}) = \sqrt{NM_{\pi^+\pi^-}\Gamma(M_{\pi^+\pi^-})P^{2L_{eff}+1}}\frac{M^2_{\pi^+\pi^-} - M_0^2}{(M^2_{\pi^+\pi^-} - M_0^2) + M_0^2\Gamma(M^2_{\pi^+\pi^-})}, \tag{4.8}$$

$$Im(\mathcal{M}) = \sqrt{NM_{\pi^+\pi^-}\Gamma(M_{\pi^+\pi^-})P^{2L_{eff}+1}}\frac{-M_0\Gamma(M_{\pi^+\pi^-})}{(M^2_{\pi^+\pi^-} - M_0^2) + M_0^2\Gamma(M^2_{\pi^+\pi^-})}. \tag{4.9}$$

Then overall phase θ is applied to this amplitude, i.e.

$$\mathcal{M} \to \mathcal{M}e^{i\theta}. \tag{4.10}$$

So real and imaginary parts are modified to be:

$$Re(\mathcal{M}) = \frac{\sqrt{NM_{\pi^+\pi^-}\Gamma(M_{\pi^+\pi^-})P^{2L_{eff}+1}}}{(M^2_{\pi^+\pi^-} - M_0^2)^2 + M_0^2\Gamma(M_{\pi^+\pi^-})^2}\{(M^2_{\pi^+\pi^-} - M_0^2)\cos\theta + M_0\Gamma(M_{\pi^+\pi^-})\sin\theta\}, \tag{4.11}$$

$$Im(\mathcal{M}) = \frac{\sqrt{NM_{\pi^+\pi^-}\Gamma(M_{\pi^+\pi^-})P^{2L_{eff}+1}}}{(M^2_{\pi^+\pi^-} - M_0^2)^2 + M_0^2\Gamma(M_{\pi^+\pi^-})^2}\{(M^2_{\pi^+\pi^-} - M_0^2)\sin\theta - M_0\Gamma(M_{\pi^+\pi^-})\cos\theta\}. \tag{4.12}$$

If there is only one resonance contributes to the decay, such overall phase does not have any physical meaning, since overall phase does not give us any change of the observed quantities. However, when we consider the case that two different resonances contribute, the phase has an important meaning. Their amplitudes are $\mathcal{M}_1$ and $\mathcal{M}_2$, both are expressed as Equation 4.7. In general, there is a phase difference between these two resonances. Therefore in order to take this fact into account,

$$\mathcal{M}_2 \to \mathcal{M}_2 e^{i\theta} \tag{4.13}$$

has to be done, where θ becomes the phase difference the two resonances. Finally, the function to be used to fit real $M_{\pi^+\pi^-}$ is obtained to be:

$$|\mathcal{M}_1 + \mathcal{M}_2 e^{i\theta}|^2. \tag{4.14}$$

Test of PDF for $B^0 \to J/\psi\rho^0$ with signal Monte Carlo

The PDF used to model the ρ^0 resonance is a relativistic p-wave Breit-Wigner function with the parameters listed in Table 4.4. The fitting result for signal Monte Carlo events is shown in Figure 4.5. The phase is fixed to 0, because this fitting considers a single resonance.

Parameter	value
J	1
Γ_0	146.4 MeV/c^2
M_0	775.5 MeV/c^2
phase	0

Table 4.4: The parameter values in the Breit-Wigner function for $B^0 \to J/\psi\rho^0$

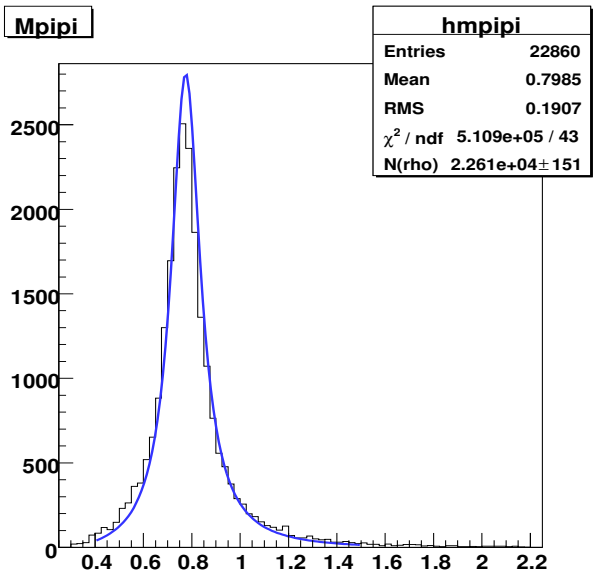

Figure 4.5: Fit to $M_{\pi^+\pi^-}$ distribution of $B^0 \to J/\psi\rho^0$ signal Monte Carlo with p-wave Breit Wigner function.

Test of PDF for $B^0 \to J/\psi f_2$ with signal Monte Carlo

The PDF used to model the f_2 resonance is a relativistic d-wave Breit-Wigner function with the parameters listed in Table 4.5. The fitting result for signal Monte Carlo events is shown in the Figure 4.6. The phase is fixed to 0, because this fitting considers a single resonance.

Parameter	value
J	2
Γ_0	185.1 MeV/c^2
M_0	1275.4 MeV/c^2
phase	0

Table 4.5: The parameter values in the Breit-Wigner function for $B^0 \to J/\psi f_2$

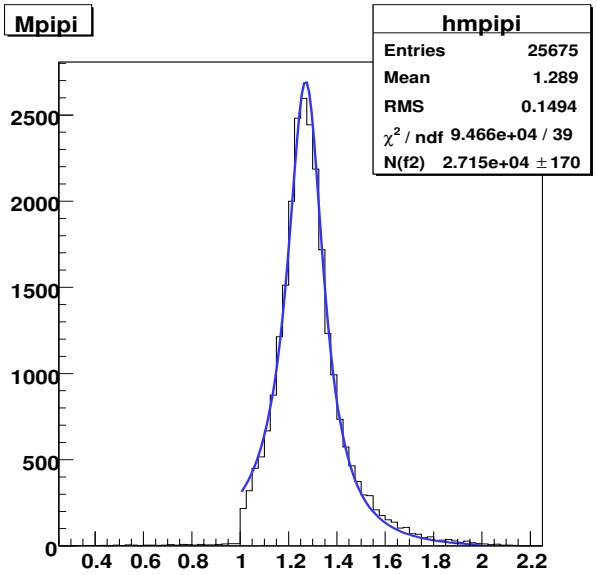

Figure 4.6: Fit to $M_{\pi^+\pi^-}$ distribution of $B^0 \to J/\psi f_2$ signal Monte Carlo with d-wave Breit Wigner function.

4.3.2 Non-resonant $B^0 \to J/\psi\pi^+\pi^-$

We assume that the $M_{\pi^+\pi^-}$ distribution for non-resonant $B^0 \to J/\psi\pi^+\pi^-$ is same as $B^0 \to J/\psi\pi^+\pi^-$ PHSP decays. Therefore based on $B^0 \to J/\psi\pi^+\pi^-$ PHSP Monte Carlo sample, an empirical function to describe the $M_{\pi^+\pi^-}$ distribution is obtained as shown in Figure 4.7 by comparing the results for several orders of polynomials (see Figure 4.8), we use a sixth order polynomial function as a PDF used to model the non-resonant $B^0 \to J/\psi\pi^+\pi^-$ mode. The obtained formula $F_{\rm NR}(M_{\pi^+\pi^-})$ is

$$F_{\rm NR}(M_{\pi^+\pi^-}) = n(-6170 + 44400M_{\pi^+\pi^-} - 113000M^2_{\pi^+\pi^-} + 150000M^3_{\pi^+\pi^-} \\ -105000M^4_{\pi^+\pi^-} + 37100M^5_{\pi^+\pi^-} - 5232M^6_{\pi^+\pi^-}) \quad (4.15)$$

,where n is the normalization factor that is treated as a floated parameter in the fitting to $M_{\pi^+\pi^-}$.

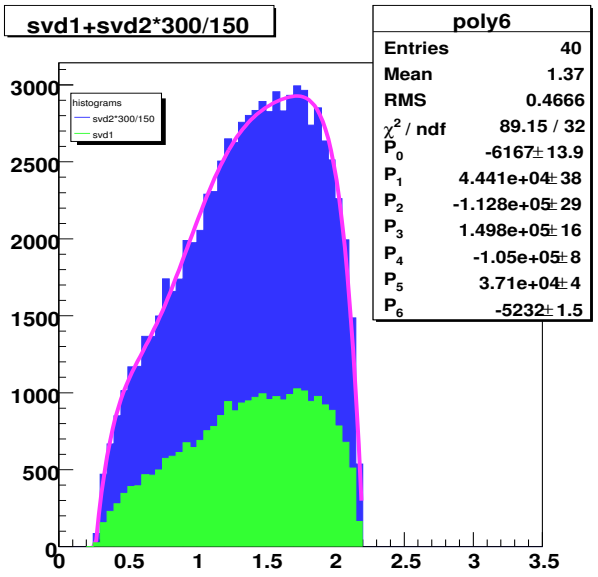

Figure 4.7: $M_{\pi^+\pi^-}$ distribution obtained from $B^0 \to J/\psi\pi^+\pi^-$ PHSP Monte Carlo. The parametrized curve is 6th order polynomial used to model the non-resonant $J/\psi\pi^+\pi^-$ contribution. Different hatchings are corresponding to SVD1 and SVD2 Monte Carlo. The ratio between SVD1 and SVD2 Monte Carlo sample is determined by the number of $B\overline{B}$ in experimental data.

4.3.3 $B^0 \to J/\psi K^0_S$

As described in section 4.1.1, $K^0_S \to \pi^+\pi^-$ contribution is described by double Gaussian function. The mass and width values of each Gaussian function and the ratio of their fitted yield are fixed with the results listed in Table 4.1.

4.3.4 Background (non $B^0 \to J/\psi\pi^+\pi^-$)

As explained in section 3.5.1, ΔE distribution is appropriate to obtain the background yield as well as the signal. Therefore, in order to obtain the background distribution as a function of $M_{\pi^+\pi^-}$, we divide the candidate event sample according to $M_{\pi^+\pi^-}$ in every 0.1 GeV/c^2 bin from 0.25 GeV/c^2 to 2.25 GeV/c^2. Then the fitting to the ΔE distribution in each $M_{\pi^+\pi^-}$ bin is performed with the same way used in section 4.1.1. Figure 4.9 $\sim$ Figure 4.27 show the results of the $M_{\pi^+\pi^-}$ bin-by-bin fits. The signal width value is fixed to 7.327 MeV/c^2 according to the signal Monte Carlo expectation.

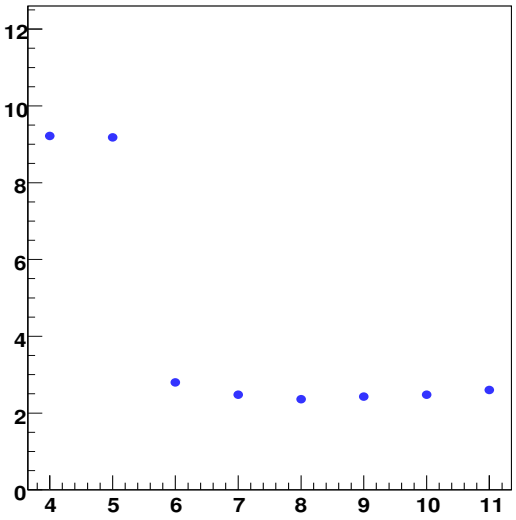

Figure 4.8: The reduced χ^2 ($= \chi^2$ divided by the number of degree of freedom of the fit) values are plotted as a function of the orders of the polynomial functions which were used for the fitting to the $M_{\pi^+\pi^-}$ distribution of non-resonant $B^0 \to J/\psi\pi^+\pi^-$. The 6th order of polynomial was adopted as the proper function.

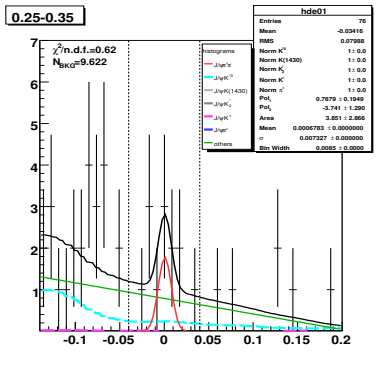

Figure 4.9: ΔE within $M_{\rm bc}$ signal region. ($0.25< M_{\pi\pi} <0.35{\rm GeV}/c^2$) †

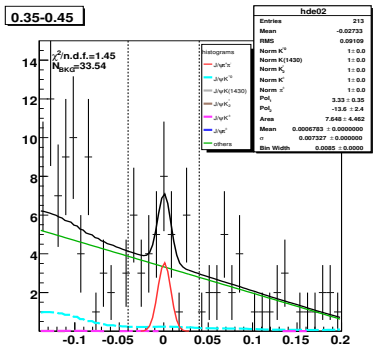

Figure 4.10: ΔE within $M_{\rm bc}$ signal region. ($0.35< M_{\pi\pi} <0.45{\rm GeV}/c^2$)

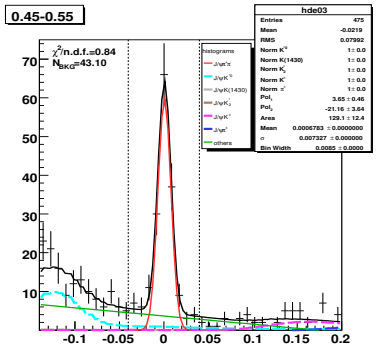

Figure 4.11: ΔE within $M_{\rm bc}$ signal region. ($0.45< M_{\pi\pi} <0.55{\rm GeV}/c^2$)

†For Figure 4.9 ∼ Figure 4.28, the dots with error bars show distribution of experimental data. The red line is Gaussian to describe signal. The dashed lines are smoothed histograms of Monte Carlo to describe background distributions listed in Table 3.4. The green line is first order polynomial to describe other backgrounds. The fitting procedure is same as described in subsection 4.1.1.

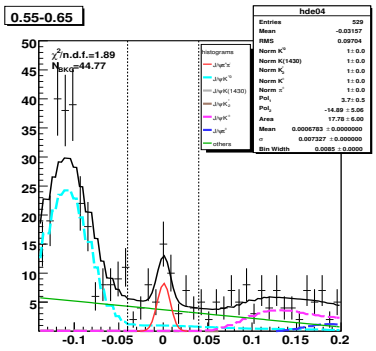

Figure 4.12: ΔE within $M_{\rm bc}$ signal region.
(0.55< $M_{\pi\pi}$ <0.65GeV/c^2)

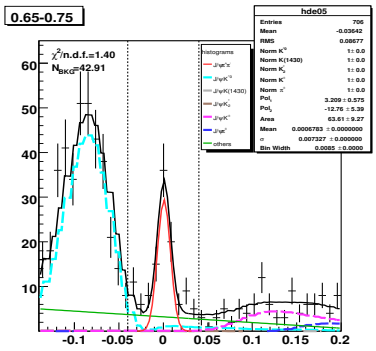

Figure 4.13: ΔE within $M_{\rm bc}$ signal region.
(0.65< $M_{\pi\pi}$ <0.75GeV/c^2)

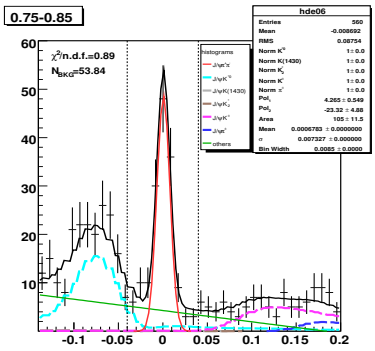

Figure 4.14: ΔE within $M_{\rm bc}$ signal region.
(0.75< $M_{\pi\pi}$ <0.85GeV/c^2)

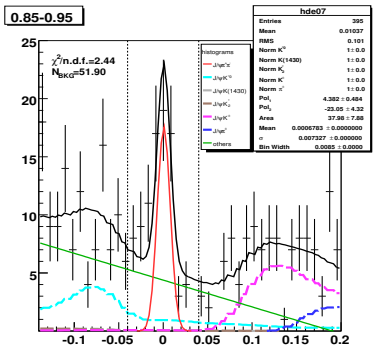

Figure 4.15: ΔE within $M_{\rm bc}$ signal region.
(0.85< $M_{\pi\pi}$ <0.95GeV/c^2)

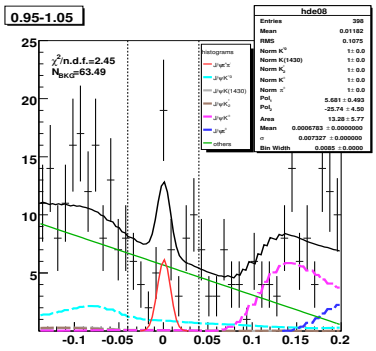

Figure 4.16: ΔE within $M_{\rm bc}$ signal region.
(1.05< $M_{\pi\pi}$ <1.15GeV/c^2)

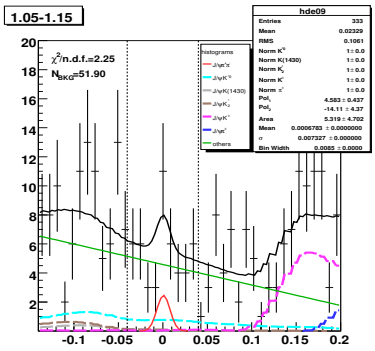

Figure 4.17: ΔE within $M_{\rm bc}$ signal region.
(1.05< $M_{\pi\pi}$ <1.15GeV/c^2)

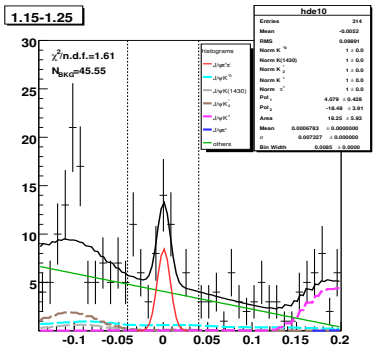

Figure 4.18: ΔE within $M_{\rm bc}$ signal region.
(1.15< $M_{\pi\pi}$ <1.25GeV/c^2)

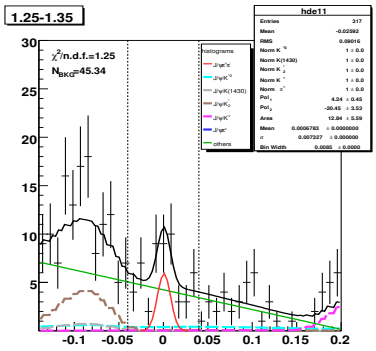

Figure 4.19: ΔE within $M_{\rm bc}$ signal region.
(1.25< $M_{\pi\pi}$ <1.35GeV/c^2)

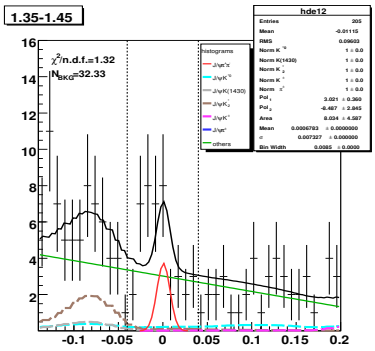

Figure 4.20: ΔE within $M_{\rm bc}$ signal region.
(1.35< $M_{\pi\pi}$ <1.45GeV/c^2)

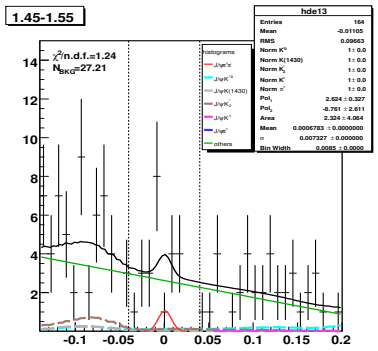

Figure 4.21: ΔE within $M_{\rm bc}$ signal region. ($1.45< M_{\pi\pi} <1.55 {\rm GeV}/c^2$)

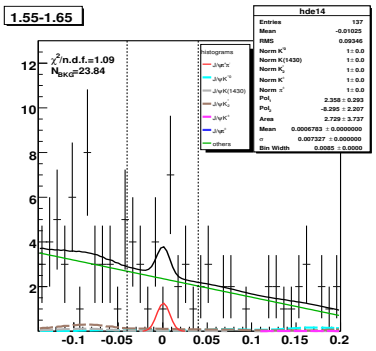

Figure 4.22: ΔE within $M_{\rm bc}$ signal region. ($1.55< M_{\pi\pi} <1.65 {\rm GeV}/c^2$)

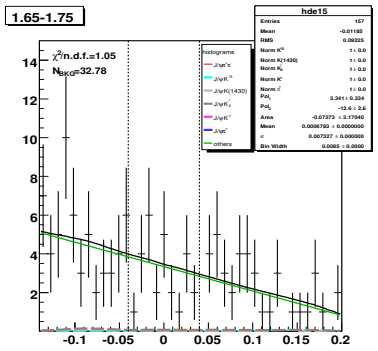

Figure 4.23: ΔE within $M_{\rm bc}$ signal region. ($1.65< M_{\pi\pi} <1.75 {\rm GeV}/c^2$)

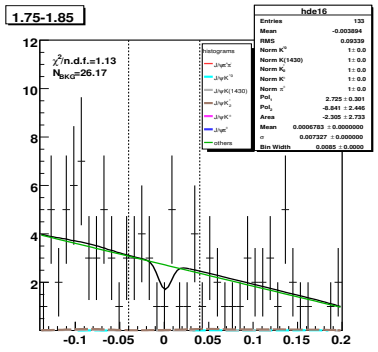

Figure 4.24: ΔE within $M_{\rm bc}$ signal region. ($1.75< M_{\pi\pi} <1.85 {\rm GeV}/c^2$)

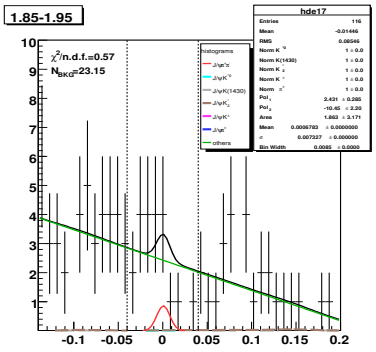

Figure 4.25: ΔE within $M_{\rm bc}$ signal region. ($1.85< M_{\pi\pi} <1.95 {\rm GeV}/c^2$)

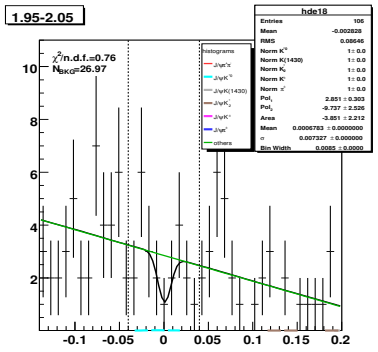

Figure 4.26: ΔE within $M_{\rm bc}$ signal region. ($1.95< M_{\pi\pi} <2.05 {\rm GeV}/c^2$)

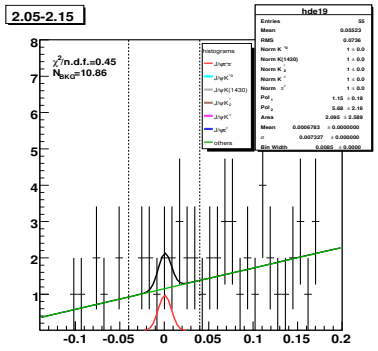

Figure 4.27: ΔE within $M_{\rm bc}$ signal region. ($2.05< M_{\pi\pi} <2.15 {\rm GeV}/c^2$)

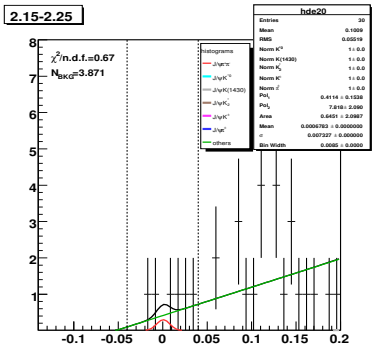

Figure 4.28: ΔE within $M_{\rm bc}$ signal region. ($2.15< M_{\pi\pi} <2.25 {\rm GeV}/c^2$)

We performed the fits to the obtained background as a function of $M_{\pi^+\pi^-}$ with several

order of polynomials (see Figure 4.30) then obtained the proper function shown in Figure 4.29. The resultant background PDF formula $F_{\mathrm{B.G.}}(M_{\pi^+\pi^-})$ is

$$F_{\mathrm{B.G.}}(M_{\pi^+\pi^-}) = -99 + 528M_{\pi^+\pi^-} - 631M^2_{\pi^+\pi^-} + 307M^3_{\pi^+\pi^-} - 54M^4_{\pi^+\pi^-}. \quad (4.16)$$

Because this PDF is determined model-independently by data, this does not have any free parameters (i.e. normalization factor is 1).

Here, the signal yields are obtained as a function of $M_{\pi^+\pi^-}$ at the same time. Since the bin width is coarse (0.1 GeV/c^2), those signal yield values are used to perform a cross check of the nominal fit to resolve ρ^0, f_2 and non-resonant contributions as shown in section 4.6.

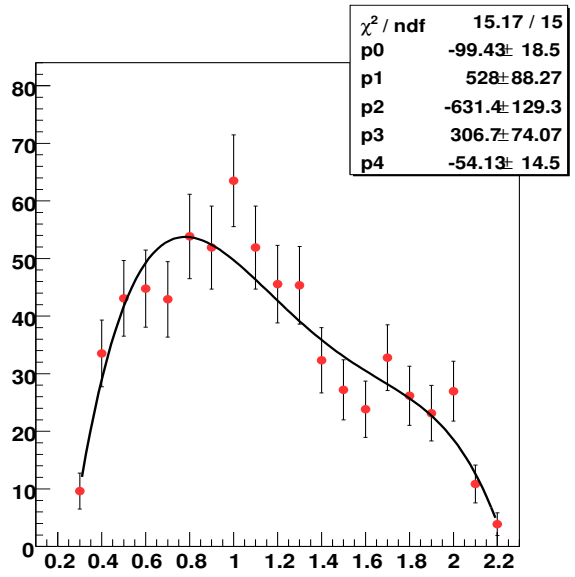

Figure 4.29: Background PDF as a function of $M_{\pi^+\pi^-}$, expressed as a 4th order polynomial. The amount of the background is extracted from the fit to ΔE distribution of the subsample divided by 0.1 GeV/c^2-wide $M_{\pi^+\pi^-}$ bins.

4.4 Detection efficiency correction

In principle, the detection efficiency can have a dependence on $M_{\pi^+\pi^-}$. If it is the case, this effect has to be taken into account during the fit to $M_{\pi^+\pi^-}$ distribution. Using the $B^0 \to J/\psi\pi^+\pi^-$ PHSP, $B^0 \to J/\psi\rho^0$ and $B^0 \to J/\psi f_2$ signal Monte Carlo events mentioned in section 3.2.1, we investigated the behavior of detection efficiencies for each

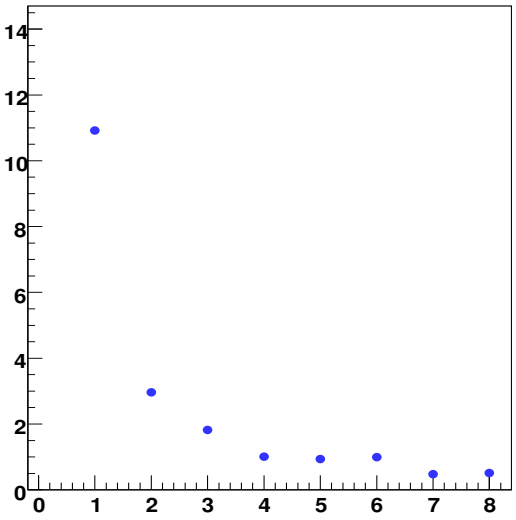

Figure 4.30: The reduced χ^2 ($= \chi^2$ divided by the number of degree of freedom of the fit) values are plotted as a function of the orders of the polynomial functions which were used for the fitting to the background distribution. The 4th order of polynomial was adopted as the proper function.

subsample divided by proper $M_{\pi^+\pi^-}$ bins. The detection efficiency (ϵ_i) for i-th bin is defined as

$$\epsilon_i = \frac{N_i^{det}}{N_i^{gen}}, \tag{4.17}$$

where N_i^{det} is the signal yield obtained by the fit to ΔE distribution and N_i^{gen} is the number of generated events in i-th $M_{\pi^+\pi^-}$ bin.

As shown in Figure 4.31, detection efficiencies exhibit consistent behavior between SVD1 and SVD2 environment. The numerical results are summarized in Table 4.6, where the ratio of the efficiency difference is defined as

$$R_{diff} = \frac{\epsilon_{SVD1} - \epsilon_{SVD2}}{\epsilon_{SVD2}}. \tag{4.18}$$

For these three processes of $B^0 \to J/\psi\pi^+\pi^-$ PHSP, $B^0 \to J/\psi\rho^0$ and $B^0 \to J/\psi f_2$, the ratio of the difference is defined as

$$R'_{diff} = \frac{\epsilon_{J/\psi\rho^0 \text{ or } J/\psi f_2} - \epsilon_{\texttt{PHSP}}}{\epsilon_{\texttt{PHSP}}}. \tag{4.19}$$

The detection efficiencies are found to be also consistent each other with considering the error of the efficiency in each $M_{\pi^+\pi^-}$ bin. Therefore we use the efficiency curve obtained by $B^0 \to J/\psi\pi^+\pi^-$ PHSP signal Monte Carlo as an universal one to perform acceptance

	$B^0 \to J/\psi\pi^+\pi^-$ PHSP	$B^0 \to J/\psi\rho^0$	$B^0 \to J/\psi f_2$
ϵ_{SVD1}	0.280 ± 0.005	0.247 ± 0.005	0.273 ± 0.005
ϵ_{SVD2}	0.279 ± 0.005	0.242 ± 0.005	0.272 ± 0.005
R_{diff}	0.5%	2.0%	0.4%

Table 4.6: The efficiency of $B^0 \to J/\psi\pi^+\pi^-$ PHSP, $B^0 \to J/\psi\rho^0$ and $B^0 \to J/\psi f_2$ modes for SVD1 and SVD2. The ratios of the differences between SVD1 and SVD2 are shown in the bottom.

	$B^0 \to J/\psi\pi^+\pi^-$ PHSP and $B^0 \to J/\psi\rho^0$	$B^0 \to J/\psi\pi^+\pi^-$ PHSP and $B^0 \to J/\psi f_2$
R'_{diff}	6.0%	1.5%

Table 4.7: The ratio of the efficiency difference among three modes.

correction for all three considered processes. This efficiency curve is parameterized with 6th order polynomial then considered in $M_{\pi^+\pi^-}$ fittings mentioned in section 4.5. For the calculation of total $B^0 \to J/\psi\pi^+\pi^-$, ϵ =0.281 $\pm$ 0.005 is used which is the weighted average value of $B^0 \to J/\psi\rho^0$ and $B^0 \to J/\psi f_2$ modes.

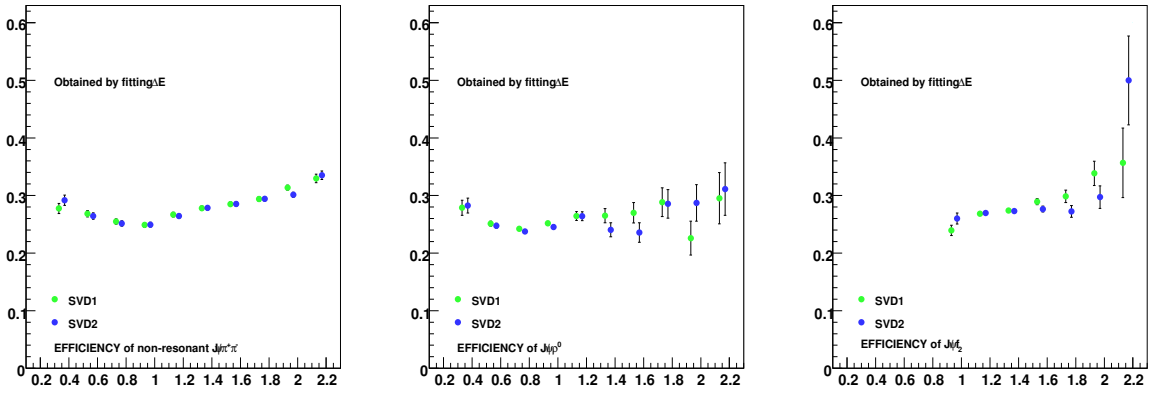

Figure 4.31: The efficiency curve as a function of $M_{\pi^+\pi^-}$ obtained by
Left; $B^0 \to J/\psi\pi^+\pi^-$ PHSP signal Monte Carlo, Center; $B^0 \to J/\psi\rho^0$ signal Monte Carlo, Right; $B^0 \to J/\psi f_2$ signal Monte Carlo.
$B^0 \to J/\psi\pi^+\pi^-$ PHSP is used as an universal one to obtain an efficiency correction function.

4.5 $M_{\pi^+\pi^-}$ fitting results

A binned maximum likelihood fit is performed with PDFs described in section 4.3. Here, in order to examine the existence of the $B^0 \to J/\psi f_2$ and the non-resonant $B^0 \to J/\psi\pi^+\pi^-$ decays, the fit is carried out in three different cases;

(i) $B^0 \to J/\psi\rho^0$, $B^0 \to J/\psi K^0_S$ and Background,

(ii) $B^0 \to J/\psi f_2$ contribution is additionally taken into account,

(iii) non-resonant $B^0 \to J/\psi\pi^+\pi^-$ contribution is additionally taken into account to case (ii).

(i) is shown in Figure 4.32. This includes only well-known decay modes. (ii) and (iii) are shown in Figure 4.33 and 4.34, respectively. The interference between $B^0 \to J/\psi\rho^0$ and $B^0 \to J/\psi f_2$ is taken into account in those fits.

The results are summarized in Table 4.8. The calculation of the branching fractions are done by using the results of (iii) Figure 4.34 in section 4.8.1, because it's likelihood of the fit is the best value.

	(i) Figure 4.32	(ii) Figure 4.33	(iii) Figure 4.34
N($B^0 \to J/\psi\rho^0$)	1098 ± 93	997 ± 99	991 ± 99
N($B^0 \to J/\psi f_2$)	———	74 ± 44	60 ± 45
$N_{NR}(B^0 \to J/\psi\pi^+\pi^-)$	———	———	73 ± 92
phase difference (rad)	———	1.08 ± 0.66	1.09 ± 0.77
-2lnL	246.6	239.6	238.9

Table 4.8: Summary of fitting results. Note that N($B^0 \to J/\psi\rho^0$), N($B^0 \to J/\psi f_2$) and $N_{NR}(B^0 \to J/\psi\pi^+\pi^-)$ are efficiency corrected values.

4.6 Cross Check

As mentioned in section 4.3.4, the signal yield extracted as a function of $M_{\pi^+\pi^-}$ provides a good cross check. It is performed as shown in Figure 4.35 and 4.36 for (ii) and (iii) cases. The results are summarized in Table 4.9.

The yields of ρ^0 and f_2 as well as the phase difference between them are found to be consistent with the resultant values obtained by the fit results shown in previous section 4.5 within their statistical errors.

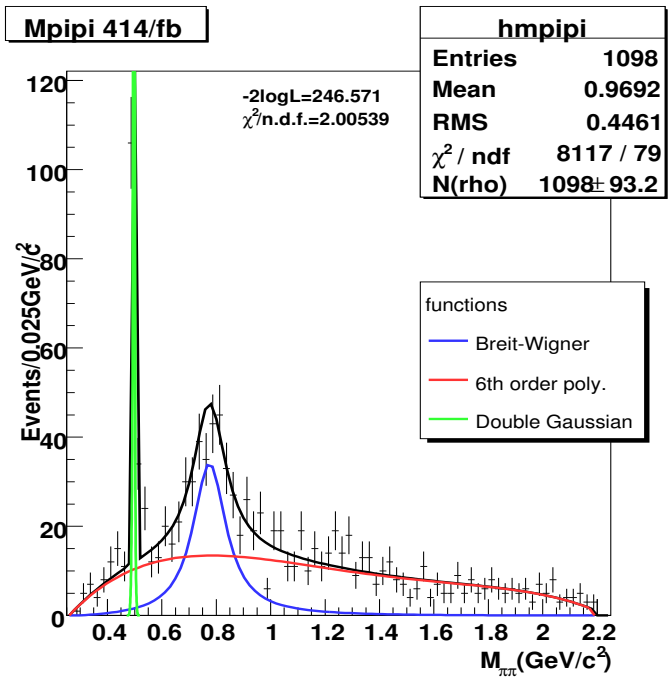

Figure 4.32: Fit to $M_{\pi^+\pi^-}$ distribution with $J/\psi\rho^0$ + $J/\psi K_S^0$ + Background.

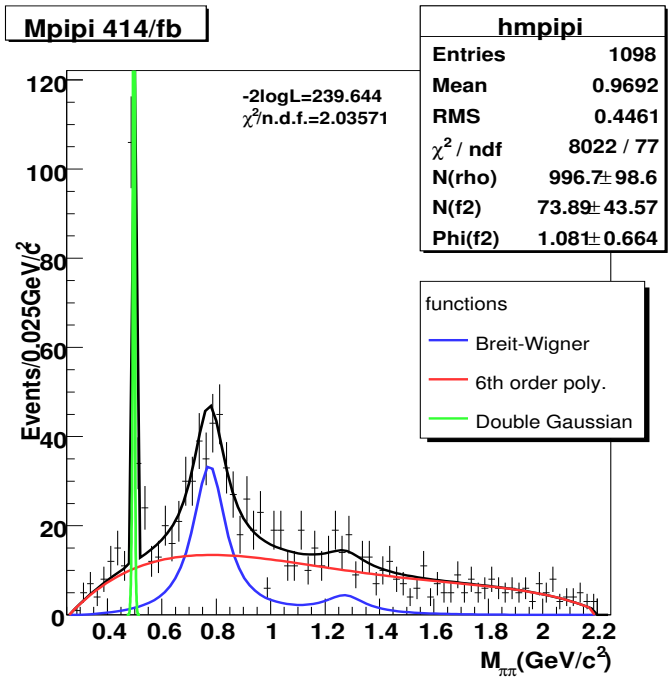

Figure 4.33: Fit to $M_{\pi^+\pi^-}$ distribution with $\underline{J/\psi f_2}$ + $J/\psi\rho^0$ + $J/\psi K_S^0$ + Background. The interference between $J/\psi\rho^0$ and $J/\psi f_2$ is taken into account.

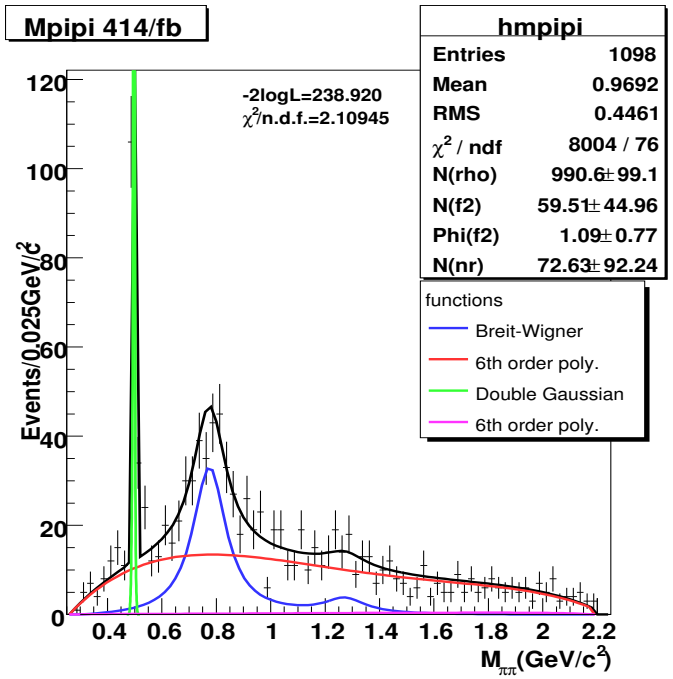

Figure 4.34: Fit to $M_{\pi^+\pi^-}$ distribution with $\underline{\text{non} - \text{resonant}\, J/\psi\pi^+\pi^-} + J/\psi f_2 + J/\psi\rho^0 + J/\psi K_S^0$ + Background. The interference between $J/\psi\rho^0$ and $J/\psi f_2$ is taken into account.

	(ii) Figure 4.33	(iii) Figure 4.34
$\mathrm{N}(B^0 \to J/\psi\rho^0)$	924 ± 82	927 ± 82
$\mathrm{N}(B^0 \to J/\psi f_2)$	76 ± 33	84 ± 36
$\mathrm{N}_{\mathrm{NR}}(B^0 \to J/\psi\pi^+\pi^-)$	———	-32 ± 58
phase difference (rad)	1.13 ± 0.48	1.12 ± 0.45

Table 4.9: Summary of fit results as a cross check. Note that $\mathrm{N}(B^0 \to J/\psi\rho^0)$, $\mathrm{N}(B^0 \to J/\psi f_2)$ and $\mathrm{N}_{\mathrm{NR}}(B^0 \to J/\psi\pi^+\pi^-)$ are efficiency corrected values.

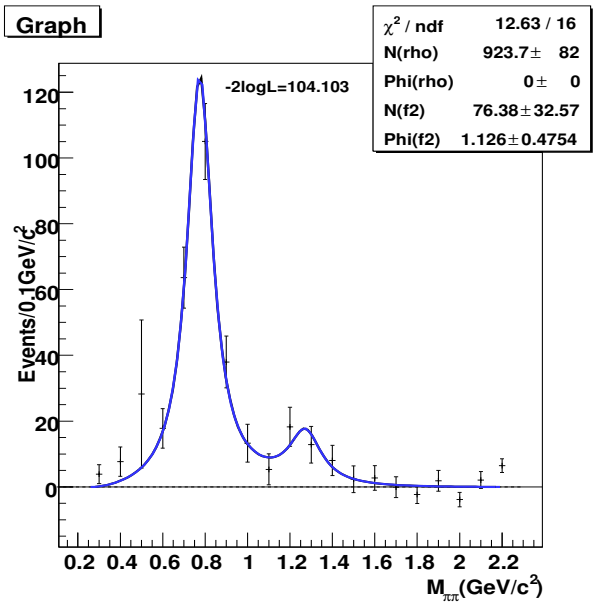

Figure 4.35: Fit to the signal yield extracted as a function of $M_{\pi^+\pi^-}$ with $f_2 + \rho^0$ contributions. The obtained values are found to be consistent with the resultant values obtained by the fit shown as Figure 4.33 within their statistical errors.

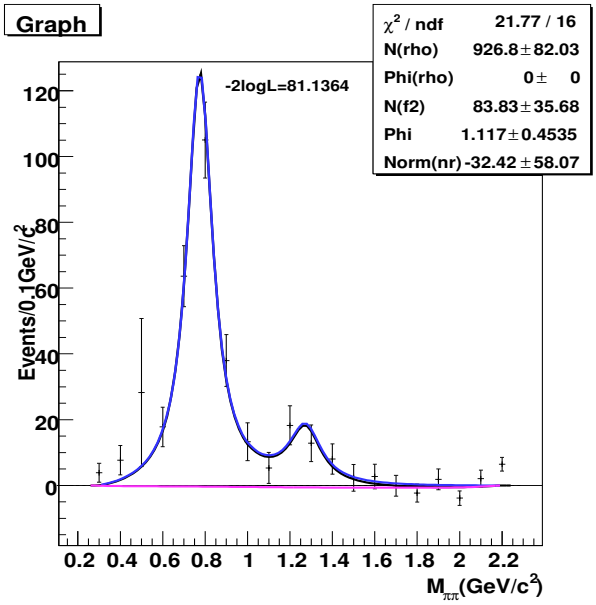

Figure 4.36: Fit to the signal yield extracted as a function of $M_{\pi^+\pi^-}$ with non-resonant $\pi^+\pi^- + f_2 + \rho^0$ contributions. The obtained values are found to be consistent with the resultant values obtained by the fit shown as Figure 4.34.

4.7 Systematic uncertainties

We consider the following sources for systematic errors. The considered systematic errors and their contribution to each decay mode are listed in Table 4.18 and 4.19. The total systematic uncertainty is calculated by a sum of them in quadrature.

4.7.1 Track reconstruction

It is estimated by the measurement of the data-Monte Carlo relative efficiency of charged tracks using $\eta \to \pi^+\pi^-\pi^0$ and $\eta \to \gamma\gamma$. The efficiency ratio between data and Monte Carlo is obtained by taking the ratio

$$\frac{\epsilon_{DATA}(\pi^+\pi^-)}{\epsilon_{MC}(\pi^+\pi^-)} = \frac{N_{DATA}(\eta \to \pi^+\pi^-\pi^0)/N_{DATA}(\eta \to \gamma\gamma)}{N_{MC}(\eta \to \pi^+\pi^-\pi^0)/N_{MC}(\eta \to \gamma\gamma)}, \tag{4.20}$$

where N is the signal yield for data and Monte Carlo of the relevant decay. The systematic error arising from the photon detection is assumed to be canceled out by taking the ratio, since the $\pi^\pm$ also decays into two photons. The tracking efficiency for a single track can be obtained from the ratio. The single $\pi^\pm$ finding efficiency ratio can be determined by

$$\frac{\epsilon^{single}_{DATA}}{\epsilon^{single}_{MC}} = \sqrt{\frac{\epsilon_{DATA}(\pi^+\pi^-)}{\epsilon_{MC}(\pi^+\pi^-)}}. \tag{4.21}$$

The statistical error for this method is very small thanks to the large amount of η mesons, so if the ratio, Equation 4.21, deviates from 1, it directly indicates probable systematic effect of charged particle detection.

The systematic uncertainty of finding one charged track is estimated to be 1.2 %. These errors have to be added linearly and to be rounded into proper digits. As a result, we have a 4.9 % systematic error arising from tracking efficiencies in the final state of $B^0 \to J/\psi\pi^+\pi^-$ decay.

4.7.2 Particle identification

- Lepton ID

  The systematic uncertainties related to lepton identification are estimated by the J/ψ decays into e^+e^- or $\mu^+\mu^-$ modes. In the case of $J/\psi \to e^+e^-$ mode, first of all, one charged track is required to be identified as electron (or positron) with very tight likelihood ratio criteria. Then two kinds of combinations are made; (i) combined with all the oppositely charged tracks and (ii) combined with the oppositely charged track that is identified as electron with the nominal likelihood ratio criteria. By the fit to the invariant mass distributions for the above two cases, the $J/\psi \to e^+e^-$

signal yields are extracted. The difference in the J/ψ yield between (i) and (ii) corresponds to the electron identification efficiency. This method is also applied to a large statistics $B\overline{B}$ MC sample. The ratio of electron identification efficiencies between the experimental data and MC is found to be 1.025 ± 0.011 for SVD1 and 1.023 ± 0.013 for SVD2 data. Being weighted by the corresponding number of $B\overline{B}$ pairs, the central value's deviation from unity and statistical errors are summed in quadrature. As a result, the uncertainty of electron identification is estimated to be 2.7 % per track. Since we require both tracks are identified as electron (or positron), the effect to the branching fraction is 5.4 %.

In the $J/\psi \to \mu^+\mu^-$ mode, a simpler procedure is applied. The two kinds of combinations; (iii) one track is identified as muon with the nominal likelihood ratio requirement and is combined with all the oppositely charged tracks (single tag) and (iv) both tracks are required to be identified as muon with the nominal criteria to reconstruct $B^0 \to J/\psi\pi^+\pi^-$ signal. This is because the QED process background is much less in the lepton pair's invariant mass distribution in $\mu^+\mu^-$ case, i.e. $e^+e^- \to \mu^+\mu^-$ or $\mu^+\mu^-\gamma$ processes have much smaller cross section than $e^+e^- \to e^+e^-$ or $e^+e^-\gamma$ processes. The muon identification efficiency is estimated by the fit to invariant mass distributions for (iii) and (iv), then probable difference between the experimental data and MC is regarded as the uncertainty of muon identification. The resultant value is 1.3 % and 1.1 % per track for SVD1 and SVD2, respectively. Again both tracks are required to be identified as muon, the effect to the branching fraction is estimated to be 2.4 % after weighted by the corresponding number of $B\overline{B}$ pairs.

By taking weighted average of these values according to J/ψ decay branching fraction, it is estimated to be 3.9 %.

- Pion ID

  The pion identification efficiency is studied in data and Monte Carlo using the decay

$$\begin{aligned} D^{*+} \to \; & D^0 \quad \pi_s^+ \\ & D^0 \quad \to K^-\pi^+, \end{aligned}$$

  and its conjugate decay

$$\begin{aligned} D^{*-} \to \; & \overline{D}^0 \quad \pi_s^- \\ & \overline{D}^0 \quad \to K^+\pi^-. \end{aligned}$$

  Due to the small mass difference between the D^{*+} and D^0 mesons, the pion from the $D^{*\pm}$ decay has a low momentum (less than 200 GeV/c) and is denoted by π_s.

The existence of π_s, the narrow width of the D meson and the small D^0-D^{*+} mass difference enables these decays to be reconstructed with a good signal to noise ratio without relying on the PID information. The K and π mesons in the D^0 decay can be identified, or tagged, by comparing their charge to that of the slow pion without any other information. This enables us to study the PID efficiencies in the data on particles that are known to be kaons or pions. Samples of tagged kaons and pions are obtained by reconstructing the D^* decays in data and Monte Carlo. The PID efficiency for pions, ϵ_π is defined as the number of events with a true pion remaining after the pion likelihood selection criteria has been applied, divided by the original number of tagged events. The ratio of total PID efficiency in data and Monte Carlo is found to be 0.84% deviation from unity per track. So the final systematic error of pion identification is 1.7%.

4.7.3 Background B decay modes branching fraction

In order to take branching fractions' uncertainty, the normalization factors of $B^0 \to J/\psi K^{*0}$, $B^0 \to J/\psi K_0^*(1430)^0$, $B^0 \to J/\psi K_2^*(1430)^0$, $B^\pm \to J/\psi K^\pm$ and $B^\pm \to J/\psi \pi^\pm$ are varied by $\pm 1\sigma$ of its branching fraction(see Table 3.4) and perform again the fit to ΔE to see the change of $B^0 \to J/\psi \pi^+\pi^-$ signal yield. The results are summarized in Table 4.10. All the listed yield changes are summed up in quadrature. The effect on $\mathrm{Br}(B^0 \to J/\psi \pi^+\pi^-)$ is estimated to be 3.2 %.

Background mode	Signal yield change
$B^0 \to J/\psi K^*(892)^0$	1.2 %
$B^0 \to J/\psi K_0^*(1430)^0$	1.1 %
$B^0 \to J/\psi K_2^*(1430)^0$	2.8 %
$B^0 \to J/\psi K^\pm$	0.2 %
$B^0 \to J/\psi \pi^\pm$	negligible

Table 4.10: Systematic error for each decay mode branching fraction uncertainty in Δ E background.

4.7.4 Non-J/ψ background parametrization in ΔE distribution

As discussed in section 4.1.1, the non-J/ψ background is expressed as a first order polynomial. For comparison, the fit using second order polynomial is also performed in Figure 4.37. Here, we obtain 447 $\pm$ 30 events as the signal yield of $B^0 \to J/\psi \pi^+\pi^-$ including $B^0 \to J/\psi K_S^0$. The systematic error of $B^0 \to J/\psi \pi^+\pi^-$ is calculated as 2.8 % by the

deviation from the number of signal (=435 ± 29) obtained by the nominal fit (Figure 4.1).

Same procedure is applied also to the subsamples divided by $M_{\pi^+\pi^-}$ bins, and the background $M_{\pi^+\pi^-}$ function is remade as Figure 4.38. With this remade background $M_{\pi^+\pi^-}$ PDF, the it to $M_{\pi^+\pi^-}$ distribution is performed. In this fit, the efficiency-corrected signal yields for $B^0 \to J/\psi\rho^0$, $B^0 \to J/\psi f_2$ and non-resonant $B^0 \to J/\psi\pi^+\pi^-$ decays are obtained to be 1008 ± 97, 106 ± 49 and 56 ± 95 events, respectively. The deviations from those by the nominal fit 991 ± 99, 60 ± 45 and 73 ± 92 are regarded as a systematic error; 1.8 %, 77.8 %, 22.9 %.

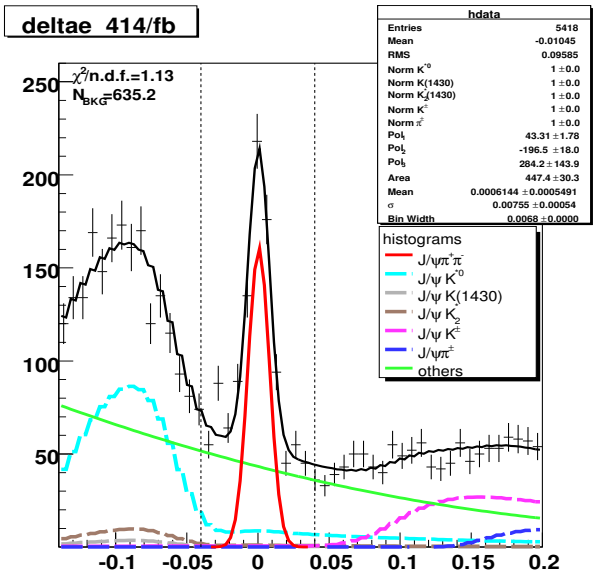

Figure 4.37: ΔE distribution with the fit result for systematic study. Not a first order polynomial but a 2nd order poly nominal is used to describe the non-J/ψ background.

4.7.5 Background $M_{\pi^+\pi^-}$ PDF parameterization

The background PDF was parameterized with 4th order polynomial as shown in Figure 4.29. The difference in the obtained signal yields from the case of 5th order is taken into account as a systematic error, 2.0 %, 21.7 % and 11.5 % for $B^0 \to J/\psi\rho^0$, $B^0 \to f_2$ and non-resonant $B^0 \to J/\psi\pi^+\pi^-$, respectively.

4.7.6 Background $M_{\pi\pi}$ PDF normalization

Fixing the shape of the background $M_{\pi^+\pi^-}$ distribution, normalization factor is floated in the fit shown in Figure 4.39. By this fit, the error for the normalization factor is estimated

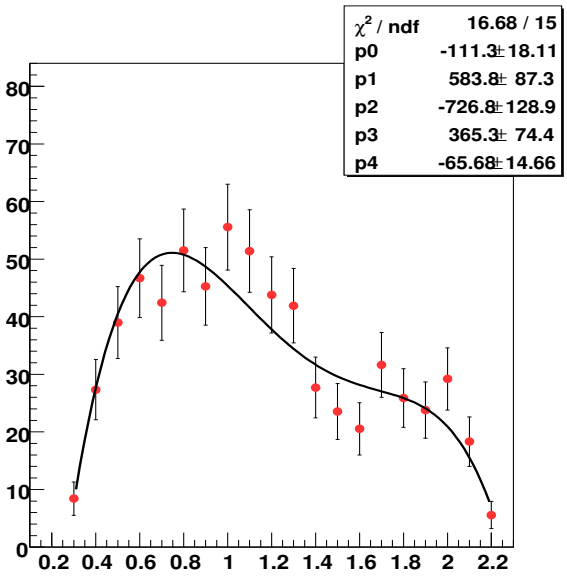

Figure 4.38: Background PDF as a function of $M_{\pi^+\pi^-}$,expressed as a 4th order polynomial for systematic study.

Background PDF	Signal Yield		
	$B^0 \to J/\psi\rho^0$	$B^0 \to J/\psi f_2$	nr-$B^0 \to J/\psi\pi^+\pi^-$
5th order	1010 ± 106	72 ± 53	64 ± 94

Table 4.11: Signal yields for each component by the background $M_{\pi^+\pi^-}$ PDF described as a 5th order polynomial.

to be 3.8 %. The amount of the background is varied by this error ($\sigma = 3.8\%$) and perform again the fit to $M_{\pi\pi}$. The change of the signal yield is taken into account as a systematic error.

Background Normalization	Yield change		
	$B^0 \to J/\psi\rho^0$	$B^0 \to J/\psi f_2$	nr-$B^0 \to J/\psi\pi^+\pi^-$
$\pm$3.8 %	2.2 %	6.3 %	70 %

Table 4.12: Systematic error for the normalization of background PDF in $M_{\pi^+\pi^-}$ fit.

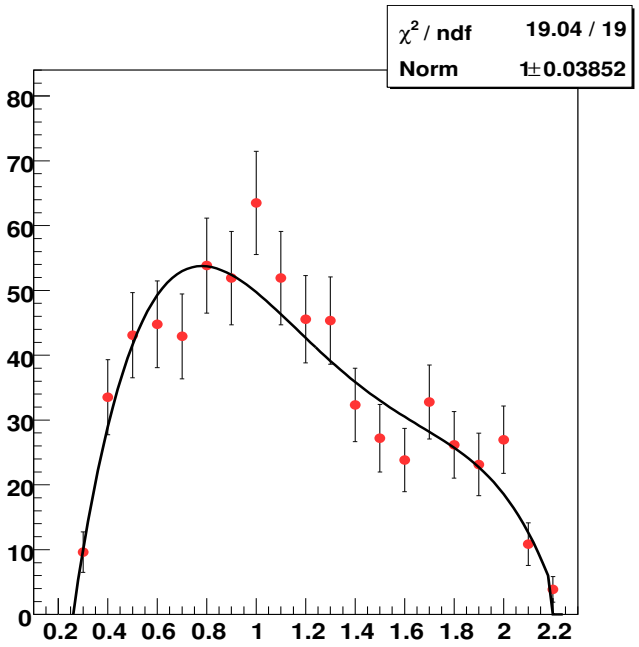

Figure 4.39: Fitting result with the background PDF to obtain possible normalization of this function.

4.7.7 The number of $B\overline{B}$

The number of $B\overline{B}$ pairs produced and measured with Belle experiment as 449.3 $\pm$ 5.7 $\times 10^6$ events. The error is due to the uncertainties in the hadronic events selection.

4.7.8 $\epsilon(M_{\pi^+\pi^-})$ modeling

We used the efficiency curve obtained by $B^0 \to J/\psi\pi^+\pi^-$ `PHSP` signal Monte Carlo as a universal one to perform an acceptance correction for all three considered process:

$B^0 \to J/\psi\pi^+\pi^-$ PHSP, $B^0 \to J/\psi\rho^0$ and $B^0 \to J/\psi f_2$, as described in section 4.4. The differences of efficiency values among these three modes listed in Table 4.7 are considered as systematic errors.

4.7.9 Breit-Wigner model uncertainty

The fit is carried out by changing the effective orbital angular momentum L_{eff} within possible range. Two different Blatt-Weiscopf barrier-factor radius R are also compared. The results are summarized in Table 4.13 and 4.14. The maximum variations of the signal yield of each decay is assigned as systematic errors.

$L_{eff}(\rho^0)$, $L_{eff}(f_2)$	Signal Yield		
	$B^0 \to J/\psi\rho^0$	$B^0 \to J/\psi f_2$	nr $B^0 \to J/\psi\pi^+\pi^-$
0,1	1034	27	65
0,2	1032	29	60
0,3	1030	34	58
1,1	1004	37	82
1,2	1001	39	79
1,3	998	44	78
2,1	998	47	87
2,2	984	50	86
2,3	979	55	86
average value	1006	40	76

Table 4.13: Fitted area numbers for each L_{eff} value in case of R=0.5.

$L_{eff}(\rho^0)$, $L_{eff}(f_2)$	Signal Yield		
	$B^0 \to J/\psi\rho^0$	$B^0 \to J/\psi f_2$	nr $B^0 \to J/\psi\pi^+\pi^-$
0,1	1019	41	61
0,2	1013	49	59
0,3	1006	59	58
1,1	998	52	74
*1,2	991	60	73
1,3	982	69	72
2,1	984	62	78
2,2	975	70	78
2,3	964	79	78
average value	992	60	70

Table 4.14: Fitted area numbers for each L_{eff} value in case of R=1.0. *These fitting results are used used for the final fit.

4.7.10 Uncertainties of masses and widths of ρ^0 and f_2 mesons

Table 4.15 shows mass and width of ρ^0 and f_2 meson from PDG[16]. The $M_{\pi^+\pi^-}$ fits are made for the error variation of each parameter. The errors are added in quadrature to give a total uncertainty 0.4 %, 0.9 % and 1.4 % for $B^0 \to J/\psi\rho^0$, $B^0 \to J/\psi f_2$ and non-resonant $B^0 \to J/\psi\pi^+\pi^-$.

	ρ^0	f_2
Mass (MeV/c^2)	775.5 $\pm$ 0.4	1275.4 $\pm$ 1.1
Width (MeV/c^2)	146.4 $\pm$ 1.1	184.4 $\pm$ 3.9

Table 4.15: PDG value related to ρ^0 and f_2.

Parameter	Systematic Error		
	$B^0 \to J/\psi\rho^0$	$B^0 \to J/\psi f_2$	nr-$B^0 \to J/\psi\pi^+\pi^-$
Mass(ρ^0)	0.12 %	0.61 %	0.15 %
Width(ρ^0)	0.41 %	0.19 %	1.34 %
Mass(f_2)	0.03 %	0.47 %	0.21 %
Width(f_2)	0.06 %	0.50 %	0.17 %

Table 4.16: Systematic error for the normalization of background PDF in $M_{\pi^+\pi^-}$ fit.

4.7.11 Branching fractions of sub-decay modes

The uncertainty arising from the sub-decay branching fraction is listed in Table 4.17. We estimate the amount of these uncertainties' effect on the final branching fractions.

Mode	Branching fraction
$J/\psi \to l^+l^-$	(11.87 $\pm$ 0.12) %
$f_2 \to \pi^+\pi^-$	(56.5 $\pm$ 1.7) %

Table 4.17: Branching fractions and uncertainties of sub-decay modes related to this analysis[16].

4.7.12 Total systematic uncertainties

A detail of the considered systematic errors and their contribution to the total $\mathcal{B}(B^0 \to J/\psi\pi^+\pi^-)$ is shown in Table 4.18. The errors are added in quadrature to give a total uncertainty of 7.5 %.

	$B^0 \to J/\psi\pi^+\pi^-$
total	$\pm$ 8.4 %
Track reconstruction	$\pm$ 4.9 %
Lepton-ID	$\pm$ 3.8 %
$\pi^{\pm}$-ID	$\pm$ 1.7 %
B.G. B decay mode br.	$\pm$ 3.2 %
Non-J/ψ B.G. parametrization	$\pm$ 2.8 %
Background PDF normalization	$\pm$ 2.8 %
N_{B^0}	$\pm$ 1.3 %
ϵ	$\pm$ 1.2 %
$\mathcal{B}(J/\psi \to l^+l^-)$	$\pm$ 1.0 %

Table 4.18: A beakdown of the considered systematic errors and their contribution to the $\mathcal{B}(B^0 \to J/\psi\pi^+\pi^-)$.

A details of the considered systematic errors and their contribution to the $\mathcal{B}(B^0 \to J/\psi\rho^0)$, $\mathcal{B}(B^0 \to J/\psi f_2)$ and non-resonant $B^0 \to J/\psi\pi^+\pi^-$ is shown in Table 4.19. The errors are added in quadrature to give a total uncertainty of 12.9 %, 75.4 % and 87.1 %, respectively.

4.8 The branching fractions

The branching fraction of total $B^0 \to J/\psi\pi^+\pi^-$ is obtained from the result shown in Figure 4.1. The branching fraction of $B^0 \to J/\psi\rho^0$, $B^0 \to J/\psi f_2$ and non-resonant $B^0 \to J/\psi\pi^+\pi^-$ is obtained from the result shown in Figure 4.34.

4.8.1 The total branching fraction for $B^0 \to J/\psi\pi^+\pi^-$ decay

The branching fraction of total $B^0 \to J/\psi\pi^+\pi^-$ is calculated using the formula

$$\mathcal{B}(B^0 \to J/\psi\pi^+\pi^-) = \frac{N_{J/\psi\pi^+\pi^-}}{N_{B^0.} \times \epsilon \times \mathcal{B}(J/\psi \to l^+l^-)}. \tag{4.22}$$

- $N_{J/\psi\pi^+\pi^-}$: the total signal yield obtained from the fit to ΔE distribution
- N_{B^0} : the total number of neutral B mesons in the data sample
- ϵ : the efficiency for $B^0 \to J/\psi\pi^+\pi^-$ decays

The values used for the calculation are shown in Table 4.20. The branching fraction is obtained to be

$$\mathcal{B}(B^0 \to J/\psi\pi^+\pi^-) = (2.2 \pm 0.3(stat.) \pm 0.2(sys.)) \times 10^{-5}.$$

	$B^0 \to J/\psi\rho^0$	$B^0 \to J/\psi f_2$	nr $B^0 \to J/\psi\pi^+\pi^-$
total	$\pm$ 10.8 %	$\pm$97.6 %	$\pm$77.4 %
Track reconstruction	$\pm$ 4.9 %	$\pm$ 4.9 %	$\pm$ 4.9 %
Lepton-ID	$\pm$ 3.8 %	$\pm$ 3.8 %	$\pm$ 3.8 %
$\pi^{\pm}$-ID	$\pm$ 1.7 %	$\pm$ 1.7 %	$\pm$ 1.7 %
Non-J/ψ B.G. parametrization	$\pm$ 1.8 %	$\pm$ 77.8 %	$\pm$ 22.9 %
Background PDF normalization	$\pm$ 2.2 %	$\pm$ 6.3 %	$\pm$ 69.8 %
Background PDF parameterization	$\pm$ 2.0 %	$\pm$ 21.7 %	$\pm$ 11.5 %
N_{B^0}	$\pm$ 1.3 %	$\pm$ 1.3 %	$\pm$ 1.3 %
Signal Monte Carlo statistics	$\pm$ 1.8 %	$\pm$ 1.8 %	$\pm$ 1.8 %
$\epsilon(M_{\pi^+\pi^-})$ modeling	$\pm$ 6.0 %	$\pm$ 1.5 %	——
Unknown parameters in BW	$\pm$ 4.4 %	$\pm$ 53.9 %	$\pm$ 20.3 %
Mass(ρ^0,f_2) & Width(ρ^0, f_2)	$\pm$ 0.9 %	$\pm$ 0.6 %	$\pm$ 1.4 %
$\mathcal{B}(J/\psi \to l^+l^-)$	$\pm$ 1.0 %	$\pm$ 1.0 %	$\pm$ 1.0 %
$\mathcal{B}(f_2 \to \pi^+\pi^-)$	——	$\pm$ 3.0 %	——

Table 4.19: A details of the considered systematic errors and their contribution to the $\mathcal{B}(B^0 \to J/\psi\rho^0)$, $\mathcal{B}(B^0 \to J/\psi f_2)$ and $\mathcal{B}(\mathrm{nr}B^0 \to J/\psi\pi^+\pi^-)$.

Systematic error estimation is described in section 4.7.12.

$N_{J/\psi\pi^+\pi^-}$	334 ± 40
N_{B^0}	$(44.93 \pm 0.57) \times 10^7$
ϵ	0.281 ± 0.005
$\mathcal{B}(J/\psi \to l^+l^-)$	0.119 ± 0.001

Table 4.20: The relevant numbers to obtain $\mathcal{B}(B^0 \to J/\psi\pi^+\pi^-)$.

4.8.2 The branching fraction for $B^0 \to J/\psi\rho^0$ mode

The branching fraction of $B^0 \to J/\psi\rho^0$ is calculated using the formula

$$\mathcal{B}(B^0 \to J/\psi\rho^0) = \frac{N_{J/\psi\rho^0}}{N_{B^0} \times \mathcal{B}(J/\psi \to l^+l^-)}. \tag{4.23}$$

- $N_{J/\psi\rho^0}$: the total signal yield obtained from the fit to $M_{\pi\pi}$ distribution
- N_{B^0} : the total number of neutral B mesons in the data sample

The values used for the calculation are shown in Table 4.21. Note that $N_{J/\psi\rho^0}$ is efficiency corrected numbers as described in section 4.5. The $\rho^0 \to \pi^+\pi^-$ branching fraction is

assumed to be 100 % with no uncertanies, because other ρ^0 decay modes have negligibly small branching fractions composed to all other statistical and systematic errors in this analysis. The branching fraction is obtained to be

$$\mathcal{B}(B^0 \to J/\psi\rho^0) = (1.9 \pm 0.2(stat.) \pm 0.2(sys.)) \times 10^{-5}. \tag{4.24}$$

Systematic error estimation is described in section 4.7.12.

$N_{J/\psi\rho^0}$	990 ± 99
N_{B^0}	$(44.93 \pm 0.57)\ \times 10^7$
$\mathcal{B}(J/\psi \to l^+l^-)$	0.119 ± 0.002

Table 4.21: The relevant numbers to obtain $\mathcal{B}(B^0 \to J/\psi\rho^0)$.

4.8.3 The upper limit of branching fraction for $B^0 \to J/\psi f_2$ mode

The branching fraction of $B^0 \to J/\psi f_2$ is calculated using the formula

$$\mathcal{B}(B^0 \to J/\psi f_2) = \frac{N_{J/\psi f_2}}{N_{B^0} \times \mathcal{B}(J/\psi \to l^+l^-) \times \mathcal{B}(B^0 \to J/\psi f_2)}. \tag{4.25}$$

- $N_{J/\psi f_2}$: the total signal yield obtained from the fit to $M_{\pi\pi}$ distribution
- N_{B^0} : the total number of neutral B mesons in the data sample

The values used for the calculation are shown in Table 4.22. Note that $N_{J/\psi f_2}$ has been corrected by efficiency as described in section4.5. The branching fraction is obtained to be

$$\mathcal{B}(B^0 \to J/\psi f_2) = (2.0 \pm 1.5(stat.) \pm 1.9(sys.)) \times 10^{-6}.$$

The significance is calculated as

$$\begin{aligned} s &= \sqrt{2\ln L_{max} - 2\ln L_\alpha} \\ &= 2.6\sigma, \end{aligned} \tag{4.26}$$

where L_{max} and L_α is the maximum likelihood of the fit, and $-2\ln L_{max}$ and $-2\ln L_\alpha$ is obtained from the results shown in Figure 4.33 (considering only ρ^0 resonance) and 4.32 (considering f_2 resonance also), respectively. If we assume that the uncertainty of the result follows a Gaussian distribution, we can calculate the upper limit ($N_{U.L.}$) as

$$N_{U.L.} = N_{val} + N_{err} \times 1.28, \tag{4.27}$$

where N_{val} is the center value of the obtained signal yield, N_{err} is the quadratic sum of statistic and systematic errors. 1.28 corresponds to the limit giving 90 % C.L.[16]. The obtained value is

$$\mathcal{B}(B^0 \to J/\psi f_2) < 4.9 \times 10^{-6} (@90\%\text{C.L.}).$$

Systematic error estimation is described in section 4.7.12.

$N_{J/\psi f_2}$	60 ± 45
N_{B^0}	$(44.93 \pm 0.57) \times 10^7$
$\mathcal{B}(J/\psi \to l^+l^-)$	0.119 ± 0.002
$\mathcal{B}(f_2 \to \pi^+\pi^-)$	0.565 ± 0.170

Table 4.22: The relevant numbers to obtain $\mathcal{B}(B^0 \to J/\psi f_2)$.

4.8.4 The upper limit of branching fraction for non-resonant $B^0 \to J/\psi\pi^+\pi^-$ mode

The branching fraction of non-resonant (=nr) $B^0 \to J/\psi\pi^+\pi^-$ is calculated using equation

$$\mathcal{B}(\text{nr}B^0 \to J/\psi\pi^+\pi^-) = \frac{N_{\text{nr}J/\psi\pi^+\pi^-}}{N_{B^0} \times \mathcal{B}(J/\psi \to l^+l^-)}. \tag{4.28}$$

- $N_{nrJ/\psi\pi^+\pi^-}$: the total signal yield obtained from the fit to $M_{\pi\pi}$ distribution
- N_{B^0} : the total number of neutral B mesons in the data sample

The values used for the calculation are shown in Table 4.23. Note that $N_{J/\psi f_2}$ has been corrected by efficiency as described in section 4.5. The branching fraction is obtained to be

$$\mathcal{B}(\text{nr}B^0 \to J/\psi\pi^+\pi^-) = (1.4 \pm 1.7(stat.) \pm 1.1(sys.)) \times 10^{-6},$$

the upper limit is calculated using Equation 4.27.

$$\mathcal{B}(\text{nr}B^0 \to J/\psi\pi^+\pi^-) < 4.0 \times 10^{-6} (@90\%\text{C.L.})$$

Systematic error estimation is described in section 4.7.12.

4.9 Comparison with previous experiments

The previous measurements for the branching fractions for $B^0 \to J/\psi\pi^+\pi^-$ and $B^0 \to J/\psi\rho^0$ have been reported by the BaBar collaboration with their data sample corresponding to 56 million $B\overline{B}$ pairs[6]. Figure 4.40 shows our results compared with that of

$N_{\mathrm{nr}J/\psi\pi^+\pi^-}$	73 ± 92
N_{B^0}	$(44.93 \pm 0.57)\ \times 10^7$
$\mathcal{B}(J/\psi \to l^+l^-)$	0.119 ± 0.001

Table 4.23: The relevant numbers to obtain $\mathcal{B}(\mathrm{nr}B^0 \to J/\psi\pi^+\pi^-)$.

BaBar. Our result on $\mathrm{B}(B^0 \to J/\psi\rho^0)$ is in good agreement with BaBar, while their $\mathrm{B}(B^0 \to J/\psi\pi^+\pi^-)$ exhibits slightly higher value than ours. This is mainly because they claimed that there is an existence of non-resonant $B^0 \to J/\psi\pi^+\pi^-$. This time we are using 8 times larger data sample. Its very rich statistics enabled us to perform the model-independent determination of background's $M_{\pi^+\pi^-}$ distribution as described in section 4.3.4, and the binned maximum likelihood fit taking the interference among possible contributions into account. Under such improved situation, we have not observed any significant signature of non-resonant $B^0 \to J/\psi\pi^+\pi^-$ decay. The deviation is still 2σ level, so it can be understood as a statistical fluctuation.

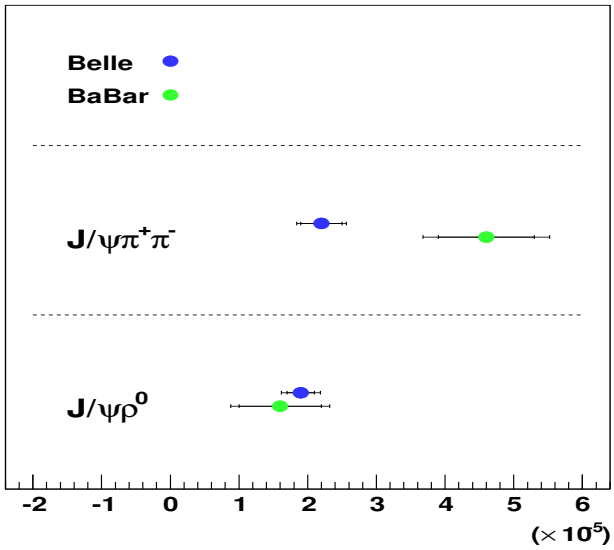

Figure 4.40: The branching fractions for $B^0 \to J/\psi\pi^+\pi^-$ and $B^0 \to J/\psi\rho^0$. The blue and green circles show the results from the Belle and BaBar experiments[6], respectively. Both statistical and total errors are shown by shorter and longer error bars.

Chapter 5

Conclusion

We have measured the branching fractions for B^0 meson decay to the final state $J/\psi\pi^+\pi^-$ and its sub-processes:

$$\mathcal{B}(B^0 \to J/\psi\pi^+\pi^-) = (2.2 \pm 0.3(stat.) \pm 0.2(sys.)) \times 10^{-5},$$
$$\mathcal{B}(B^0 \to J/\psi\rho^0) = (1.9 \pm 0.2(stat.) \pm 0.2(sys.)) \times 10^{-5},$$
$$\mathcal{B}(B^0 \to J/\psi f_2) < 4.9 \times 10^{-6} (@\ 90\%\ \text{C.L.}),$$
$$\mathcal{B}(\text{nr}B^0 \to J/\psi\pi^+\pi^-) < 4.0 \times 10^{-6} (@\ 90\%\ \text{C.L.}),$$

based on data samples of 449 million $B\overline{B}$ pairs recorded by the Belle detector at the KEKB collider. We found that $B^0 \to J/\psi\rho^0$ is the dominant decay mode in the final state $B^0 \to J/\psi\pi^+\pi^-$ and determine its branching fraction most precisely. We set the upper limit for $B^0 \to J/\psi f_2(1270)$ decay at 90% C.L. Among the same kind of measurements carried out so far, the most recent one is BaBar's measurement[6] based on their data sample corresponding to 56 million $B\overline{B}$. The analysis presented in this thesis has superseded it with 8 times larger data sample, a model-independent determination of the background $M_{\pi^+\pi^-}$- distribution function and the binned maximum likelihood fit taking the interference among possible contributions into account.

Appendix A

CP Violation in the B Meson System

A.1 Definitions of P, C and T Operators

The parity operator, P produces the operation of spatial inversion of coordinates

$$(x, y, z) \implies (-x, -y, -z).$$

Let us define a spin and momentum of particle f as $\vec{\sigma}$ and $\vec{p}$, respectively.
The state of $|f; \vec{\sigma}\ \vec{p}\rangle$ is transformed by the operator P as

$$P|f; \vec{\sigma}\ \vec{p}\rangle = \eta_P |f; \vec{\sigma}\ \vec{p}\rangle,$$

where η_P is a phase of parity transformation. Since P^2 is an identical operator, ${\eta_P}^2$ is 1, and thus $\eta_P = \pm 1$.

The Charge conjugation operator, C changes the sign of internal charges such as electric charge, baryon number and so on. This operation replaces particle f with thier antiparticles $\overline{f}$ (and vice versa) as

$$C|f; \vec{\sigma}\ \vec{p}\rangle = \eta_C |\overline{f}; \vec{\sigma}\ \vec{p}\rangle,$$

where η_C is a phase.

The third fundamental operator, T is a time reversal transformation which inverse the time coordinates:

$$T|f; \vec{\sigma}\ \vec{p}\rangle = \eta_T |\overline{f}; -\vec{\sigma}\ -\vec{p}\rangle,$$

where η_T is a phase. Table A.1 is shown the effects of P, C and T transformation on each parameter.

According to the CPT theorem, the combined operation CPT is invariant in relativistic field theory.

		C	P	T
r	(spatial coordinates)	r	$-r$	r
p	(momentum)	p	$-p$	$-p$
J	(angular momentum)	J	J	$-J$
σ	(spin)	σ	σ	$-\sigma$
E	(electric field)	$-E$	$-E$	E
B	(magnetic field)	$-B$	$-B$	$-B$
$\sigma \cdot p$	(helicity)	$\sigma \cdot p$	$-\sigma \cdot p$	$\sigma \cdot p$

Table A.1: Behavior of various basic observables under C, P and T operations.

Until the early 1950's, one believed that all are conserved under each of these transformation, C, P and T. In 1956, however, T. Lee and C. Yang pointed out the violation of the parity conservation[7], and the subsequent experiments by C. Wu *et al.* and by R. Garwin *et al.* in 1957 independently demonstrated that weak interactions violate C-invariance just as they violate P-invariance in weak decays of nuclei and of muons [8] [9]. This violation is visualized by the longitudinal polarization of neutrinos and antineutrinos. Neutrino has helicity of -1 (left-handed), and antineutrino has a helicity $+1$. As illustrated in Figure A.1, left-handed neutrino applied P or C operation is not observed experimentally. However, the combine operation CP, which transforms a left-handed neutrino into right-handed neutrino, is not forbidden.

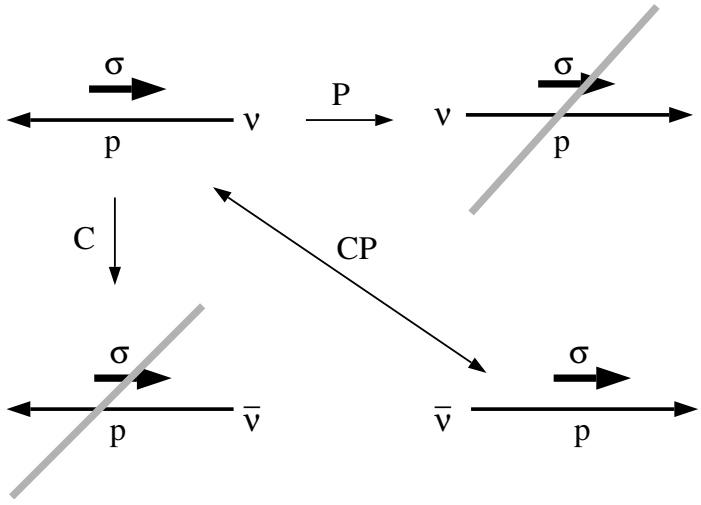

Figure A.1: Results of the C, P and CP operations on neutrino states. Only left-handed neutrino (left-top), and right-handed neutrino which is result of appliying CP operation to left-handed neutrino (right-bottom), are observed in nature.

A.2 CP Violation in K Meson System

Following the discovery of parity violation in weak decay processes in 1957, it was believed that the weak interactions were at least invariant under the CP operation. However, L. H. Christenson, J. W. Cronin, V. L. Fitch, and R. Turlay discovered the violation of the CP system in K^0 meson decays[10]. There are two neutral strange mesons, K^0 and $\overline{K}^0$. The quark contents of them are

$$K^0(\overline{s}d) \ , \quad \overline{K}^0(s\overline{d}).$$

As shown in Figure A.2. K^0 and $\overline{K}^0$ can mix via exchange of W bosons, which is called "box diagrams".

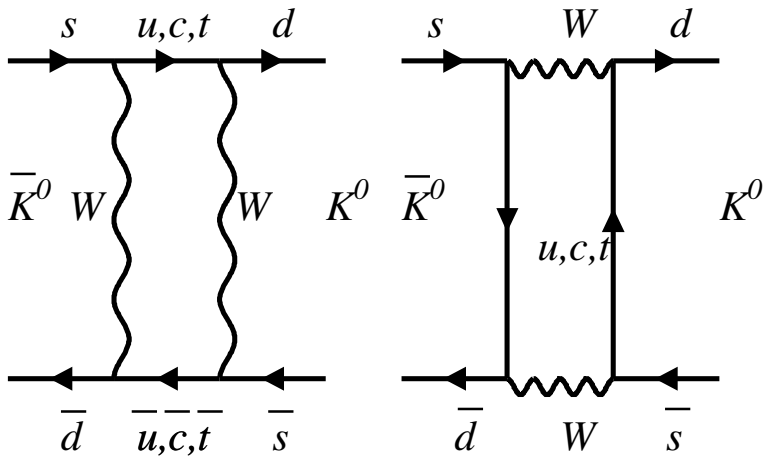

Figure A.2: $K^0 - \overline{K}^0$ mixing

We define that operation of CP on the states K^0 and $\overline{K}^0$ gives $CP|K^0\rangle = |\overline{K}^0\rangle$ and $CP|\overline{K}^0\rangle = |K^0\rangle$. We can form the linear combinations of K^0 and $\overline{K}^0$ as a CP eigenstate of neutral K mesons:

$$\begin{aligned} |K_1\rangle &= \frac{1}{\sqrt{2}}(|K^0\rangle + |\overline{K}^0\rangle) \\ |K_2\rangle &= \frac{1}{\sqrt{2}}(|K^0\rangle - |\overline{K}^0\rangle) \end{aligned}$$

where

$$\begin{aligned} CP|K_1\rangle &= +|K_1\rangle \qquad (CP = +1) \\ CP|K_2\rangle &= -|K_2\rangle \qquad (CP = -1) \end{aligned}$$

Experimentally, it was observed that there are two lifetime of neutral K mesons, where the shorter lived was named K_S, and the longer lived was named K_L. Since it was measured that K_S decays into two-pions of which CP eigenvalue is $+1$, and K_L decays three-pions of which CP eigenvalue is -1, it was considered that K_S and K_L correspond to the K_1 and K_2 respectively, at that time. The longer life of K_L is due to limited phase space. Under the CP conservation, $K_L \to \pi^+ \pi^-$ is forbidden. However, L. H. Christenson *et al.* group discovered the small fraction decay of $K_L \to \pi^+\pi^-$. The branching fraction was order of $\sim 10^{-3}$. Thus, K_L should be rewritten as

$$|K_L\rangle = \frac{1}{\sqrt{(2(1+|\epsilon|^2)}}((1+\epsilon)|K^0\rangle - (1-\epsilon)|\overline{K}^0\rangle)$$

It means there is CP violation with ϵ between K^0 and $\overline{K}^0$. Charged asymmetries in $K_L \to \pi^\pm e^\mp \nu$[11] and $K_L \to \pi^\pm \mu^\mp \nu$[12] also confirmed the CP violation in neutral K meson system. The theoretical explanation within the Standard Model for the origin of the CP violation was proposed by Kobayashi and Maskawa in 1973[1], which is described in the next section.

A.3 Kobayashi-Maskawa Model

In 1973, M. Kobayashi and T. Maskawa proposed that the existence of at least three quark generations, six quarks, can explain the CP violation, even though only three quarks had been observed, at that time. After that, c, b, and t quark were discovered in 1974, 1977 and 1995, respectively, and thus Kobayashi-Maskawa mechanism becomes a essential part of the Standard Model.

In the Standard Model, six quarks form the three doublets that are called as three quark generations:

$$\begin{pmatrix} u \\ d \end{pmatrix} \qquad \begin{pmatrix} c \\ s \end{pmatrix} \qquad \begin{pmatrix} t \\ b \end{pmatrix}$$

in terms of mass eigenstates. The Lagrangian of charged-current weak interaction is expressed as

$$\mathcal{L} = \frac{g}{\sqrt{2}} \left\{ (\overline{u}, \overline{c}, \overline{t})_L \gamma^\mu W^+_\mu V_{KM} \begin{pmatrix} d \\ s \\ b \end{pmatrix}_L + (\overline{d}, \overline{s}, \overline{b})_L \gamma^\mu W^-_\mu V^\dagger_{KM} \begin{pmatrix} u \\ c \\ t \end{pmatrix}_L \right\}$$

where,

$$\begin{aligned} g &: \text{coupling constant} \\ \gamma^\mu &: \gamma \text{ matrix} \\ W^\pm &: W \text{ bosons} \\ \begin{pmatrix} d \\ s \\ b \end{pmatrix}_L \text{ or } \begin{pmatrix} u \\ c \\ t \end{pmatrix}_L &: \text{left} - \text{handed quark} \end{aligned}$$

and V_{KM} is mixing matrix named Kobayashi-Maskawa matrix.

$$V_{KM} = \begin{pmatrix} V_{ud} & V_{us} & V_{ub} \\ V_{cd} & V_{cs} & V_{cb} \\ V_{td} & V_{ts} & V_{tb} \end{pmatrix} \tag{A.1}$$

Since V_{KM} is unitary matrix, it satisfy:

$$V_{KM}^{\dagger} V_{KM} = \begin{pmatrix} V_{ud}^* & V_{cd}^* & V_{td}^* \\ V_{us}^* & V_{cs}^* & V_{ts}^* \\ V_{ub}^* & V_{cb}^* & V_{tb}^* \end{pmatrix} \begin{pmatrix} V_{ud} & V_{us} & V_{ub} \\ V_{cd} & V_{cs} & V_{cb} \\ V_{td} & V_{ts} & V_{tb} \end{pmatrix} = I \tag{A.2}$$

Thus,

$$\sum_{i=u,c,t} V_{ij}^* V_{ik} = \delta_{jk} \quad (j,k = d,s,b) \tag{A.3}$$

The matrix elements are parametrized by three real parameters and a complex phase. The complex phase introduces CP violation. It is convenient to write the matrix in Wolfenstein parametrization[13] which is an expansion in powers of sin of Cabibbo angle, $\lambda \equiv \sin\theta_c \simeq 0.22$:

$$V_{KM} = \begin{pmatrix} 1-\lambda^2/2 & \lambda & A\lambda^3(\rho - i\eta) \\ -\lambda & 1-\lambda^2/2 & A\lambda^2 \\ A\lambda^3(1-\rho-i\eta) & -A\lambda^2 & 1 \end{pmatrix} + \mathcal{O}(\lambda^4)$$

Among Equation A.2, the relation involving V_{td} and V_{ub}, which relate B meson decays, results in

$$V_{ud}V_{ub}^* + V_{cd}V_{cb}^* + V_{td}V_{tb}^* = 0$$

Each term is expressed in Wolfenstein parametrization

$$\begin{aligned} V_{ud}V_{ub}^* &\simeq A\lambda^3(\rho + i\eta) \\ V_{cd}V_{cb}^* &\simeq -A\lambda^3 \\ V_{td}V_{tb}^* &\simeq A\lambda^3(1-\rho-i\eta) \end{aligned}$$

The three terms form a closed triangle in the complex plane, which is called "unitarity triangle", as shown in Figure A.3. The three angle of the triangles are defined as

$$\phi_1 \equiv \arg\left(\frac{V_{cd}V_{cb}^*}{V_{td}V_{tb}^*}\right), \ \phi_2 \equiv \arg\left(\frac{V_{ud}V_{ub}^*}{V_{td}V_{tb}^*}\right), \ \phi_3 \equiv \arg\left(\frac{V_{cd}V_{cb}^*}{V_{ud}V_{ub}^*}\right)$$

Since the length of all three sides are the same order of $\mathcal{O}(\lambda^3)$, we can expect large CP violation such as $\mathcal{O}(0.1) \sim \mathcal{O}(1)$ in the B meson systems.

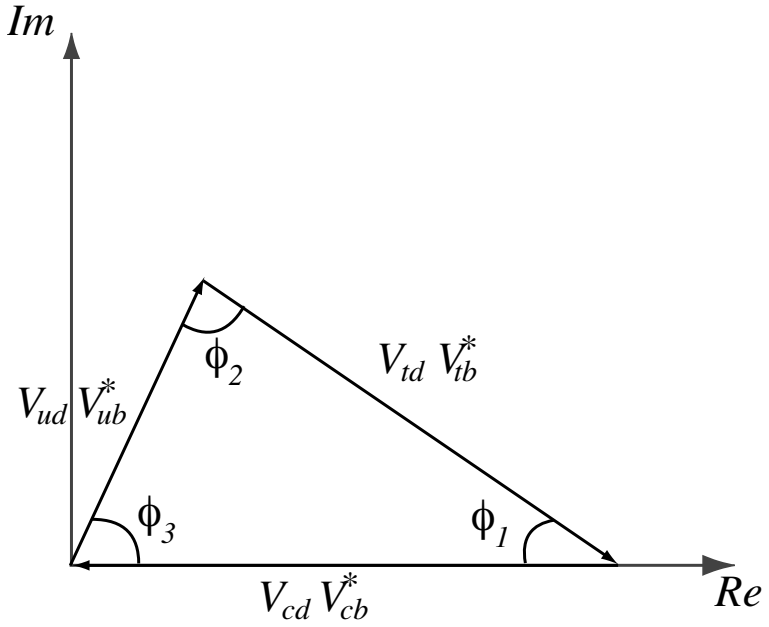

Figure A.3: The unitarity triangle.

A.4 The different types of CP violation

There are three ways in which CP violation can manifest itself in the SM.
These are:

1. CP violation in decay;
2. CP violation in mixing;
3. CP violation in the intereferenc between decays with and without mixing.

A.4.1 CP violation in decay

CP violation in decay is described by the quantity

$$l = \left| \frac{\overline{A}_{\overline{f}}}{A_f} \right| \tag{A.4}$$

,where $A_f = \langle B^0|H|f\rangle$ represents the amplitude of a B^0 decaying to a final state f, and $\overline{A}_{\overline{f}} = \langle \overline{B}^0|H|\overline{f}\rangle$ represents the amplitude of a B^0 decaying to the anti-particle of f. It turns out that l is independent of phase conventions and therefore has physical meaning. CP violation in decay occurs if $l \neq 1$ and is also called *direct CP violation*. This type of CP violation comes from interference between different terms in the decay amplitude.

In the SM the amplitude can pick up phases from two different sources. Electroweak interaction terms gain phases through the CKM matrix elements (as discussed in section A.3) These are CP violating phases, which contribute with different signs to the

amplitudes A_f and $\overline{A}_{\overline{f}}$. They are called *weak phases* because they originate from the electroweak interaction term in the SM Lagrangian. So called *Strong phases* can also contribute to the amplitudes. These come from the contribution on intermediate on-shell states in the decays. The strong phases do not violate CP so they appear in both the amplitude $(A_f, \overline{A}_{\overline{f}})$ with equal signs.

Both these types of phases are convention dependent, but the difference between any two weak or strong phases is independent of convention and is physically meaningful.

For CP violation in decay to occur there must be more than one amplitude contribution to the decay $B \to f$. The total amplitude is then given by

$$A_f = \Sigma A_i e^{i(\delta_i + \phi_i)} \tag{A.5}$$

where the sum is over all the possible diagrams which contribute to the decay. A_i is the magnitude of the amplitude for the specific diagram and ϕ_i and δ_i are the weak and strong phases respectively. The quantity l is now given by following equation.

$$l = \left| \frac{\overline{A}_{\overline{f}}}{A_f} \right| = \left| \frac{\Sigma_i \overline{A}_{\overline{i}} e^{i(\delta_i - \phi_i)}}{\Sigma_i A_i e^{i(\delta_i + \phi_i)}} \right| \tag{A.6}$$

For direct CP violation to occur, there have to be at least two terms in the overall amplitudes that have different weak phases and different strong phases. This is because

$$|A|^2 - \left|\overline{A}\right|^2 = -2\Sigma A_i A_j \sin(\phi_i - \phi_j) \sin(\delta_i - \delta_j) \tag{A.7}$$

which shows that if either the strong or weak phases are the same for a contributing diagram then the difference in amplitude magnitudes vanishes, which is equivalent to $l = 1$. Thus for direct CP violation to be observed we look for decays in which penguin (or loop) diagrams contribute with a different weak phase from the tree diagram. The amplitudes for the tree and penguin diagrams should have a large similar magnitude as this will ensure relatively large interference terms. Direct CP violation is generally looked for in the decays of charged particles, although it also occurs in the decays of neutrals. In charged modes, however, it can not be confused with the other possible types of CP violation, which only occur in neutral decays. An example of a mode which satisfies these criteria, and is therefore a good candidate for observing direct CP violation, is $B^{\pm} \to \rho^{\pm}\pi^{\mp}$ (the tree and penguin diagrams for this decay are shown in Figure A.4).

Typically the asymmetry

$$a_f = \frac{\Gamma(B^+ \to f) - \Gamma(B^- \to \overline{f})}{\Gamma(B^+ \to f) + (B^- \to \overline{f})} = \frac{1 - l^2}{1 + l^2} \tag{A.8}$$

is used to look for CP violation in decays. Currently the world average [14], [15], [16] for this is

$$a_{\rho\pi}^{-+} = -0.48 \pm 0.14 \tag{A.9}$$

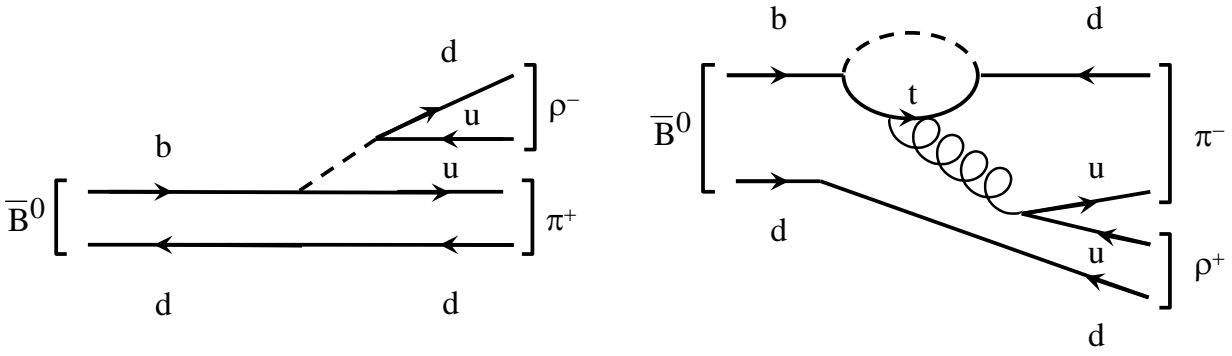

Figure A.4: The tree and penguin Feynman diagrams for the decay $\overline{B}^0 \to \rho\pi$.

A.4.2 CP violation in mixing

Although the explanation is done in section A.5, CP violation in mixing is often called *indirect CP violation*. It was CP violation of this type which first showed that CP is not an exact symmetry of nature[10]. The value of CP violation in mixing is measured in kaon decays using the semileptonic asymmetry.

$$a_{sl}^K = \frac{\Gamma(K_L \to l^+\overline{\nu}X) - \Gamma(K_L \to l^-\nu X)}{\Gamma(K_L \to l^+\overline{\nu}X) + (K_L \to l^-\nu X} = \frac{1-|q/p|^4}{1+|q/p|^4} \tag{A.10}$$

This asymmetry is thought to be small, of order 10^2 because in the B system $|q/p| \approx 1$. The further explanation is done in section A.5.

A.4.3 CP violation in the intereference between mixing and decay

It can be shown that the quantity

$$\lambda = \frac{q}{p}\frac{\overline{A}f_{CP}}{Af_{CP}} \tag{A.11}$$

is independent of phase convention and thus physically meaningful. Here $A_{f_{CP}}$ is the amplitude for the decay of a B^0 to a CP eigenstate (f_{CP}). The comvention deoendence of the mixing part ($\frac{q}{p}$) cancels with that of the decay part ($\frac{\overline{A}}{A}$). The condition $\lambda \neq 1$ allows *CP violation in the interference between mixing and decay* to occur.

This can occur along with both other types of CP violation e.g. $|\frac{q}{p}| \neq 1$ and/or $|\frac{\overline{A}}{A}| \neq 1$ but can also occur in the absence of these e.g. $|\lambda| = 1$ but $\Im(\lambda) \neq 0$. In this case λ is a pure phase which can be calculated without hadronic uncertainties.

The time-dependent amplitudes for the decay of a B^0 ($\overline{B}^0$) to a CP eigenstate f_{CP} are given in following Equations (these come from using the time-dependent states in Equation A.36 ,A.37).

$$\langle f_{CP}|\hat{H}|B^0(t)\rangle = A_{f_{CP}}(g_+(t) + \lambda g_-(t)) \tag{A.12}$$

$$\langle f_{CP}|\hat{H}|\overline{B}^0(t)\rangle = A_{f_{CP}}(q/p)(g_-(t) + \lambda g_+(t)) \tag{A.13}$$

where

$$g_{\pm} = \frac{1}{2}(e^{-i\mu_H t} \pm e^{-i\mu_L t}). \tag{A.14}$$

The time-dependent decay rates, which come from taking the modules squared of these amplitudes, are

$$\begin{aligned}
\Gamma(t)(B^0 \to f_{CP}) &= |\langle f_{CP}|\hat{H}|B^0(t)\rangle|^2 && \text{(A.15)}\\
&= |A_{CP}|^2 e^{-\Gamma t}\left[\frac{1+|\lambda|^2}{2} + \frac{1-|\lambda|^2}{2}\cos(\Delta m t) - \Im(\lambda)\sin(\Delta m t)\right], \\
\Gamma(t)(\overline{B}^0 \to f_{CP}) &= |\langle f_{CP}|\hat{H}|\overline{B}^0(t)\rangle|^2 && \text{(A.16)}\\
&= |A_{CP}|^2 e^{-\Gamma t}\left[\frac{1+|\lambda|^2}{2} - \frac{1-|\lambda|^2}{2}\cos(\Delta m t) + \Im(\lambda)\sin(\Delta m t)\right].
\end{aligned}$$

The time-dependent asymmetry is shown in Equation A.17. It is constructed by taking the difference between the two rates and dividing by the sum of the two.

$$\begin{aligned}
a_{f_{CP}}(t) &= \frac{\Gamma(B^0(t) \to f_{CP}) - \Gamma(\overline{B}^0(t) \to f_{CP})}{\Gamma(B^0(t) \to f_{CP}) + \Gamma(\overline{B}^0(t) \to f_{CP})} \\
&= \frac{(1-|\lambda|^2)\cos(\Delta m t) - 2\Im(\lambda) sin(\Delta m t)}{1+|\lambda|^2}
\end{aligned} \tag{A.17}$$

This quantity is non-zero if any of the three types of CP violation occur. If there is no direct or indirect CP violation (ie. $|\lambda| = 1$) the asymmetry reduces to

$$a_{f_{CP}} = \Im(\lambda)\sin(\Delta m_B t) \tag{A.18}$$

As will be seen in section A.8, this type of CP violation is the easiest to measure in B system. This is because the measured asymmetry can be related to the CKM elements without hadroninc uncertainties. For most B decays $\lambda \approx 1$, so both direct and indirect CP violation occur at a negligible level, while CP violation in the interference between mixing and decay can occur at a much greater level.

For kaons this is not the case as $\Im(\lambda(K^0 \to \pi^+\pi^-)) \approx \mathcal{O}^{-3}$. This is one of the big advantages of the B system, over the kaon system, for studying CP asymmetries.

A.5 CP Violation in B Decays

A.5.1 B^0-$\overline{B}^0$ Mixing with no CP violation

We start a neutral meson, which is made up of two quarks of different flavors, $|\overline{P}^0\rangle$. These are eigenstates of the strong force and are useful to talk about as they have definite quark content. However due to the possibility of mixing from electroweak process, these states are not eigenstates of the electroweak Hamiltonian and therefore are not stationary.

A general state $|P(t)\rangle$ can be constructed using the flavor eigenstates $|P^0\rangle$ and $|\overline{P}^0\rangle$, as

$$|P(t)\rangle = P^0(t)|P^0\rangle + \overline{P}^0(t)|\overline{P}^0\rangle. \tag{A.19}$$

The time-dependence of $|P(t)\rangle$ is given by the Schrödinger equation

$$i\hbar\frac{\partial P(t)}{\partial t} = H|P(t)\rangle, \tag{A.20}$$

where H is the Hamiltonian matrix. CPT invariance (which is prerequisite of quantum field theory and assumed to be true) leads to the diagonal elements of the Hamiltonian matrix being equal (ie. $H_{11} = H_{22}$). If we assume CP is an exact symmetry then the off-diagonal elements of H are also equal. So that H can be written as

$$H = \begin{pmatrix} A & B \\ B & A \end{pmatrix}.$$

EquationA.20 represents two couple modes. The modes can be decoupled by deagonalising the matrix H, which leads to two new states

$$|P_+(t)\rangle = \frac{1}{\sqrt{2}}(|P\rangle + |\overline{P}\rangle),\ |P_-(t)\rangle = \frac{1}{\sqrt{2}}(|P\rangle - |\overline{P}\rangle) \tag{A.21}$$

which obey the decoupled equations

$$i\frac{\partial|P_+\rangle}{\partial t} = M_+|P_+\rangle - i\Gamma_+/2|P_+\rangle,\ i\frac{\partial|P_-\rangle}{\partial t} = M_-|P_-\rangle - i\Gamma_-/2|P_-\rangle. \tag{A.22}$$

The masses and widths of the new states are

$$M_\pm = \Re(A \pm B),\ \ -\Gamma_\pm/2 = \Im(A \pm B). \tag{A.23}$$

The decoupled states are eigenstates of mass and CP, such that

$$\widehat{CP}|P_\pm\rangle = \pm|P_\pm\rangle. \tag{A.24}$$

In dealing with mixing it is useful to define the mass and mass difference as

$$m = (M_+ + M_-)/2,\ \Delta m = |M_+ - M_-|, \tag{A.25}$$

and the lifetime and lifetime difference as

$$\Gamma = (\Gamma_+ + \Gamma_-)/2,\ \Delta\Gamma = |\Gamma_+ - \Gamma_-|. \tag{A.26}$$

A.5.2 B^0-$\overline{B}^0$ Mixing with CP violation

As same as K^0 meson system, B^0 and $\overline{B}^0$ can mix through second order weak interactions via box diagrams shown in Figure A.5. Due to mixing, arbitrary neutral B meson state is written as linear combination of B^0 and $\overline{B}^0$

$$|B(t)\ \rangle\ =\ \alpha(t)\ |B^0\ \rangle\ +\ \beta(t)\ |\overline{B}^0\ \rangle \tag{A.27}$$

The time-dependent Schrödinger equation of $|B(t)\ \rangle$ with the Hamiltonian of $\mathcal{H}$ is

$$i\frac{\partial}{\partial t}|B(t)\ \rangle\ \ =\ \ \mathcal{H}\ |B(t)\ \rangle \tag{A.28}$$

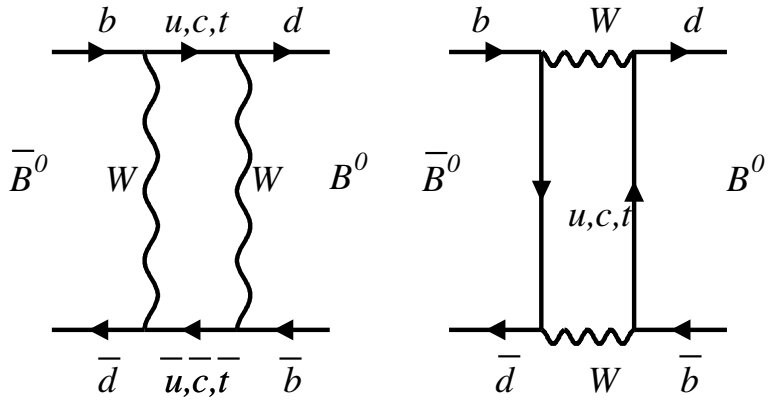

Figure A.5: The box diagrams responsible for $B^0 - \overline{B}^0$ mixing

$\mathcal{H}$ is defined as

$$\mathcal{H} = \mathbf{M} - \frac{i}{2}\mathbf{\Gamma} = \begin{pmatrix} M_{11} - \frac{i}{2}\Gamma_{11} & M_{12} - \frac{i}{2}\Gamma_{12} \\ M_{12} - \frac{i}{2}\Gamma_{12} & M_{22} - \frac{i}{2}\Gamma_{22} \end{pmatrix} \tag{A.29}$$

where, $\mathbf{M}$ and $\mathbf{\Gamma}$ are Hermitian matrices, which are called the mass and decay matrices, respectively. M_{11} and M_{22} are the B^0 and $\overline{B}^0$ mass, and Γ_{11} and Γ_{22} are the decay width of the flavor eigenstates, B^0 and $\overline{B}^0$, respectively. $M_{12}(M_{21})$ and $\Gamma_{12}(\Gamma_{21})$ represent transition amplitude from B^0 to $\overline{B}^0$ (from $\overline{B}^0$ to B^0).

Since CPT invariance requires $M_{11} = M_{22} \equiv M_0$ and $\Gamma_{11} = \Gamma_{22} \equiv \Gamma_0$, eigenvalues $\mu_\pm$ of Schrödinger equation of (A.28) can be written as

$$\begin{aligned} \mu_{H,L} &= m_{H,L} - \frac{i}{2}\Gamma_{H,L} \\ &= \left(M_0 - \frac{i}{2}\Gamma_0\right) \pm \left[\left(M_{12} - \frac{i}{2}\Gamma_{12}\right)\left(M_{12}^* - \frac{i}{2}\Gamma_{12}^*\right)\right]^{\frac{1}{2}} \end{aligned} \tag{A.30}$$

which correspond to eigenvectors $|B_{H,L}\rangle$ that are given as

$$|B_{H,L}\rangle = p|B^0\rangle \pm q|\overline{B}^0\rangle\,, \tag{A.31}$$

$$\frac{q}{p} = \left(\frac{M_{12}^* - \frac{i}{2}\Gamma_{12}^*}{M_{12} - \frac{i}{2}\Gamma_{12}}\right)^{\frac{1}{2}} \tag{A.32}$$

where p and q are normalized as $|p^2| + |q^2| = 1$. H, L represents "light" mass eigenstate of $|B_L\rangle$ and "heavy" mass eigenstate of $|B_H\rangle$, and we defined mass and width of $B_{H,L}$ as $m_{H,L}$ and $\Gamma_{H,L}$, respectively. Using Equation A.30, time evolutions of $|B_H\rangle$ and $|B_L\rangle$ are

given by

$$|B_H(t)\rangle = (p|B^0\rangle + q|\overline{B}^0\rangle)e^{-i\mu_H t} \quad (A.33)$$
$$|B_L(t)\rangle = (p|B^0\rangle - q|\overline{B}^0\rangle)e^{-i\mu_L t} \quad (A.34)$$

From Equation A.31, flavor eigenstates, B^0 and $\overline{B}^0$ are expressed as

$$|B^0\rangle = \frac{1}{2p}(|B_H\rangle + |B_L\rangle)\ ,\ |\overline{B}^0\rangle = \frac{1}{2q}(|B_H\rangle - |B_L\rangle). \quad (A.35)$$

Thus, time evolutions of B^0 and $\overline{B}^0$ are given by

$$|B^0(t)\rangle = g_+(t)|B^0\rangle + \frac{q}{p}g_-(t)|\overline{B}^0\rangle \quad (A.36)$$
$$|\overline{B}^0(t)\rangle = \frac{p}{q}g_-(t)|B^0\rangle + g_+(t)|\overline{B}^0\rangle \quad (A.37)$$

where

$$g_\pm = \frac{1}{2}(e^{-i\mu_H t} \pm e^{-i\mu_L t}), \quad (A.38)$$

and Δm $\Delta\Gamma$ are the difference of mass and width of the two mass eigenstates as

$$\begin{aligned}\Delta m &= m_H - m_L \\ &= 2Re\sqrt{\left(M_{12} - \frac{i}{2}\Gamma_{12}\right)\left(M_{12}^* - \frac{i}{2}\Gamma_{12}^*\right)} \\ \Delta\Gamma &= \Gamma_H - \Gamma_L \\ &= -4Im\sqrt{\left(M_{12} - \frac{i}{2}\Gamma_{12}\right)\left(M_{12}^* - \frac{i}{2}\Gamma_{12}^*\right)}\end{aligned}$$

In the B meson system, the neutral B meson mass is heavy enough to reduce such an effect to a level of $(\Gamma_H - \Gamma_L)/\Gamma \sim \mathcal{O}(10^{-3})$. Therefore, we set $\Gamma_H = \Gamma_L = \Gamma$. Thus, are represented with $\Delta\Gamma = 0$ as

$$g_\pm = \frac{1}{2}\exp\left\{\left(-iM - \frac{\Gamma}{2}\right)t\right\}(1 \pm \exp(-i\Delta m t)) \quad (A.39)$$

A.5.3 B Meson Decays into CP Eigenstates

In this subsection, we consider time evolution of neutral B mesons decays into a CP eigenstate, f_{CP} that is possible for both B^0 and $\overline{B}^0$ decays. we define the amplitudes of these processes as

$$A(f_{CP}) \equiv \langle f_{CP}|\mathcal{H}|B^0\rangle\ \ ,\ \ \overline{A}(f_{CP}) \equiv \langle f_{CP}|\mathcal{H}|\overline{B^0}\rangle$$

Using equations A.36 and A.37, the time-dependent decay rates for initially pure B^0 or $\overline{B}^0$ states decaying into f_{CP} are given by

$$\begin{aligned}\Gamma(B^0(t)\to f_{CP}) = e^{-\Gamma t}|A|^2 &\left[\frac{1+\cos\Delta mt}{2} + \left|\frac{q}{p}\right|^2 |\overline{\rho}(f_{CP})|^2\frac{1-\cos\Delta mt}{2}\right.\\ &\left. -Im\left[\left(\frac{q}{p}\right)\overline{\rho}(f_{CP})\right]\sin\Delta mt\right]\\ \Gamma(\overline{B}^0(t)\to f_{CP}) = e^{-\Gamma t}|\overline{A}|^2 &\left[\frac{1+\cos\Delta mt}{2} + \left|\frac{p}{q}\right|^2 |\rho(f_{CP})|^2\frac{1-\cos\Delta mt}{2}\right.\\ &\left. -Im\left[\left(\frac{p}{q}\right)\rho(f_{CP})\right]\sin\Delta mt\right]\end{aligned} \tag{A.40}$$

where,

$$\begin{aligned}\overline{\rho}(f_{CP}) &\equiv \frac{\overline{A}(f_{CP})}{A(f_{CP})},\\ \rho(f_{CP}) &\equiv \frac{A(f_{CP})}{\overline{A}(f_{CP})}.\end{aligned} \tag{A.41}$$

Let λ_{CP} define as

$$\lambda_{CP} \equiv \frac{q}{p}\overline{\rho}(f_{CP}), \tag{A.42}$$

The decay rates are written as

$$\begin{aligned}\Gamma(B^0(t)\to f_{CP}) &= e^{-\Gamma t}|A|^2\left[1 - \frac{|\lambda_{CP}|^2-1}{|\lambda_{CP}|^2+1}\cos\Delta mt - \frac{2Im\lambda_{CP}}{|\lambda_{CP}|^2+1}\sin\Delta mt\right]\\ \Gamma(\overline{B}^0(t)\to f_{CP}) &= e^{-\Gamma t}|A|^2\left[1 + \frac{|\lambda_{CP}|^2-1}{|\lambda_{CP}|^2+1}\cos\Delta mt + \frac{2Im\lambda_{CP}}{|\lambda_{CP}|^2+1}\sin\Delta mt\right]\end{aligned} \tag{A.43}$$

Thus, the time-dependent CP asymmetry is defined as the normalized decay rate difference:

$$\begin{aligned}a_{f_{CP}} \equiv &\frac{\Gamma(\overline{B}^0(t)\to f_{CP}) - \Gamma(B^0(t)\to f_{CP})}{\Gamma(\overline{B}^0(t)\to f_{CP}) + \Gamma(B^0(t)\to f_{CP})}\\ = &\frac{(|\lambda_{CP}|^2-1)\cos\Delta mt + 2Im\lambda_{CP}\sin\Delta mt}{|\lambda_{CP}|^2+1},\end{aligned} \tag{A.44}$$

A.5.4 CP Violation in $B^0 \to J/\psi K^0_S$ Decays

$B^0 \to J/\psi K^0_S$, which is governed by the $b\to c\overline{c}s$ transition, is promissing decay mode to extract ϕ_1 experimentally. This decay mode is so-called "golden mode", because of relatively large branching fractions with small backgrounds. In addition, the final state has only negligible theoretical uncertainty in ϕ_1 measurement. In the following, we describe time-dependent CP violation in $B^0 \to J/\psi K^0_S$ decays briefly.Therefore, we can neglect

the contribution from the weak phase in the tree diagram for $B^0 \to J/\psi K_S^0$ as shown in Figure A.6,

$$\frac{\overline{A}(\overline{B}^0 \to J/\psi K_S^0)}{A(B^0 \to J/\psi K_S^0)} = \frac{V_{cb}V_{cs}^*}{V_{cb}^*V_{cs}} = 1. \tag{A.45}$$

The dominant penguin contribution has the same weak phase as the tree. Therefore, we can neglect the contribution from the weak phases other than the tree diagram.

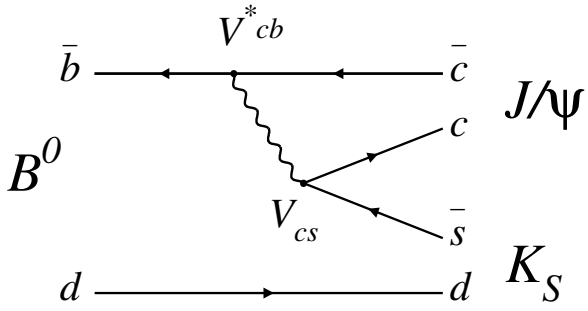

Figure A.6: $J/\psi K_S$ decays

Here, we calculate q/p. The main contribution to the box diagrams of B^0-$\overline{B}^0$ mixing in Figure A.5 is the top quark because of its heavy mass, and the CKM matrix elements contributing to the mixing are $V_{tb}V_{td}^*$ on the vertices of the box diagrams. Theoretical calculations [17] [18] on M_{12}, Γ_{12} and their ratio yield:

$$\begin{aligned} M_{12} &\propto (V_{tb}V_{td}^*)^2 m_t^2, \\ \Gamma_{12} &\propto (V_{tb}V_{td}^*)^2 m_b^2, \\ \left|\frac{\Gamma_{12}}{M_{12}}\right| &\simeq \frac{m_b^2}{m_t^2} \simeq 10^{-3}, \end{aligned} \tag{A.46}$$

where m_b is the bottom quark mass and m_t is the top quark mass. Using Equation A.32 and A.46, the q/p becomes

$$\begin{aligned} \frac{q}{p} &= \sqrt{\frac{M_{12}^*}{M_{12}}} + \mathcal{O}\left(\frac{\Gamma_{12}}{M_{12}}\right) \\ &\simeq \frac{V_{tb}^*V_{td}}{V_{tb}V_{td}^*} = e^{-2i\phi_1} \end{aligned} \tag{A.47}$$

Therefore , $\lambda_{J/\psi K_S^0}$ which corresponds to Equation A.42 by replacing $f_{CP} = J/\psi K_S^0$, becomes

$$\begin{aligned} \lambda_{J/\psi K_S^0} &\propto -\frac{\overline{A}(\overline{B}^0 \to J/\psi K_S^0)}{A(B^0 \to J/\psi K_S^0)} \cdot \left(\frac{q}{p}\right) \\ &\simeq -\frac{V_{cb}V_{cs}^*}{V_{cb}^*V_{cs}} \cdot \frac{V_{tb}^*V_{td}}{V_{tb}V_{td}^*} \\ &= -e^{-2i\phi_1}. \end{aligned}$$

The minus sign in front of Equation A.48 corresponds to the state of $|J/\psi K_S^0\rangle$ being CP odd. Because of $|B^0 \to J/\psi K_S^0| = |\overline{B}^0 \to J/\psi K_S^0|$ and $|q/p| = 1$, $|\lambda_{J/\psi K_S^0}| = 1$ holds, as a result Equation A.43 becomes:

$$\begin{aligned} \Gamma(B^0(t) \to f_{CP}) &= e^{-\Gamma t}|A|^2(1 - \sin 2\phi_1 \cdot \sin \Delta m t), \\ \Gamma(\overline{B}^0(t) \to f_{CP}) &= e^{-\Gamma t}|A|^2(1 + \sin 2\phi_1 \cdot \sin \Delta m t), \end{aligned} \tag{A.48}$$

and time-dependent asymmetry for $B^0 \to J/\psi K_S^0$ decays is given by

$$a_{J/\psi K_S^0} = \sin 2\phi_1 \cdot \sin \Delta m t. \tag{A.49}$$

CP violation in these decays involving the $b \to c\bar{c}s$ transition has been established by the Belle[3] and BaBar[4] collaborations. The measured results are in good agreement with the Standard Model expectation. Therefore, we can regard the CP-violating parameter $\sin 2\phi_1$ measured in $B^0 \to J/\psi K_S^0$ decays as the value for the Standard Model.

A.6 Principle of the Measurement

At the Belle experiment, B mesons are produced through the $e^+e^- \to \Upsilon(4S) \to B\overline{B}$ process. The mass of $\Upsilon(4S)$, which is a bound state of a b quark and a $\overline{b}$ quark, is 10.58 GeV/c^2. The value is just above the B meson pair production threshold 5.28GeV/$c^2 \times 2 =$ 10.56GeV/c^2. Thus the $\Upsilon(4S)$ meson decays nearly 100 % into $B^0\overline{B}^0$ or B^+B^- with almost the same branching fraction. In the Belle experiment, the $B^0\overline{B}^0$ pair is produced with the Lorentz boost of $\beta\gamma = 0.425$ by an asymmetric collision of a positron and an electron with energy of 3.5 GeV and 8 GeV, respectively. Because, to measure time-dependent CP asymmetry parameters, we need to determine the initial flavor of B meson and the decay time. The boosted $B^0\overline{B}^0$ pair has a characteristic feature suitable for these measurement.

A $B^0\overline{B}^0$ pair from $\Upsilon(4S)$ is produced as a C-odd state. Although $B^0 - \overline{B}^0$ oscillation then starts, the state preserves the C-odd configuration and is not allowed to be B^0B^0 or $\overline{B}^0\overline{B}^0$. The time evolution of the pair is given by

$$\begin{aligned} |\Psi(t)\rangle &= e^{-t/\tau_{B^0}}|\Psi(t=0)\rangle, \\ |\Psi(t=0)\rangle &= \frac{1}{\sqrt{2}}[|B^0(\vec{k})\overline{B}^0(-\vec{k})\rangle - |B^0(-\vec{k})\overline{B}^0(\vec{k})\rangle], \end{aligned} \tag{A.50}$$

where τ_{B^0} is the lifetime of the neutral B meson, and $\vec{k}$ and $-\vec{k}$ are the B mesons' momenta in the $\Upsilon(4S)$ center of mass system. This coherence is preserved until one B meson decays. Hence, if we detect a decay of one of the B meson pair, which we call B_{tag}, and tag its flavor from the decay product at the time t_{tag}, we can determine the flavor of the other B meson, which we call B_{CP}, to be the opposite flavor of B_{tag} at t_{tag}. We then detect B_{CP} decay into $J/\psi K_S^0$ at the time t_{CP} by a probability given by

$$\mathcal{P}(q, \Delta t; \mathcal{A}_{J/\psi K_S^0}, \mathcal{S}_{J/\psi K_S^0}) = \frac{e^{-\frac{|\Delta t|}{\tau_{B^0}}}}{4\tau_{B^0}}\Big[1 + q(\mathcal{A}_{J/\psi K_S^0}\cos\Delta m\Delta t + \mathcal{S}_{J/\psi K_S^0}\sin\Delta m\Delta t\Big)], \tag{A.51}$$

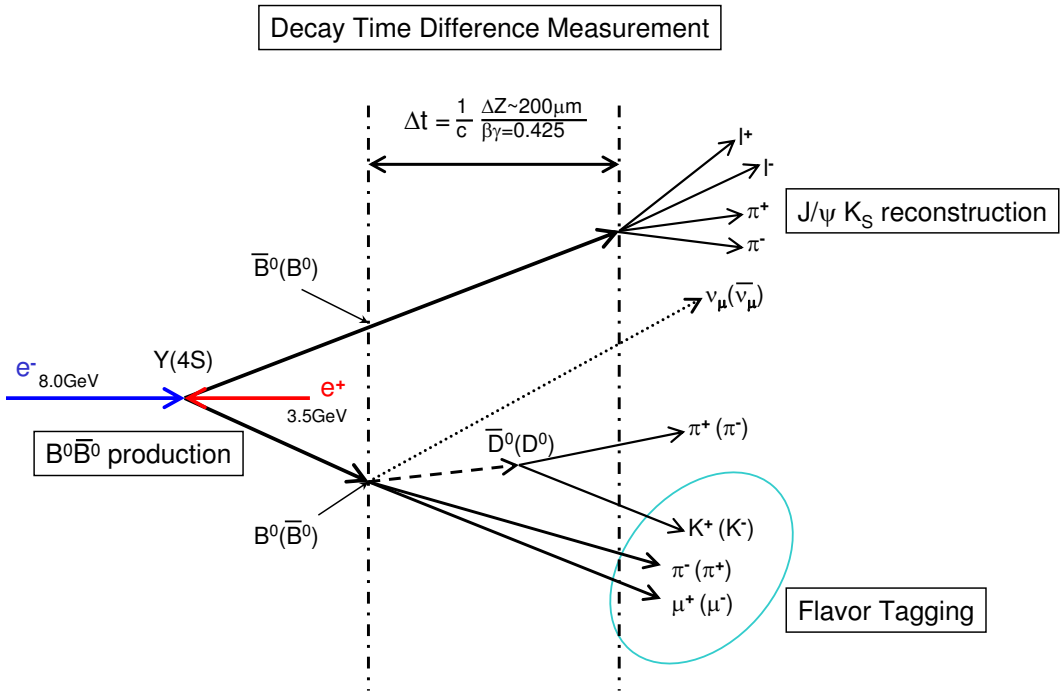

Figure A.7: The schematic picture of the experiment.

where $\Delta t \equiv t_{CP} - t_{tag}$ and q denotes the flavor of B_{tag}: $q = +1$ corresponds to $B_{tag} = B^0$ and $q = -1$ corresponds to $B_{tag} = \overline{B}^0$. The CP asymmetry becomes

$$\begin{aligned} a_{J/\psi K^0_S} &= \frac{\mathcal{P}(q=1,\Delta t;\mathcal{A}_{J/\psi K^0_S},\mathcal{S}_{J/\psi K^0_S}) - \mathcal{P}(q=-1,\Delta t;\mathcal{A}_{J/\psi K^0_S},\mathcal{S}_{J/\psi K^0_S})}{\mathcal{P}(q=1,\Delta t;\mathcal{A}_{J/\psi K^0_S},\mathcal{S}_{J/\psi K^0_S}) + \mathcal{P}(q=-1,\Delta t);\mathcal{A}_{J/\psi K^0_S},\mathcal{S}_{J/\psi K^0_S}} \\ &= \mathcal{A}_{J/\psi K^0_S}\cos\Delta m\Delta t + \mathcal{S}_{J/\psi K^0_S}\sin\Delta m\Delta t. \end{aligned} \tag{A.52}$$

The probability equation A.51 is normalized in $-\infty\langle\Delta t\langle+\infty$.

Considering the discussion above, we have to carry out the following major items:

- Reconstruction of B_{CP} decays into $J/\psi\pi^0$,
- Measurement of decay time difference Δt between B_{CP} and B_{tag},
- Flavor tagging of B_{tag}.

These are shown schematically in Figure A.7. Since B mesons are nearly at rest in the $\Upsilon(4S)$ center of mass system, they fly along the electron beam direction thanks to the boost and make decay vertices with an average distance of $\beta\gamma c\tau_{B^0} \sim 200$ μm. The Δt is determined from the distance to be

$$\Delta t \simeq \frac{z_{CP} - z_{tag}}{\beta\gamma c} \tag{A.53}$$

where the z axis is defined to be anti-parallel to the positron beam direction, z_{CP} is the z position of the B_{CP} decay vertex and z_{tag} is the z position of the B_{tag} decay vertex. We can measure the Δz by using micro-strip silicon detectors with a spatial resolution better than 200 μm.

A.7 Current knowledgement of the CKM parameters

The CKM sector of the SM can be expressed using the four parameters $\lambda_W, A, \overline{\rho}, \overline{\eta}$ from the Wolfenstein paramterisation. These are related to the original ρ and η by

$$\overline{\rho} = \rho(1 - \lambda_W^2/2),\ \overline{\eta}(1 - \lambda_W^2/2). \tag{A.54}$$

The parameter λ_W (which is $|V_{us}|$) is known to be 0.26 from $K \to \pi l \nu$ decays, with an accuracy of $\sim 1\%$ [16]. Here the theoretical and experimental uncertainties are approximately equal.

A (which is V_{cb}) is also fairly well known from exclusive and inclusive B decays to charm states. The weighted mean from both these methods yields [16]

$$|V_{cb}| = (41.6 \pm 0.6) \times 10^{-3} \tag{A.55}$$

where the dominant theoretical error comes from the uncertainty of the validity of the quark-hadron duality approximation.

Current constrains on the unitarity triangle in the $\overline{\rho}, \overline{\eta}$ plane, are summarised in Figure A.8 The main constraints come from measurements of the side lengths and from recent

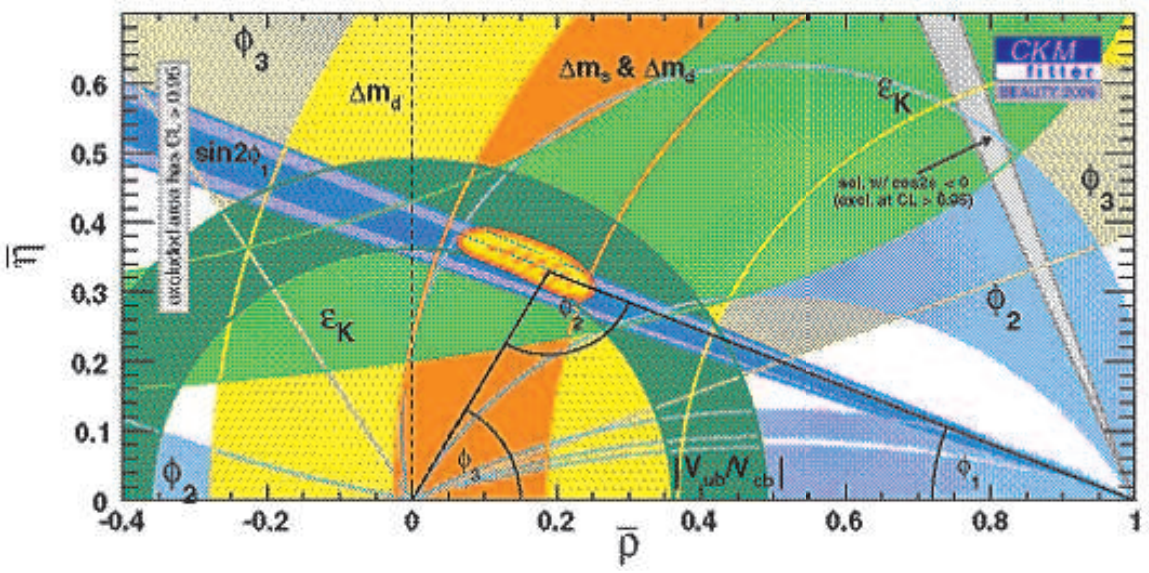

Figure A.8: The constraint on $\overline{\rho} - \overline{\eta}$ plane from neutral B meson mixings ($\Delta m_d and \Delta m_s$), $|V_{ub}/V_{cb}|$ and the CP violation in neutral K meson (ϵ_K) with the $\sin 2\phi_1$ measured by $B^0 \to J/\psi K_S^0$ and others $c\bar{c}K^{(*)0}$ decays overlaid.

measuremsnts of $\sin 2\phi_1$[3] [4]. The two side lengths can be written as

$$R_u = \frac{1-\lambda_W^2/2}{\lambda_W}\left|\frac{V_{ub}}{V_{cb}}\right|,\ R_t = \frac{1}{\lambda_W}\left|\frac{V_{td}}{V_{cb}}\right|, \tag{A.56}$$

$|V_{ub}|$ can be measured using semileptonic B decays to charmless final states. The endpoint of the inclusive semileptonic momentum spectra can be used to determine the ratio $\left|\frac{V_{ub}}{V_{cb}}\right|$. These methodes allow R_u to be known to an accuracy of $\approx 20\%$ with the majority of the error coming from theoretical uncertainties[19].

R_t can be determined by measuring ΔM_{B_d} from mixing analyses ($\Delta m_{B_d} \propto |V_{td}V_{tb}^*|$) where theoretical hadronic uncertainties lead to an uncertainty in the measurement of $|V_{td}|$ of the order of 20 %.

Measurement of ϵ_K also act as a constraint on the possible values of $\overline{\rho}$ and $\overline{\eta}$, this is shown on Figure A.8 as $\Delta m_s/\Delta m_d$.

A.8 Measurement of the angles ϕ_1, ϕ_2 and ϕ_3

The angles of the unitarity triangle (section A.3) can be measured in a model independent way by looking at the decays of B^0 and $\overline{B^0}$s to CP eigenstates. Equation A.18 shows that the imaginary part of λ can be measured using the time dependent asymmetry (given by Equation A.17). The phase of λ depends on the specific decay mode being looked at. Here three modes which lead to possibly the best three measurement of the unitarity angles are discussed.

If F_{CP} is chosen to be the state $J/\psi K_S^0$ the unitarity angle ϕ_1 can be measured. In this case λ is made up of three terms

$$\lambda(B^0 \to J/\psi K_S^0) = \left(\frac{q}{p}\right)_B \left(\frac{\overline{A}}{A}\right) \left(\frac{q}{p}\right)_K \tag{A.57}$$

The first term on the right hand side of this equation comes from $B^0 - \overline{B^0}$ mixing, the next term comes from the actual $B^0 \to J/\psi K_S^0$ decay amplitudes. The final term comes from $K^0 - \overline{K^0}$ mixing in the produced K_S^0. The overall phase of λ can be determined by combining the phases from these three terms. The term which comes from the decay amplitude can be rewritten as

$$\frac{\overline{A}_{f_{CP}}}{A_{f_{CP}}} = \eta_{f_{CP}} \frac{\overline{A_{f_{CP}}}}{A_{f_{CP}}} \tag{A.58}$$

where $\eta_{f_{CP}}$ is the CP eigenvalue of the final state (f_{CP}), which must be ± 1. From looking at the tree Feynman diagram for $B^0 \to J/\psi K_S^0$ (shown on the left of Figure A.9) it can be seen that the amplitude $A \propto V_{cb}V_{cs}^*$. Therefore the amplitude term in Equation A.57 becomes

$$\left(\frac{\overline{A}}{A}\right) = \eta_{J/\psi K_S^0} \frac{V_{cb}^* V_{cs}}{V_{cb}V_{cs}^*} = -\frac{V_{cb}^* V_{cs}}{V_{cb}V_{cs}^*} \tag{A.59}$$

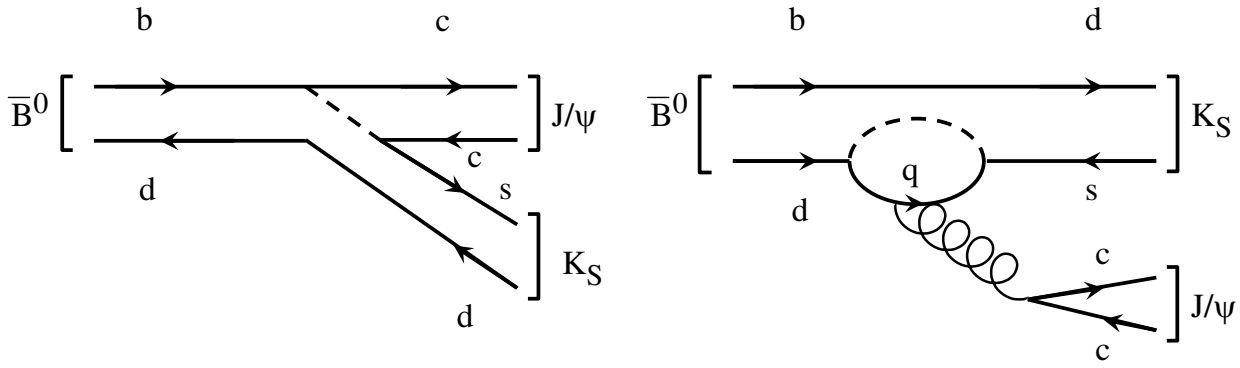

Figure A.9: The tree and penguin Feynman diagrams for the decay $\overline{B}^0 \to J/\psi K^0_S$.

(because the CP eigenvalue of $J/\psi K^0_S$ is -1). The final term from $K^0 - \overline{K}^0$ mixing (which is dominated by the c quark in the box-diagram loop) looks like

$$\left(\frac{q}{p}\right)_K = \frac{V^*_{cs}V_{cd}}{V_{cs}V^*_{cd}} \tag{A.60}$$

This gives

$$\Im(\lambda(B^0 \to J/\psi K^0_S)) = \Im\left(\frac{V^*_{tb}V_{td}}{V_{tb}V^*_{ds}} - \frac{V^*_{cb}V_{cs}}{V_{cb}V^*_{cs}} \cdot \frac{V^*_{cs}V_{cd}}{V_{cs}V^*_{cd}}\right) = \sin 2\phi_1 \tag{A.61}$$

So the time-dependent asymmetry between the rates of $B^0 \to J/\psi K^0_S$ and $\overline{B^0} \to J/\psi K^0_S$ is given by

$$a_{J/\psi K^0_S}(t) = -\sin 2\phi_1 \sin(\Delta m_B t). \tag{A.62}$$

A similar thing can be done to measure ϕ_2, using the decay $B^0 \to \pi^+\pi^-$. The tree

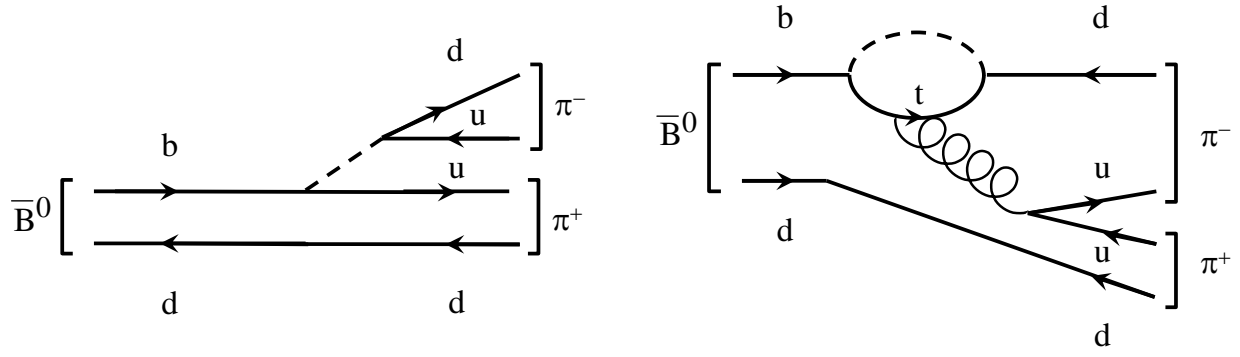

Figure A.10: The tree and penguin Feynman diagrams for the decay $\overline{B}^0 \to \pi^+\pi^-$.

diagram for this mode is shown on the left of Figure A.10. In this case λ is given by

$$\Im(\lambda(B^0 \to \pi^+\pi^-)) = \left(\frac{V^*_{tb}V_{td}}{V_{tb}V^*_{ts}}\right)\left(\eta_{\pi^+\pi^-}\frac{V_{ub}V^*_{ud}}{V^*_{ub}V_{ud}}\right) = \left(\frac{V^*_{tb}V_{td}}{V_{tb}V^*_{td}}\right)\left(\frac{V_{ub}V^*_{ud}}{V^*_{ub}V_{ud}}\right) \tag{A.63}$$

(here there is obviously no contribution from K^0 mixing). The imaginary part of λ is then

$$\Im(\lambda(B^0 \to J/\psi\pi^+\pi^-)) = \sin(2(\pi - \phi_1 - \phi_3)) = \sin 2\phi_2 \tag{A.64}$$

The angle ϕ_3 can be measured using the same technique for the decay $B_s^0 \to \rho K_S^0$. Here we have the K^0 mixing term again, as well as B_s^0 mixing term, so

$$\begin{aligned} \Im(\lambda(B_s^0 \to \rho^0 K_S^0) &= \left(\frac{V_{tb}^* V_{ts}}{V_{tb} V_{ts}^*}\right) \cdot \left(\eta_{\rho^0 K^S} \frac{V_{ub} V_{ud}^*}{V_{ub}^* V_{ud}}\right) \cdot \left(\frac{V_{cs} V_{cd}^*}{V_{cs}^* V_{cd}}\right) \\ &= \left(\frac{V_{tb}^* V_{ts}}{V_{tb} V_{ts}^*}\right) \cdot \left(-\frac{V_{ub} V_{ud}^*}{V_{ub}^* V_{ud}}\right) \cdot \left(\frac{V_{cs} V_{cd}^*}{V_{cs}^* V_{cd}}\right), \end{aligned} \tag{A.65}$$

giving

$$\Im(\lambda(B_s^0 \to \rho K_S^0) = -\sin 2\phi_3. \tag{A.66}$$

Other CP final states can be used to measure ϕ_1 and ϕ_2. Table A.2 shows which angles can be measured from different quark decays, and gives examples of the final states that these could use.

Quark decay	Fianl state	SM prediction for syammetry
$b \to c\bar{c}s$	$J/\psi K_S^0$, $J/\psi K^{*0}(K_S^0\pi^0)$	$-\eta f_{CP} \sin 2\phi_1$
$b \to c\bar{c}d$	D^+D^-, $J/\psi\pi^0$, $J/\psi\rho^0$	$-\eta f_{CP} \sin 2\phi_1$
$b \to u\bar{u}d$	$\pi^+\pi^-$, $\rho^0\pi^0$	$-\eta f_{CP} \sin 2\phi_2$
$b \to s\bar{s}d$	$K_S^0 K_S^0$	0

Table A.2: Examples of CP asymmetry for B decays into CP eigenstates.

A.8.1 Problems from penguins

The above methods have potential uncertainties which come from so called penguin pollution. These arise when a penguin diagram contributes a different phase to the decay amplitude part of $\lambda(\frac{\overline{A}}{A})$. A penguin diagram is one with an internal quark loop which radiates a gluon, photon, or Z^0. The penguins are suppressed by having an additional two vertices (this suppression factor is of order 2 % for gluonic penguins). They can also be suppressed or enhanced with repect to the tree diagram, by the CKM elements at the vertices.

For $B^0 \to J/\psi K_S^0$ the penguin diagram is shown on the right of Figure A.9. The three possible diagrams with $q = u, c, t$ have CKM suppression of order λ_W^4, λ_W^2 & λ_W^2 respectively. It is therefore reasonable to neglect the phase from the diagram involving the u quark as this is much suppressed. The penguin phases for the order two diagrams are $V_{tb}V_{ts}^*$ and $V_{cb}V_{cs}^*$. Using one of the orthogonality relations, which can be re-written

$$V_{tb}V_{ts}^* = -V_{cb}V_{cs}^* + \mathcal{O}(\lambda_W^4), \tag{A.67}$$

we can see that both penguins contribute with the same phase as the tree diagram ($V_{cb}V_{cs}^*$) to $\mathcal{O}(\lambda_W^4)$. This mode is therefore ideal for measuring $\sin 2\phi_1$ to a high degree of accuracy (hadronic uncertainties contribute only at the 10^{-3} level).

When using $B^0 \to \pi^+\pi^-$ to measure ϕ_2 the situation is more complicated. The penguin diagram is shown on the right of Figure A.10. It has the same level of Cabibbo suppression as the tree diagram (both are order λ_W^3). The phase of the penguin diagram is $V_{tb}V_{td}^*$ which is not the same as the tree diagram. This means the measurement of ϕ_2 will suffer from penguin contamination. Using an isospin analysis[20], it is thought the amount of the penguin contribution can be calculated, which will allow a clean measurement of ϕ_2.

A.8.2 $B \to$ vector + vector decays

If the B decay to two vector mesons, the situation becomes slightly more complicated. The spins of the two vector mesons can add up to give a total spin of $0, 1$, or 2. As the B is a scalar particle and the total angular momentum must be conserved, the final state can have an orbital angular momentum of $L = 0, 1$ or 2. Consider a system consisting if two CP eigenstates $|A\rangle$ and $|B\rangle$, with intrinsic CP, η_A and η_B respevtively. The CP of the system is given by

$$\widehat{CP}(|A\rangle|B\rangle) = (-1)^L\widehat{CP}(|A\rangle)\widehat{CP}(|B\rangle) = (-1)^L\eta_A\eta_B|A\rangle|B\rangle. \tag{A.68}$$

Therefore the vector vector final state is not a pure CP eigenstate, but is an admixture of CP odd and CP even, due to the presence of the different angular momentum (L) partial waves. These kind of decays can still be used to measure the unitarity angles, but there is now dilution factor given by the amount of the $L = 0, 2$ and $L = 1$ in the final state. The asymmetry is now given by

$$a_{f_{CP}}^{VV}(t) = D\Im(\lambda)\sin(\Delta m_B t), \tag{A.69}$$

where D is the dilution factor

$$D = \frac{\Gamma_+ - \Gamma_-}{\Gamma_+ + \Gamma_-}. \tag{A.70}$$

Here $\Gamma_\pm$ are the partial widths with CP eigenvalue ± 1.

It has been shown[21] that by studying the angular distributions of the decay products, the values of $\Gamma_\pm$ can be measured. This allows a clean measurement of the unitarity angle.

The most obvious candidate for this kind of analysis is the decay $B^0 \to J/\psi K^{*0}(K_S^0\pi^0)$ to measure $\sin 2\phi_1$. This has been done at Belle. Firstly the different helicity amplitudes (which are directly related to angular momentum states) were measured[22]. This analysis found $D = 0.68 \pm 0.07$.

A.9 The $B^0 \to J/\psi\pi^+\pi^-$ & $B^0 \to J/\psi\rho^0$ decays

A.9.1 Branching fraction estimates

Assuming the modes are dominated by the tree diagram (shown on the left of Figure A.11), the branching fractions can be estimated by simply scaling the measured branching

fractions of the corresponding Cabibbo favored modes. Here the PDG[16] values for the branching fractions are used. The $B^0 \to J/\psi\rho^0$ branching fraction is estimated using

$$Br(B^0 \to J/\psi K^{*0}) \times \left|\frac{V_{cd}}{V_{cs}}^2\right| \times \frac{1}{2} = (3.7 \pm 0.5) \times 10^{-5}, \tag{A.71}$$

where the factor of a half comes from the fact that the ρ^0 and ω partial widths are equal.

The branching fraction for the non-resonant $B^0 \to J/\psi\pi^+\pi^-$ mode can be estimated using

$$\left[Br(B^0 \to J/\psi K^+\pi^-) - \frac{2}{3}Br(B^0 \to J/\psi K^{*0})\right] \times \left|\frac{V_{cd}}{V_{cs}}^2\right| = (1.7 \pm 3.0) \times 10^{-5} \tag{A.72}$$

Here the fraction of K^{*0} events contributing to the $K^-\pi^-$ final state ($\frac{2}{3}$) is subtracted from the total $B^0 \to J/\psi K^+\pi^-$ branching fraction, to leave the non-resonant component. We assume that only the K^* resonance and non-resonant components contribute to the $K^+\pi^-$ final state.

These simple branching fraction estimates are summarised in Table A.3.

Mode	predicted Br. ($\times 10^{-5}$)
$B^0 \to J/\psi\rho^0$	(3.7 ± 0.4)
$B^0 \to J/\psi\pi^+\pi^-$ (non-resonant)	(1.7 ± 3.0)
$B^0 \to J/\psi\pi^+\pi^-$ (combined)	(5.4 ± 3.0)

Table A.3: The simple predictions are obtained by scaling the measured $J/\psi K^*$ and $J/\psi K^+\pi^-$ branching fractions appropriately (assuming tree diagrams dominate).

A.9.2 Measuring $\sin 2\phi_1$ in $B^0 \to J/\psi\rho^0$ decays

As can be seen in tabel A.2 the $J/\psi\rho^0$ mode can be used to measure $\sin 2\phi_1$. The ρ^0 and the J/ψ are both vector particles so an angular analysis (as discussed in section A.8.2) is needed to determine the dilution factor D, before such a measurement can be made.

The estimated branching fraction is an order of λ_W^2 less than the $b \to c\bar{c}s$ modes used to measure $\sin 2\phi_1$, so this mode will not provide a competitive measurement on its own. However it is important to test the SM, and checking that the $b \to c\bar{c}d$ decays give the same value of $\sin 2\phi_1$ is a good test that the CKM picture is correct. The penguin amplitude for this decay (the diagram for which is shown on the right of Figure A.11) could have a magnitude similar to the tree amplitude. This would came the measurement of $\sin 2\phi_1$ more complicated as in this case $|\lambda| \neq 1$. The penguin diagram internal loop can contain any of up type quarks, and all have the same order of Cabibbo suppression (all are of order λ_W^3). The total amplitude can be written as

$$A = T \cdot V_{cd}V_{cb}^* + P_u \cdot V_{ub}V_{ub}^* + P_c \cdot V_{cd}V_{cb}^* + P_t \cdot V_{td}V_{tb}^* \tag{A.73}$$

where T is the magnitude of the tree amplitude, P_q is the magnitude of the penguin amplitude with the quark q in the internal loop. The appropriate CKM phases are shown

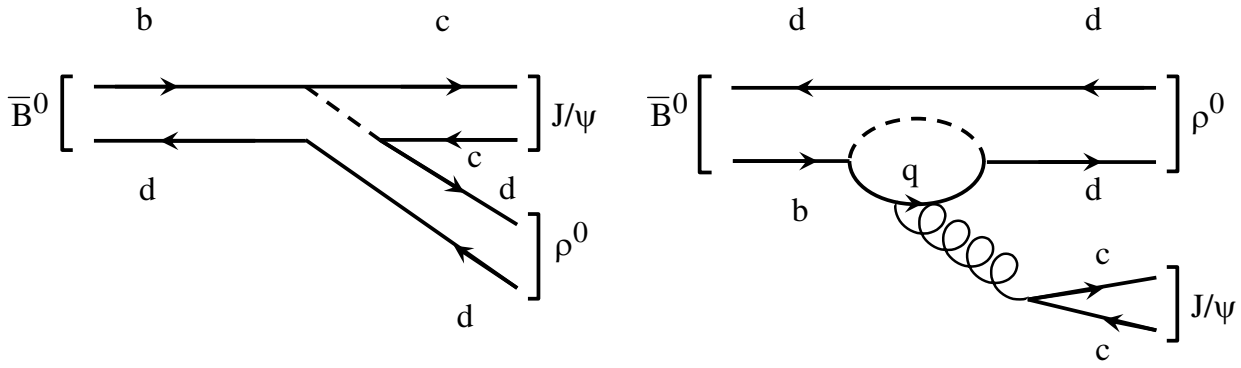

Figure A.11: The tree and penguin Feynman diagrams for the decay $\overline{B}^0 \to J/\psi\rho^0$.

for each term. The penguin diagram proceeding through the c quark has the same CKM phase as the tree diagram and is therefore treated as part of the tree amplitude. The unitarity relation (Equation A.4) can be used to express the $V_{ud}V_{ub}^*$ term in terms of the other two phases. The amplitude then becomes

$$A = (T + P_c - P_u) \cdot V_{cd}V_{cb}^* + (P_t + P_u) \cdot V_{td}V_{tb}^* = \mathcal{T} \cdot V_{cd}V_{cb}^* + \mathcal{P} \cdot V_{td}V_{tb}^*, \tag{A.74}$$

where $\mathcal{T}$ is the tree dominated amplitude and $\mathcal{P}$ is the penguin-only amplitude. When this amplitude is substituted into Equation A.11, we find

$$\lambda(B^0 \to J/\psi\rho^0) = \frac{V_{td}V_{td}^*}{V_{td}V_{tb}}\frac{\overline{A}}{A} = \frac{e^{-i\beta} - |R|e^{i\delta}}{e^{i\beta} - |R|e^{i\delta}} \tag{A.75}$$

where

$$R = \frac{V_{td}^*V_{tb}}{V_{cd}^*V_{cb}}r, \; r = \frac{\mathcal{P}}{\mathcal{T}} = |r|e^{i\delta}, \tag{A.76}$$

r is the ratio of the penguin-only term to the tree dominated term, and δ is the relative strong phase between the two terms.

Using λ given by Equation A.75, the asymmetry (Equation A.17) becomes

$$\begin{aligned} a_{f_{CP}}(t) &= C\cos(\Delta m_B t) + S\sin(\Delta m_B t), \\ C &= \frac{-2|R|\sin\phi_1\sin\delta}{1 + |R|^2 - 2|R|\cos\phi_1\cos\delta}, \\ S &= \frac{\sin 2\phi_1 - 2|R|\sin\phi_1\cos\delta}{1 + |R|^2 - 2|R|\cos\phi_1\cos\delta}. \end{aligned} \tag{A.77}$$

If the tree term dominates the $|R|$ is small and C and S are given by

$$\begin{aligned} C &\approx -2|R|\sin\phi_1\sin\delta, \\ S &\approx \sin 2\phi_1 + 2|R|\sin\phi_1\cos 2\phi_1\cos\delta. \end{aligned} \tag{A.78}$$

Therefore it is impossible to extract $\sin 2\phi_1$ in a model-independent way. C and S can be determined by fitting to the asymmetry, but a theoretical model must be used to give a value of $|R|$, which is needed to get $\sin 2\phi_1$. This is the case for all the $b \to c\overline{c}d$ decay modes, such as $B^0 \to J/\psi\pi^0$ and $B^0 \to D^+D^-$.

Acknowledgment

I wish to first thank my adviser Prof. S. Noguchi for leading me to the field of high energy physics and his gentle support.

I am deeply thankful to my supervisor Prof. K. Miyabayashi and H. Hayashii for their great supports and teaching me the basis of high energy physics.

I wish to express my appreciation to Prof. Y. Sakai, M. Hazumi, K. Trabelsi, H. Ishino and all the members of the Belle ICPV and charmonium groups for their helps and valuable suggestions.

I also would like to thank Prof. T. Tsukamoto, Dr. I. Nakamura, K. Arinstein and I. Bedny for their supports of the work related to ECL.

I would like to express my special thanks to Prof. S.I. Eidelman, A.E. Bonder, G. Phakhalova, J.B. Singh, Y. Yusa and R. Itoh. Without their great helps and precious advises, this thesis work wouldn't have finished.

I also wish to express my thanks to the members in KEK, Ms. M. Watanabe, Y. Uchida, Mr. A. Kusaka and all of my friends for the meaningful discussions and pleasant life with them.

I am most grateful to the members in our group at the Nara Women's University, Dr. S. Kataoka and Ms. M. Fujikawa. They always encourage me whenever needed.

At last, I am especially indebted to all of my family. I appreciate my parent for giving me the opportunity to receive an education. I thank my husband for his great help and support. Without his and his parents' understanding, I could not finish my work.

Bibliography

[1] M. Kobayashi and T. Maskawa, Prog. Theor. Phys. **49**, 652 (1973).

[2] A. B. Carter and A. I. Sanda, Phys. Rev. **D 23**, 1567 (1981); I. I. Bigi and A. I. Sanda, Nucl. Phys. **B 193**, 85 (1981).

[3] K. Abe *et al.* (Belle Collaboration), Phys. Rev. Lett. **87**, 091802 (2001);
K. Abe *et al.* (Belle Collaboration), Phys. Rev. **D66**, 032007 (2002);
K. Abe *et al.* (Belle Collaboration), Phys. Rev. **D66**, 071102(R) (2002).

[4] B. Aubert *et al.* (BaBar Collaboration), Phys. Rev. Lett. **87**, 091801 (2001);
B. Aubert *et al.* (BaBar Collaboration), Phys. Rev. **D66**, 032003 (2002);
B. Aubert *et al.* (BaBar Collaboration), Phys. Rev. Lett. **89**, 201802 (2002).

[5] M. Bishai *et al.* (CLEO collaboration), Phys. Rev. Lett. **B 369**, 186-192 (1996).

[6] B. Aubert *et al.* (BaBar collaboration), Phys. Rev. Lett. **90**, 091801 (2003).

[7] T. D. Lee and C. N. Yang, Phys. Rev. **104**, 254 (1956).

[8] C. S. Wu, E. Amblrt, R. W. Hayward, D. D. Hoppes and R. P. Hudson, Phys. Rev. **105**, 1413 (1957).

[9] R. L. Garwin, L. M. Lederman and M. Weinrich, Phys. Rev. **105**, 1415 (1957).

[10] L. H. Christenson, J. W. Cronin, V. L. Fitch, and R. Turlay, Phys. Rev. Lett. **13**, 138 (1964).

[11] S. Bennett *et al.*, Phys. Rev. Lett. **19**, 993 (1967).

[12] D. Dorfan *et al.*, Phys. Lett. **19**, 983 (1967).

[13] L. Wolfenstein, Phys. Rev. Lett. **51**, 1945 (1983).

[14] C.C. Wang *et al.* (Belle Collaboration), Phys. Rev. Lett. **94**, 121801 (2005).

[15] B. Aubert *et al.*, hep-ex/0408099.

[16] W. M. Yao et al. (Particle Data Group), J. of Phys. **G 33**, 1 (2006)

[17] T. Inami and C.S. Lim, Prog. Theor. Phys., **65**,297(1981).

[18] J. S. Hagelin, Nucl. Phys. **B193**,123 (1981).

[19] A. Hocker *et al.*, hep-ph/010462 (2001).

[20] M. Gronau and D. London, Phys. Lett. **65**, 3381 (1990).

[21] I. Dunietz *et al.*, Phys. Rev. D **43** (1991) 2193.

[22] B. Aubert *et al.*, hep-ex/0107049 (2001).

[23] Belle publications web page, http://belle.kek.jp/belle/publications.html.

[24] S. Kurokawa and E. Kikutani, Nucl. Instr. and. Meth. A **499**, 1 (2003).

[25] A. Abashian *et al.* (Belle Collaboration), Nucl. Instr. and Meth. **A 479** (2002) 117.

[26] V. Chabaud *et al.*, Nucl. Instr. and Meth. **A368**, 314 (1996).

[27] E. Nygård *et al.*, Nucl. Instr. and Meth. **A301**, 506 (1991).

[28] O. Toker *et al.*, Nucl. Instr. and Meth. **A340**, 572 (1994).

[29] G. Alimonti *et al.*, Nucl. Instr. and Meth. **A453**, 71 (2000).

[30] HBOOK, CERN Program Library Long Writeup Y250 (1993).

[31] QQ event generator, `http://www.lns.cornell.edu/public/CLEO/soft/QQ`.

[32] The EvtGen package home page,`http://hep.ucsb.edu/people/lange/EvtGen/`.

[33] D. J. Lange, Nucl. Instr. and Meth. **A462**, 152 (2001).

[34] T. Sjostrand, "High-energy physics event generation with PYTHIA 5.7 and JETSET 7.4" *Comput. Phys. Commun.* **82** (1994) 74-90. 15

[35] T. Sjostrand, "PYTHIA 5.7 and JETSET 7.4: Physics and manual", hep-ph/9508391. 15

[36] B. Andersson, G. Gustafson, G. Ingelman, and T. Sjostrand, "PARTON FRAGMENTATION AND STRING DYNAMICS", *Phys. Rept.* **97** (1983) 31. 15

[37] GEANT detector Description and Simulation Tool, CERN Program Library Long Writeup W5013 (1993).

[38] R. E. Kalman, Trans. ASME, J. Bas. Eng. **82D**, 35 (1960); R. E. Kalman and R. S. Bucy, Trans. ASME, J. Bas. Eng. **83D**, 95 (1961).

[39] K. Hanagaki *et al.*, Nucl. Instr. and Meth. **A485**, 490 (2002).

[40] A. Abashian *et al.*, Nucl. Instr. and Meth. **A491**, 69 (2002).

[41] The dominant contribution comes from two-body B meson decays including a J/ψ meson, with well-measured branching fractions ($B \to J/\psi K^{(*)}$).

[42] See `http://www.slac.stanford.edu/BFROOT/www/Physics/Tools/generators/EvtGen/Evt.ps`

[43] R. Itoh *et al.* (Belle Collaboration), Phys. Rev. Lett. **95**, 091601 (2005).

[44] Belle Collaboration, Technical Report 1, KEK (1995).

[45] B. Casey, Belle note 296 and 390, unpublished.

[46] G. Fox and S. Wolfram, Phys. Rev. Lett. **41**, 1581 (1978).

[47] Private communication with J. Singh and N. Soni. Implementation with the inclusive J/ψ Monte Carlo is based on their preliminary measurements for $B^0 \to J/\psi K_0^*(1430)^0$ and $B^0 \to J/\psi K_2^*(1430)^0$ branching fractions.

[48] J. Pisut and M. Roos, Nucl. Phys. **B 6**, 325 (1968).

[49] J. M. Blatt and V. F. Weisskopf, Theoretical Nuclear Physics (Wiley, New York, 1952), p. 361.

[50] S. Godfrey and N. Isgur, Phys. Rev. **D 32**, 189 (1985)